MIT OpenCourseWare
http://ocw.mit.edu

Continuum Electromechanics

For any use or distribution of this textbook, please cite as follows:

Melcher, James R. *Continuum Electromechanics*. Cambridge, MA: MIT Press, 1981. Copyright Massachusetts Institute of Technology. ISBN: 9780262131650. Also available online from MIT OpenCourseWare at http://ocw.mit.edu (accessed MM DD, YYYY) under Creative Commons license Attribution-NonCommercial-Share Alike.

For more information about citing these materials or our Terms of Use, visit: http://ocw.mit.edu/terms.

4

Electromechanical Kinematics: Energy-Conversion Models and Processes

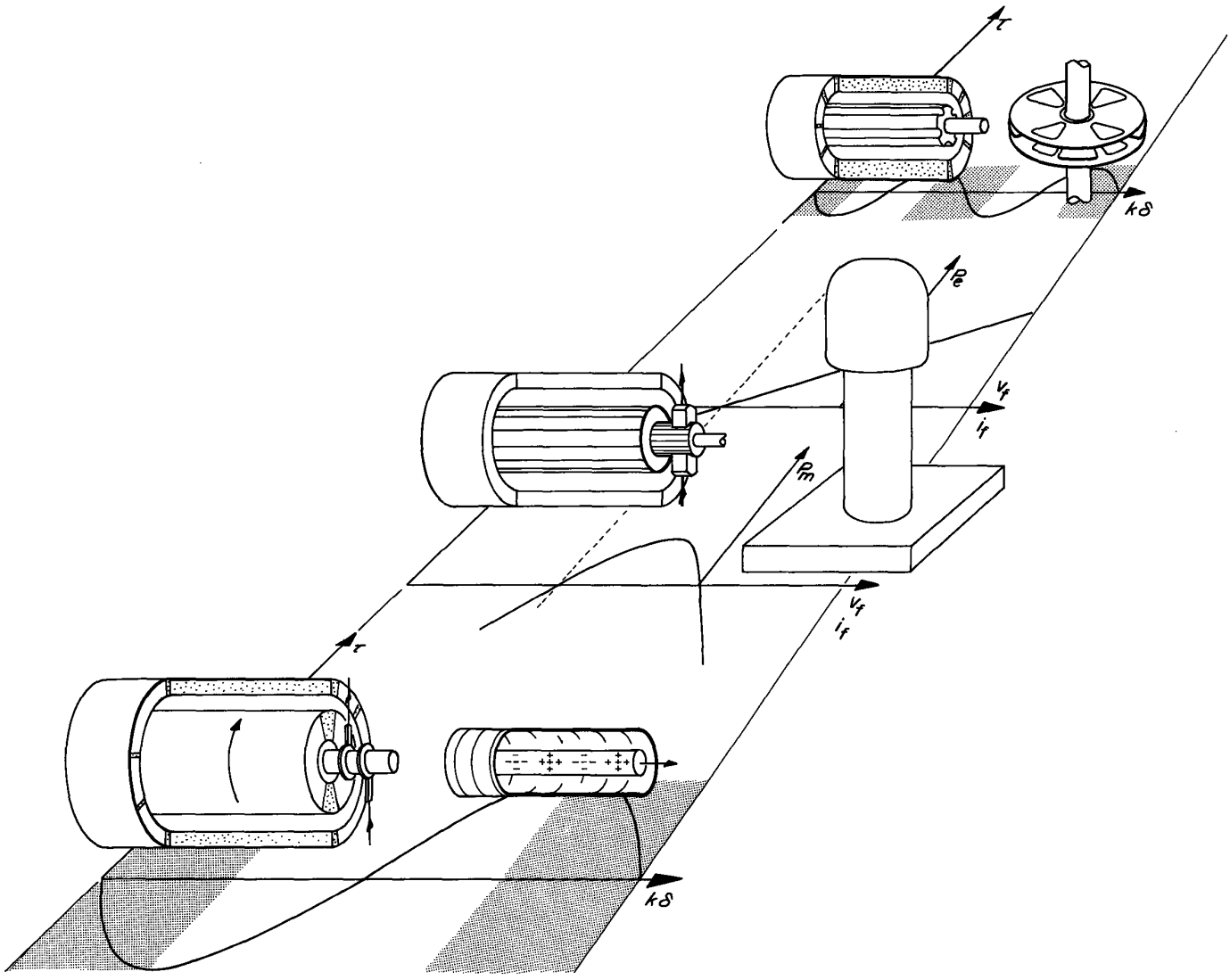

4.1 Objectives

Beginning with this chapter, progressively more electromechanical "degrees of freedom" are considered. The subject of electromechanical kinematics is first because then the relative mechanical motions as well as the paths and trajectories of charges and currents are known from the outset. The mechanics involves rigid-body translations or rotations, while charges and currents might be constrained by electrodes and wires. Processes in this category can be represented by lumped-parameter models. The field approach of this chapter provides the basis for conceptualizing and interrelating such interactions, for appreciating energy conversion limitations, and for deriving the parameters used in lumped-parameter models.

The representation of total forces and torques in terms of Maxwell stresses is developed in Sec. 4.2, followed in Sec. 4.3 by a classification of common types of energy converters, based on the fundamental field interactions. An extension of the transfer relations found in Secs. 2.16 and 2.19 to describe regions occupied by specified distributions of charge and current is made in Secs. 4.5 and 4.8. Although this chapter is concerned with modeling specific interactions, it is the technique for representing these systems that is the message. Section 4.4 exemplifies the notation and strategy underlying the methodical formulation of complex systems in not only this chapter, but those to follow. Of the remaining sections, only one does not pertain to a specific class of devices. Section 4.12 lends some formality to the philosophy underlying quasi-one-dimensional models. Such approximations retain nonlinear interactions and are illustrated in Secs. 4.13 and 4.14. By contrast, Secs. 4.4, 4.6 - 4.9 and 4.11 are concerned with field models that are naturally linear, or are linearized. Formally, the linearized model, in which products of amplitudes are ignored compared to terms that are linear in the amplitudes, is the zero-order approximation in an amplitude-parameter expansion for the exact solution. Similarly, the quasi-one-dimensional model is a zero-order approximation to an expansion in a space-rate parameter.

The analogies that exist between electric and magnetic field interactions is a theme throughout the chapter. This is clear in Sec. 4.3. But a thoughtful comparison of the characteristics of the d-c magnetic machine, considered in more detail in Sec. 4.10, with those of the Van de Graaff machine in Sec. 4.14 is worth while.

An overview of the chapter is given in Sec. 4.15.

4.2 Stress, Force and Torque in Periodic Systems

The configurations shown in Fig. 4.2.1 typify devices exploiting force or torque producing interactions between spatially periodic excitations on a "stator" structure and spatially periodic constrained or induced sources on a "rotor." In each of these, the interaction is across an air gap, a region having the electromagnetic characteristics of free space. The planar configuration of Fig. 4.2.1a might represent a linear motor or generator with the relevant force between "stator" (above) and "rotor" (below) z-directed, or it might be a developed model for the cylindrical geometry of Fig. 4.2.1c (appropriate in the limit where the air-gap spacing is small compared to the radius of the rotor). Figure 4.2.1b shows the cross section of either a planar "slab" with the interaction across two air gaps, or a cylindrical structure having an annular air gap. In either case the relevant net force is z-directed.

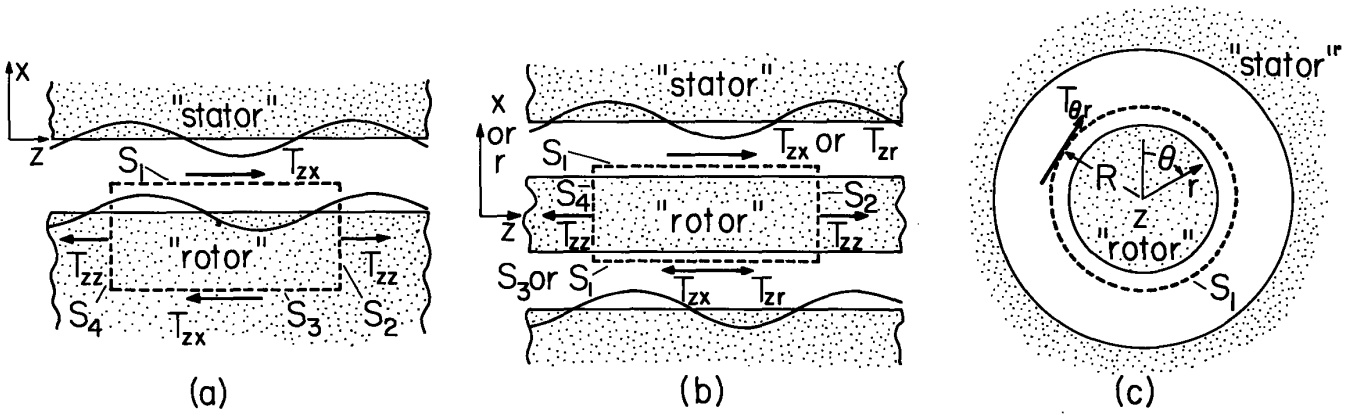

Fig. 4.2.1. Typical "air-gap" configurations in which a force or torque on a rigid "rotor" results from spatially periodic sources interacting with spatially periodic excitations on a rigid "stator." Because of the periodicity, the force or torque can be represented in terms of the electric or magnetic stress acting at the air-gap surfaces S_1: (a) planar geometry or developed model; (b) planar or cylindrical beam; (c) cylindrical rotor.

The total force acting in the z-direction on the "rotor" of Fig. 4.2.1a is conveniently determined by integrating the Maxwell stress, in accordance with Eq. 3.9.4, over the surface S enclosing a portion of the rotor having one fundamental length of periodicity. The portion S_1 of this surface is at an arbitrary plane x = constant in the air gap. Because the fields and hence the stress components T_{zz} are periodic in z, the contributions to the integration of the stress over surfaces S_2 and S_4 cancel regardless of where S_1 is located in the air gap. The contribution to the integration over S_3 can vanish for several reasons. The rotor may be perfectly permeable, of infinite permittivity or infinitely conducting, in which case $\vec{H}$ or $\vec{E}$ is zero on S_3. In Cartesian coordinates, the fields associated with excitations that are periodic in the z-direction decay in the x direction and if S_3 is well removed from the air gap, the contribution on S_3 asymptotically vanishes. Yet another possibility is that the planar model really is a developed model for the cylindrical configuration of Fig. 4.2.1c, in which case the surface S is "pie" shaped and the section S_3 does not exist. In any of these cases, the z-directed force acting on the rotor of Fig. 4.2.1a is simply

$$f_z = A \left\langle T_{zx} \right\rangle_z \Big|_{S_1} \tag{1}$$

where A is the y-z area of the air gap and T_{zx} is the magnetic or electric stress tensor, as the case may be. The brackets indicate a spatial average is taken, as discussed in Sec. 2.15.

There is no question as to which of the stress tensors in Table 3.10.1 should be used. As discussed in Sec. 3.10, in the free-space region of the air gap, all of the magnetic and all of the electric stress tensors agree.

If Fig. 4.2.1b represents a planar layer, then there are stress contributions from surfaces S_1 and S_3, and the net force acting on a section of the layer having area A in the y-z plane is

$$f_z = A[\left\langle T_{zx} \right\rangle_z \Big|_{S_1} - \left\langle T_{zx} \right\rangle_z \Big|_{S_3}] \tag{2}$$

On the other hand, if the "rotor" in that figure is a cylinder, then the net force takes the form of Eq. 1, with A the area of an enclosing cylindrical surface and appropriate shear stress $T_{zx} \rightarrow T_{zr}$ evaluated on that surface.

In computing the net torque on the rotor of Fig. 4.2.1c, it is tempting to multiply the space-average shear stress $\left\langle T_{\theta r} \right\rangle_\theta$ by the lever arm R and the area A of a cylindrical enclosing surface having radius R:

$$\tau_z = RA \left\langle T_{\theta r} \right\rangle_\theta \Big|_{S_1} \tag{3}$$

Because the stress is symmetric, this notion is rigorous, as can be seen by applying Eq. 3.9.16 to the surface S_1 of Fig. 4.2.1c.

4.3 Classification of Devices and Interactions

Based on the developed or linear air-gap configuration of Fig. 4.2.1a, this section begins with illustrative simplified examples of "synchronous" and "d-c" magnetic and electric interactions. Then, a general discussion is given of the various classes of machines, some having lumped-parameter models developed in later sections of this chapter and in the problems.

In parallel, consider first the electric and magnetic configurations of Part 1 of Table 4.3.1. Even though the devices might in fact be developed or "linear," the terms stator and rotor will be used to refer to the elements on respective sides of the air gap. The magnetic field is produced by spatially sinusoidal distributions of current modeled as current sheets on the surfaces of the stator and rotor. Because the stator and rotor are modeled as infinitely permeable, $\vec{H} = 0$ outside the air gap and the surface currents "terminate" the tangential fields (Eq. 2.10.21). The electric field is produced by electrodes constrained to have spatially periodic potentials. Thus, boundary conditions at the air-gap boundaries (s) and (r) are

$$\begin{aligned} H_z^s &= \mathrm{Re}[\tilde{K}^s \exp(-jkz)] \quad \Big| \quad \Phi^s = \mathrm{Re}[\tilde{V}^s \exp(-jkz)] \\ H_z^r &= \mathrm{Re}[-\tilde{K}^r \exp(-jkz)] \quad \Big| \quad \Phi^r = \mathrm{Re}[\tilde{V}^r \exp(-jkz)] \end{aligned} \tag{1}$$

where $(\tilde{K}^s, \tilde{K}^r)$ and $(\tilde{V}^s, \tilde{V}^r)$ are given complex functions of time. (Complex notation is introduced in Sec. 2.15.)

With the surface S_1 taken as the rotor surface, (r), it follows from Eq. 4.2.1 and the average theorem, Eq. 2.15.14, that the force on a section of the rotor having area A is

Table 4.3.1. **Basic configurations illustrating classes of electromechanical interactions and devices. MQS and EQS systems respectively in left and right columns.**

sources imposed on moving member

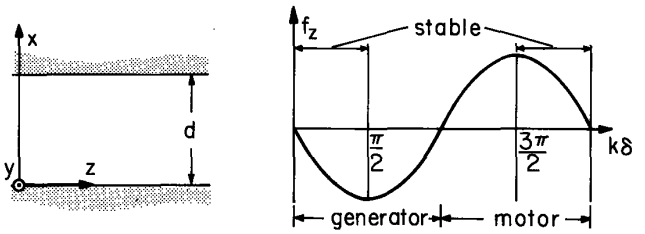

1. currents (potentials) constrained on both windings (electrodes)

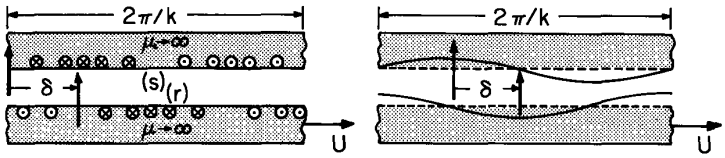

2. current (potential) constrained on "stator" and permanent magnetization (polarization) on "rotor"

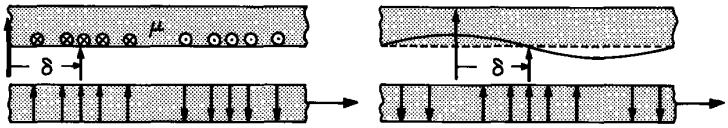

3. current (potential) constrained on "stator" and flux (charge) constrained on "rotor"

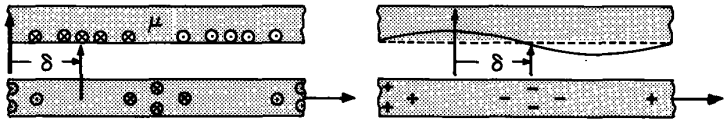

sources instantaneously induced on nonuniform moving member

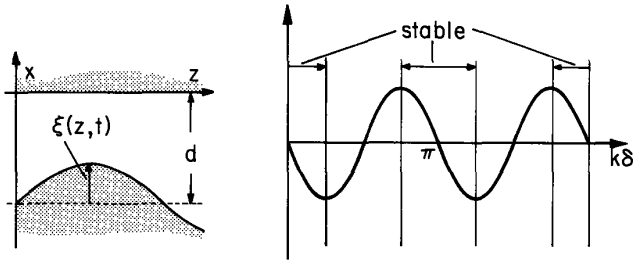

4. current (potential) constrained on "stator" and magnetization (polarization) induced on "rotor" having saliency

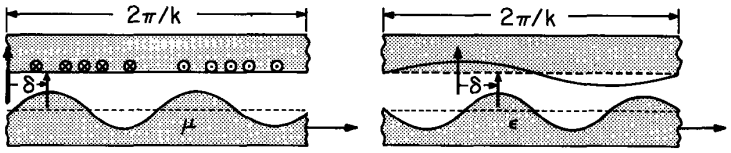

5. current (potential) constrained on "stator" and currents (charges) induced on "rotor" having saliency

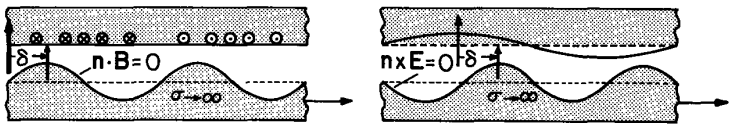

$$f_z = \frac{A}{2}\,\mathrm{Re}\mu_o \tilde{H}_x^r (\tilde{H}_z^r)^* = \frac{A}{2}\,\mathrm{Re}\mu_o \tilde{H}_x^r (-\tilde{K}^r)^* \quad \Big| \quad f_z = \frac{A}{2}\,\mathrm{Re}\epsilon_o \tilde{E}_x^r (\tilde{E}_z^r)^* = \frac{A}{2}\,\mathrm{Re}\epsilon_o \tilde{E}_x^r (jk\tilde{V}^r)^* \tag{2}$$

The gap transfer relations, Eq. (a) of Table 2.16.1, give the normal fluxes at (s) and (r) in terms of the potentials there. In the magnetic case, $H_z = jk\tilde{\Psi}$ and because of the boundary conditions, Eq. 1, these relations become

$$\begin{bmatrix} \mu_o \tilde{H}_x^s \\ \mu_o \tilde{H}_x^r \end{bmatrix} = \mu_o k \begin{bmatrix} -\coth(kd) & \frac{1}{\sinh(kd)} \\ \frac{-1}{\sinh(kd)} & \coth(kd) \end{bmatrix} \begin{bmatrix} \frac{\tilde{K}^s}{jk} \\ \frac{-\tilde{K}^r}{jk} \end{bmatrix} \quad \Big| \quad \begin{bmatrix} \epsilon_o \tilde{E}_x^s \\ \epsilon_o \tilde{E}_x^r \end{bmatrix} = \epsilon_o k \begin{bmatrix} -\coth(kd) & \frac{1}{\sinh(kd)} \\ \frac{-1}{\sinh(kd)} & \coth(kd) \end{bmatrix} \begin{bmatrix} \tilde{V}^s \\ \tilde{V}^r \end{bmatrix} \tag{3}$$

Substitution of the normal flux densities at (r) expressed by Eqs. 3 into Eqs. 2 gives the desired forces

$$f_z = -\frac{A\mu_o}{2\sinh(kd)}\,\mathrm{Re}[j\tilde{K}^s(\tilde{K}^r)^*] \quad \Big| \quad f_z = \frac{A\epsilon_o}{2\sinh(kd)}\,\mathrm{Re}[j(k\tilde{V}^s)(k\tilde{V}^r)^*] \tag{4}$$

Note that the terms involving products of the individual rotor excitations do not contribute. (They are imaginary and hence dropped in taking the real part.) Physically, this is expected because such terms represent the rotor self-field interactions.

Synchronous Interactions: Consider now systems with the rotor excitations produced by windings or electrodes that are fixed to the rotor. The coordinate z' measures distance from a frame of reference moving with the velocity U of the rotor, as sketched in Fig. 4.3.1. Fixed and moving frame coordinates are related in the figure. Perhaps through slip rings, the rotor is excited by a current of angular frequency ω_r, in such a way that as viewed from the rotor there is a current or potential distribution taking the form of a traveling wave:

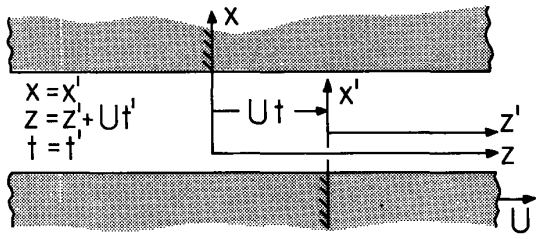

Fig. 4.3.1. Rotor and stator reference frames z' and z.

$$K^r = K_o^r \sin[\omega_r t - k(z' - \delta)] \quad \Big| \quad V^r = -V_o^r \cos[\omega_r t - k(z' - \delta)] \tag{5}$$

On the stator, a similar arrangement of windings or electrodes, with excitations at the angular frequency ω_s, give the traveling waves:

$$K^s = K_o^s \sin[\omega_s t - kz] \quad \Big| \quad V^s = V_o^s \cos[\omega_s t - kz] \tag{6}$$

Because $z' = z - Ut$, Eqs. 5 and 6 can be written in terms of complex amplitudes:

$$\begin{aligned} \tilde{K}^r &= -jK_o^r e^{j(\omega_r + kU)t} e^{jk\delta} \quad \Big| \quad \tilde{V}^r = -V_o^r e^{j(\omega_r + kU)t} e^{jk\delta} \\ \tilde{K}^s &= -jK_o^s e^{j\omega_s t} \quad \Big| \quad \tilde{V}^s = V_o^s e^{j\omega_s t} \end{aligned} \tag{7}$$

Substitution of these amplitudes into the respective force relations of Eq. 4 gives forces with sinusoidal time dependences. The frequencies are in each case $\omega_s - \omega_r - kU$. Only if this frequency is zero will these forces have time-average values. Division of the resulting frequency condition by k shows that these time-average forces exist because, as viewed from the stator frame of reference, the velocities of the traveling waves of field induced by stator and rotor sources are equal:

$$\frac{\omega_s}{k} = \frac{\omega_r}{k} + U \tag{8}$$

Usually, the rotor is d-c excited so that $\omega_r = 0$ and the phase velocity of the stator traveling wave, ω_s/k, is equal to the rotor velocity U. Under the synchronous condition, the substitution of Eqs. 7 into Eqs. 4 gives the forces as functions of the relative spatial phase $k\delta$ between traveling waves:

$$f_z = -\frac{A\mu_o K_o^s K_o^r}{2\sinh kd}\sin k\delta \quad \Big| \quad f_z = -\frac{A\varepsilon_o (kV_o^s)(kV_o^r)}{2\sinh kd}\sin k\delta \tag{9}$$

The sketches of the stator and rotor excitations in Part 1 of Table 4.3.1 (at the instant t = 0) show the relative distributions with $\delta = \lambda/4$, and hence $k\delta \equiv 2\pi(\delta/\lambda) = \pi/2$. According to Eqs. 9, it is at this spatial phase that the greatest retarding force acts on the rotor. The observation is consistent with what would be expected intuitively for the sketched distributions. Under the synchronous conditions the relative distribution of stator and rotor field sources is invariant. The stator current distribution gives rise to a normal flux density that peaks at the current null. This is the stator magnetic axis, indicated by the vertical arrow on the stator. This field interacts with the rotor current to produce the time-average force in the -z direction. Stator and rotor magnetic axes tend to line up. Similarly, in regions of positive and negative electrode potential there are positive and negative surface charges (although not exactly in phase with the potential). Thus, the retarding electric force results from the attraction of neighboring opposite charges. The rotor and stator axes, denoted by the vertical arrows, also tend to line up.

The classic force (or torque) phase-angle diagram, the graphical representation of Eqs. 9, is shown at the top of Table 4.3.1. Angles of positive and negative force can respectively give motor and generator operation. But, operation is generally restricted to the shaded regions because then a change in relative phase, $k\delta$, results in a force that tends to return the rotor to its original angle.

Parts 2 and 3 of Table 4.3.1 illustrate other types of excitations that result in synchronous interactions. In each of these, the rotor sources are "attached" to the rotor and hence the synchronous condition of Eq. 8 reduces to $\omega_s/k = U$. Each has a force with the same dependence on relative phase $k\delta$ illustrated by Eqs. 9.

Small machines having permanent magnet rotors are common, but electric analogues having permanent polarization (Sec. 4.4) are not. By contrast, electric synchronous interactions between traveling waves of charge and potential are common, whereas, devices making use of a trapped rotor flux are not. The former, a kinematic model for electron beam devices, will be considered further in Sec. 4.6.

D-C Interactions: The family of magnetic devices called d-c machines has as an electric field analogue devices of the Van de Graaff type. The configurations shown in Table 4.3.1, Part 1, can also be used to illustrate this class of devices, provided the sketched current and potential distributions are understood to be time-varying in amplitude but stationary in space. Currents are supplied to the rotor windings through brushes and commutator segments in such a way that even though the rotor moves, the rotor's relative current distribution is stationary. The stator current distribution is similarly stationary in space and shifted by the distance δ. The stationary distribution of rotor potential in the electric analogue is an approximation to the potential associated with charge placed on a moving belt at one fixed location and removed at another. Excitations therefore take the form

$$K^r = \mathrm{Re}[-jK_o^r(t)e^{jk\delta}]e^{-jkz} = -K_o^r(t)\sin k(z-\delta) \quad \Big| \quad V^r = \mathrm{Re}[-V_o^r(t)e^{jk\delta}]e^{-jkz} = -V_o^r(t)\cos k(z-\delta)$$

$$K^s = \mathrm{Re}[-jK_o^s(t)]e^{-jkz} = -K_o^s(t)\sin kz \quad \Big| \quad V^s = \mathrm{Re}\,V_o^s(t)e^{-jkz} = V_o^s(t)\cos kz \tag{10}$$

Note that the complex amplitudes multiplying exp(-jkz), now arbitrary functions of time, are as required to evaluate Eqs. 4. The resulting forces are in fact the same as given by Eqs. 9, provided it is understood that (K_o^s, K_o^r) and (V_o^s, V_o^r) are now arbitrary real functions of time.

The magnetic version of the d-c machine is modeled in Sec. 4.10, while the Van de Graaff machine is taken up in Sec. 4.14.

Synchronous Interactions with Instantaneously Induced Sources: Common examples of devices that exploit instantaneously induced magnetization forces on a moving member are variable-reluctance or salient-pole machines. Electric field members of this family of devices include variable-capacitance machines. (By contrast with magnetic and electric "induction" interactions, naturally taken up in the next two chapters, the rotor sources induced by the stator excitations move synchronously with the material. Geometry rather than a rate process, such as magnetic diffusion or charge relaxation, is involved.)

Linear or developed salient-pole models are shown in Part 4 of Table 4.3.1. The rotor, which in the magnetic case is perhaps highly magnetizable magnetically soft iron, has surface saliencies. In a two-pole rotating machine, the rotor represented by this model (with $2\pi/k$ the circumference of the stator) could be a squashed cylinder protruding toward the stator at two positions and away from it at two others. The conventional method for finding the magnetic force on the moving member is to use the energy method of Sec. 3.5 and knowledge of the inductance or capacitance of the stator windings or

electrodes. Because of the rotor saliency, the stator terminal relations clearly depend on the rotor position, and hence so also does the magnetic or electric energy storage.

With the objective of fitting this type of interaction into the field point of view, the development is in terms of the magnetic interaction. Similitude then makes it possible to apply the results to the polarization case. In the limit where the material is highly magnetizable, $\vec{H}$ is excluded from the rotor so that on the rotor surface the tangential field vanishes. As a result, the magnetic traction acts normal to the surface of the rotor. That is, in a local Cartesian coordinate system on the rotor surface, having the axis n in the normal direction, any of the stress tensors (Table 3.10.1) evaluated in free space next to the rotor surface give a traction

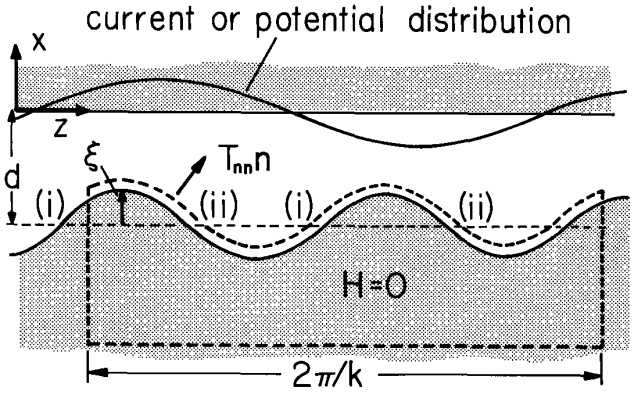

Fig. 4.3.2. Traction $\vec{\vec{T}}\cdot\vec{n} = T_{nn}\vec{n}$ acts normal to rotor surface.

$$\vec{\vec{T}} = \vec{\vec{T}}\cdot\vec{n} = T_{nn}\vec{n} \tag{11}$$

Although not convenient for mathematical derivations, the surface enclosing one periodicity length $2\pi/k$ of the rotor, shown in Fig. 4.3.2, helps in understanding how the magnetic traction gives rise to a net force on the rotor. The traction acting normal to the surface has a value $T_{nn} = \mu_o H_n^2/2$ and hence is positive. No matter what the excitation from the stator winding, it is clear that at positions (i), where the slope of the stator surface is positive, the magnetic field tends to pull the rotor to the left while at point (ii) the pull is to the right. It is the spatial phase relationship between the stator current distribution and the rotor saliencies that makes one or the other of these forces dominant. It is clear, for example, that if the rotor surface wavelength matched that of the stator current there could be no net force. The z-directed traction acting at any given point would then be cancelled by that acting at a point on the rotor surface a half-wavelength away.

In deriving the relation of the excitation and rotor geometry to the net force, the rotor surface is taken as being at

$$x = -d + \xi(z,t) = -d + \mathrm{Re}\,\hat{\xi}\, e^{-j(2k)(z-Ut)} \tag{12}$$

The rotor travels with the linear velocity $U = \omega/k$ and hence its surface, with wavelength π/k half that of the stator excitation, moves in synchronism with the traveling wave of stator surface current:

$$\vec{K} = \mathrm{Re}\hat{K}^s e^{j(\omega t - kz)}\vec{i}_y \tag{13}$$

A surface, represented by $F(x,y,z,t) = x + d - \xi = 0$, has a normal vector

$$\vec{n} = \frac{\nabla F}{|\nabla F|} = \frac{\vec{i}_x - \frac{\partial \xi}{\partial z}\vec{i}_z}{|\nabla F|} \tag{14}$$

As a reminder that this is a familiar relation, the surface might be one of zero potential ($F \to \Phi$), with $\vec{n}$ the negative of the electric field intensity normalized so that it has unit magnitude. The condition that there be no tangential field on the rotor surface is then

$$[\vec{n} \times \vec{H}]_y = 0 \Rightarrow H_z = -H_x \frac{\partial \xi}{\partial z} \text{ at } x = -d + \xi \tag{15}$$

To match this boundary condition is in general difficult. In this section, it is assumed that ξ is small, so that Eq. 15 is evaluated approximately (to first order in ξ) at the "equilibrium" position of the rotor surface, $x = -d$. With H_x evaluated at $x = -d$ rather than at $x = -d + \xi$, the right-hand side of Eq. 15 is already written to first order in ξ:

$$H_z(x = -d + \xi) = H_z(x = -d) + \frac{\partial H_z}{\partial x}(x = -d)\xi \tag{16}$$

If it is further recognized that because $\vec{H}$ is irrotational, $\partial H_z/\partial x = \partial H_x/\partial z$, then to first order in ξ, Eq. 15 becomes a boundary condition to be evaluated at $x = -d$, defined as the position (r):

$$H_z^r = -\frac{\partial}{\partial z}(H_x^r \xi) \tag{17}$$

What must be used in evaluating H_x^r is the zero-order field. This is the field that would be found with $\xi = 0$, with the rotor presenting a planar surface to a gap excited on the stator side by the current sheet given by Eq. 13. Thus, Eq. 17 takes the form

$$H_z^r = -\frac{\partial}{\partial z}\left[\mathrm{Re}\hat{H}_x^r e^{j(\omega t-kz)}\,\mathrm{Re}\hat{\xi}e^{-2jk(z-Ut)}\right]$$
$$= -\frac{\partial}{\partial z}\left\{\frac{1}{2}\left[\hat{H}_x^r e^{j(\omega t-kz)} + (\hat{H}_x^r)^* e^{-j(\omega t-kz)}\right]\frac{1}{2}\left[\hat{\xi}\, e^{-2jk(z-Ut)} + \hat{\xi}^* e^{2jk(z-Ut)}\right]\right\} \tag{18}$$

Because of the synchronism condition, $\omega = kU$, multiplying out this expression gives a term having the same spatial frequency as the stator current and a term at three times that frequency:

$$H_z^r = -\frac{\partial}{\partial z}\left[\mathrm{Re}\hat{\psi}_k e^{j(\omega t-kz)} + \mathrm{Re}\hat{\psi}_{3k} e^{3j(\omega t-kz)}\right];\ \hat{\psi}_k \equiv \frac{1}{2}(\hat{H}_x^r)^*\hat{\xi},\ \hat{\psi}_{3k} \equiv \frac{1}{2}(\hat{H}_x^r)\hat{\xi} \tag{19}$$

Note that this expression takes the form $\vec{H} = -\nabla\Psi$. With the surface S_1 of Fig. 4.2.1a taken as contiguous with the stator, the desired space-average rotor force is

$$f_z = A\langle T_z\rangle_z = A\left\langle \mu_o H_x^s \mathrm{Re}\hat{K}^s e^{j(\omega t-kz)}\right\rangle_z \tag{20}$$

Note that the terms in Eq. 19 are written in the standard complex form, with the quantity in brackets the magnetic potential Ψ. The amplitudes at the stator and rotor surfaces (at s and r) are therefore related by the transfer relation (Eqs. (a) of Table 2.16.1):

$$\begin{bmatrix}\mu_o\hat{H}_x^s\\ \mu_o\hat{H}_x^r\end{bmatrix} = \mu_o k\begin{bmatrix}-\coth(kd) & \dfrac{1}{\sinh(kd)}\\ \dfrac{-1}{\sinh(kd)} & \coth(kd)\end{bmatrix}\begin{bmatrix}\dfrac{\hat{K}^s}{jk}\\ \hat{\Psi}_k\end{bmatrix} \tag{21}$$

for components with dependence $\exp[j(\omega t - kz)]$ and

$$\begin{bmatrix}\mu_o H_x^s\\ \mu_o H_s^r\end{bmatrix} = \mu_o 3k\begin{bmatrix}-\coth(3kd) & \dfrac{1}{\sinh(3kd)}\\ \dfrac{-1}{\sinh(3kd)} & \coth(3kd)\end{bmatrix}\begin{bmatrix}0\\ \hat{\Psi}_{3k}\end{bmatrix} \tag{22}$$

for components with dependence $\exp 3j(\omega t - kz)$. The infinitely permeable material backing the stator current sheet requires that the third harmonic tangential field at the stator in Eq. 22a vanish.

The normal flux density $\mu_o H_x^s$ in Eq. 20 is a superposition of the components found using Eqs. 21a and 22a. Because it multiplies $\hat{\xi}$, $\hat{H}_x^r$ on the right in these expressions need only be evaluated to zero order in ξ. Thus, $\hat{H}_x^r$ is given by Eq. 21b with $\hat{\xi} = 0$, and hence $\hat{\Psi}_k = 0$. The second term in Eq. 19 also excites a field at the stator surface given by Eq. 22a. But, inserted into Eq. 20, this higher harmonic gives no space-average contribution and hence can be dropped. Thus, Eq. 20 becomes

$$f_z = A\left\langle \mathrm{Re}\left\{j\mu_o\coth(kd)\hat{K}^s + \frac{\mu_o k}{2}\left[\frac{-j(\hat{K}^s)^*\hat{\xi}}{\sinh^2(kd)}\right]\right\} e^{j(\omega t-kz)}\ \mathrm{Re}\left[\hat{K}^s e^{j(\omega t-kz)}\right]\right\rangle_z \tag{23}$$

The averaging theorem, Eq. 2.15.14, can now be applied to Eq. 23 to obtain the first of these relations:

$$f_z = \frac{\mu_o kA}{4\sinh^2(kd)}\mathrm{Re}\left[(\hat{K}^s)^2 j\hat{\xi}^*\right] \quad\Bigg|\quad f_z = \frac{-\varepsilon_o kA}{4\sinh^2(kd)}\mathrm{Re}\left[(k\hat{V}^s)^2 j\hat{\xi}^*\right] \tag{24}$$

The second expression pertains to the electric configuration of Part 4, Table 4.3.1, and has been obtained by recognizing that, in terms of the magnetic and electric potentials, the air-gap fields are analogous. The only difference is that in the magnetic case the stator magnetic potential is $\hat{K}^s/jk$, while in the electric case, the stator electric potential is $\hat{V}^s$. Hence, the electric time average force is found (using the complete analogy discussed at the beginning of Sec. 2.16) by replacing $\mu_o \to \varepsilon_o$ and $\hat{K}^s \to jk\hat{V}^s$ in Eq. 24a to obtain Eq. 24b.

As specific examples having the stator excitations and rotor position when t = 0 shown in Part 4 of Table 4.3.1, let

$$\xi = \xi_o \cos 2k[Ut - (z - \delta)] = Re\xi_o e^{2jk\delta} \exp[2jk(Ut - z)] \tag{25}$$

and

$$K^s = K_o^s \sin(\omega t - kz) = Re(-jK_o^s) \exp[j(\omega t - kz)] \quad \Big| \quad V^s = V_o^s \cos(\omega t - kz) = ReV_o^s \exp[j(\omega t - kz)] \tag{26}$$

where ξ_o, K_o^s and V_o^s are taken as real. Then, Eqs. 24 take the specific forms

$$f_z = -\frac{-\mu_o k(K_o^s)^2 \xi_o A}{4\sinh^2(kd)} \sin(2k\delta) \quad \Big| \quad f_z = \frac{-\varepsilon_o k(kV_o^s)^2 \xi_o A}{4\sinh^2(kd)} \sin(2k\delta) \tag{27}$$

The dependence of these forces on the spatial phase of stator excitations and rotor position, sketched in Table 4.3.1, is typical of salient-pole synchronous devices. That $\langle T_z \rangle_z$ has twice the periodicity in $k\delta$, obtained with the rotor excited directly by sources having the same periodicity as the stator excitations, is a direct consequence of the induced nature of the magnetization or polarization. Because the surface traction is proportional to the square of the local field, the same force is obtained if the rotor is shifted in relative position by $\delta = \pi/k$. The $[\sinh(kd)]^{-2}$ dependence of the force on the gap dimension d results because the only excitation is on the stator. By contrast with the synchronous interactions between excited stators and rotors [with (d) dependence $\sinh(kd)^{-1}$], here there is a round-trip attenuation of the excitation field, first in reaching the rotor surface and then in being reflected back to the stator.

Of the many configurations in the general family of "salient-pole" devices, two more are shown in Part 5 of Table 4.3.1. The magnetic case is considered in the problems, while the electric one is formally the same as if the rotor were perfectly polarizable. Hence it is also described by Eqs. 24b and 27b.

Practical devices make use of large amplitude saliency. One approach to obtaining an appropriate model is developed in Secs. 4.12 and 4.13, where the variable capacitance machine is considered in more detail.

4.4 Surface-Coupled Systems: A Permanent Polarization Synchronous Machine

With field sources modeled by surface charges or surface currents, it is natural to generalize the approach taken in Sec. 4.3 to the description of a wide class of complex electromechanically kinematic systems. The technique involves breaking the region of interest into source-free subregions that have uniform properties and hence can be described by the transfer relations of Sec. 2.16. Sources are then relegated to boundaries between subregions and are taken into account in the boundary conditions used to splice fields together. It is the objective in this section to illustrate the systematic approach that can be taken with such models by developing the lumped-parameter mechanical and electrical terminal relations for the rotating machine shown in Fig. 4.4.1.

The rotor consists of a material having polarization density that is uniform and permanent:

$$\vec{P} = P_o[\vec{i}_r \cos(\theta - \theta_r) - \vec{i}_\theta \sin(\theta - \theta_r)] = ReP_o(\vec{i}_r - j\vec{i}_\theta)e^{-j(\theta-\theta_r)} \tag{1}$$

Field coordinates are (r,θ) while $\theta_r(t)$ is the rotor axis. Thus, the polarization density is uniform and directed collinear with the rotor axis at the angle $\theta_r(t)$. The region between the rotor (with radius R) and the stator (radius R_o) is an air gap. Stator electrodes shown in the figure have respective potentials $\pm v(t)$ and are imbedded in a dielectric having permittivity ε_s. The length of the device in the z direction, ℓ, is considered large compared to the radial dimensions.

Within the rotor, there is no free charge density. Moreover, because the permanent polarization is uniform and hence has no divergence, Gauss' law (Eq. 2.3.27) reduces to

$$\nabla \cdot \varepsilon_o \vec{E} = 0 \tag{2}$$

Within the rotor, as well as in the air gap and in the surrounding dielectric of the stator, the fields are Laplacian. The transfer relations of Sec. 2.16 are directly applicable to describing the bulk fields

Boundary Conditions: The potential at $r = R_o$ is constrained to be $\pm v(t)$ on the respective portions of the stator surface covered by the electrodes. The potential between the electrodes on the dielectric surface at $r = R_o$ is approximated by the continuous linear distribution shown in Fig. 4.4.2.

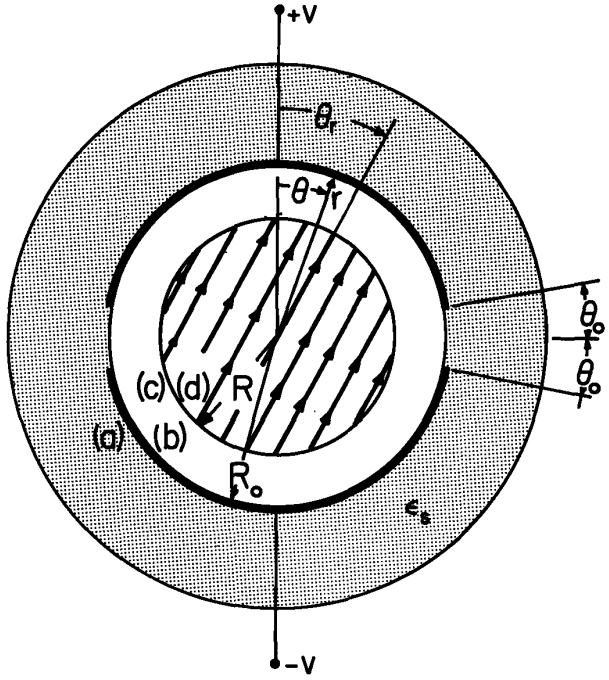

Fig. 4.4.1

Cross-sectional view of permanent polarization rotating machine.

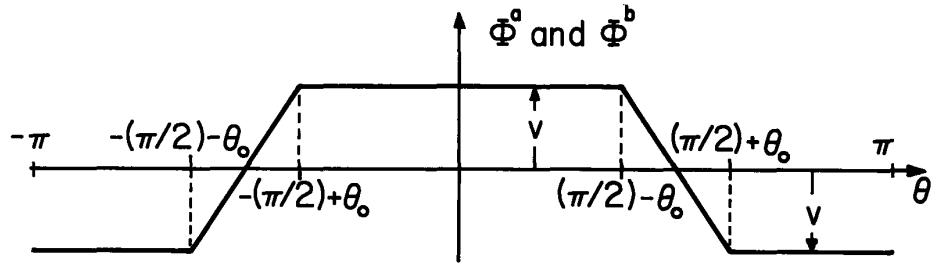

Fig. 4.4.2. Distribution of stator potential used to model the device shown in Fig. 4.4.1.

In Fig. 4.4.1, the notation (a)...(d) is used to denote positions adjacent to interfaces between regions. (This convention is introduced in Sec. 2.20.) Thus, the potential distribution of Fig. 4.4.2 is both Φ^a and Φ^b. In anticipation of the Laplacian solutions used to describe the bulk fields in cylindrical geometry, the potential of Fig. 4.4.2 is now expanded in a Fourier series (see Sec. 2.15 for a discussion of Fourier series):

$$\Phi^a = \Phi^b = \sum_{\substack{m=-\infty \\ (\text{odd})}}^{+\infty} \tilde{\Phi}^a_m(t)\, e^{-jm\theta};\quad \tilde{\Phi}^a_m = \frac{2v(t)}{m\pi}\,\frac{\sin(m\theta_o)}{\theta_o m}\,\sin\left(\frac{m\pi}{2}\right) \tag{1}$$

In the following it is assumed that the dielectric surrounding the rotor is of sufficient radius compared to R_o, that fields decay to zero before reaching the outer surface of the dielectric.

At the rotor air-gap interface the tangential $\vec{E}$ and hence the potential must be continuous. Thus the Fourier amplitudes are related by

$$\tilde{\Phi}^c_m = \tilde{\Phi}^d_m \tag{2}$$

In addition, Gauss' law (Eq. 2.10.21a) and Eq. 1 require that

$$\vec{n}\cdot\varepsilon_o [\![E]\!] = -\vec{n}\cdot [\![P]\!] \Rightarrow \varepsilon_o E_r^c - \varepsilon_o E_r^d = \mathrm{Re}(P_o e^{j\theta_r})e^{-j\theta} \tag{3}$$

This latter expression relates the Fourier amplitudes by

$$\varepsilon_o \tilde{E}_{rm}^c - \varepsilon_o \tilde{E}_{rm}^d = \frac{P_o}{2}\left[\delta_{1m} e^{j\theta_r} + \delta_{-1m} e^{-j\theta_r}\right] \tag{4}$$

where δ_{nm}, Kronecker's delta function, is unity for n = m and is otherwise zero.

Bulk Relations: The transfer relations, Eqs. (a) of Table 2.16.2 with k = 0, are now used to represent the fields at the boundaries. In the stator dielectric surrounding the electrodes ($r > R_o$), $\alpha \to \infty$ and $\beta = R_o$, while $\varepsilon \to \varepsilon_s$:

$$\varepsilon_s \tilde{E}_{rm}^a = \varepsilon_s f_m(\infty, R_o)\tilde{\Phi}^a \tag{5}$$

In the air gap ($R_o > r > R$), $\alpha \to R_o$, $\beta \to R$ and $\varepsilon \to \varepsilon_o$ so that

$$\begin{bmatrix} \varepsilon_o \tilde{E}_{rm}^b \\ \varepsilon_o \tilde{E}_{rm}^c \end{bmatrix} = \varepsilon_o \begin{bmatrix} f_m(R,R_o) & g_m(R_o,R) \\ g_m(R,R_o) & f_m(R_o,R) \end{bmatrix} \begin{bmatrix} \tilde{\Phi}_m^b \\ \tilde{\Phi}_m^c \end{bmatrix} \tag{6}$$

Finally, within the rotor ($r < R$) the relations are used with $\alpha = R$, $\beta \to 0$ and $\varepsilon \to \varepsilon_o$:

$$\varepsilon_o \tilde{E}_{rm}^d = \varepsilon_o f_m(0,R)\tilde{\Phi}_m^d \tag{7}$$

The boundary conditions given by Eqs. 2 and 4 and the bulk relations of Eqs. 5, 6 and 7 comprise six expressions that can be used to determine the Fourier amplitudes ($\tilde{\Phi}_m^c$, $\tilde{\Phi}_m^d$, $\tilde{E}_{rm}^c$, $\tilde{E}_{rm}^d$, $\tilde{E}_{rm}^a$, $\tilde{E}_{rm}^b$) with the driving amplitudes ($\tilde{\Phi}_m^a$, $\tilde{\Phi}_m^b$) given by Eq. 1. The solution for any one of the amplitudes is usually much easier than this statement makes it seem, but nevertheless it is worthwhile to have the objective of the model in view before proceeding further.

Torque as a Function of Voltage and Rotor Angle (v,θ_r): The rotor is enclosed by a surface at the radial position (c) in the air gap. The method using the Maxwell stress to compute the torque is as outlined in connection with Eq. 4.2.3. With the fields represented by Fourier series, Eq. 2.15.17 reduces the average of the shear stress over the enclosing surface to a summation on the products of the Fourier amplitudes:

$$\tau_z = R(2\pi R\ell)\left\langle D_r^c E_\theta^c \right\rangle_\theta = 2\pi R^2 \ell \sum_{m=-\infty}^{+\infty} (\varepsilon_o \tilde{E}_{rm}^c)^* \left(\frac{jm}{R}\tilde{\Phi}_m^c\right) \tag{8}$$

Substitution for $\varepsilon_o \tilde{E}_{rm}^c$ from Eq. 6b introduces the stator field, which is given by Eq. 1, and the same field $\tilde{\Phi}_m^c$ as already appears in Eq. 8. On physical grounds it is expected that this latter "self-field" term should not make a contribution. This is indeed the case, because f_m is an even function of m so that terms in $|\tilde{\Phi}_m^c|^2$ cancel out of the sum. The mth term is cancelled by the -mth term. Thus, Eq. 8 reduces to

$$\tau_z = 2\pi R^2 \ell \sum_{m=-\infty}^{\infty} \varepsilon_o g_m(R,R_o)(\tilde{\Phi}_m^b)^* \left(\frac{jm}{R}\tilde{\Phi}_m^c\right) \tag{9}$$

and all that is required to determine the torque is an evaluation of $\tilde{\Phi}_m^c$.

With this objective, substitution of Eqs. 6b and 7 into Eq. 4 with Eq. 2 used to replace $\tilde{\Phi}_m^d$ with $\tilde{\Phi}_m^c$ gives an expression that can be solved for $\tilde{\Phi}_m^c$:

$$\tilde{\Phi}_m^c = \frac{\frac{P_o}{2}\left[\delta_{1m} e^{j\theta_r} + \delta_{-1m} e^{-j\theta_r}\right] - \varepsilon_o g_m(R,R_o)\tilde{\Phi}_m^b}{\varepsilon_o [f_m(R_o,R) - f_m(0,R)]} \tag{10}$$

This expression and Eq. 1 in turn can be used to evaluate the torque, Eq. 9. (Again, because g_m and f_m

are even in m, the self-field terms sum to zero):

$$\tau_z(v,\theta_r) = \frac{-4R\ell g_1(R,R_o)}{f_1(R_o,R) - f_1(0,R)} \frac{\sin\theta_o}{\theta_o} v(t)P_o \sin\theta_r \tag{11}$$

In a lumped parameter model for the device, with v(t) and $\theta_r(t)$ functions of time determined by the external electrical and mechanical constraints, this relation represents the electrical-to-mechanical coupling. The reciprocal mechanical-to-electrical coupling completes the model.

Electrical Terminal Relations: To describe the electrical terminals, the total charge q on the respective electrodes is required, again as a function of the terminal variables (v,θ_r). The charge on the upper electrode is

$$q = \ell \int_{-\frac{\pi}{2}+\theta_o}^{\frac{\pi}{2}-\theta_o} (\varepsilon_s E_r^a - \varepsilon_o E_r^b) R_o d\theta = \ell \int_{-\frac{\pi}{2}+\theta_o}^{\frac{\pi}{2}-\theta_o} \sum_{m=-\infty}^{+\infty} (\varepsilon_s \tilde{E}_{rm}^a - \varepsilon_o \tilde{E}_{rm}^b) e^{-jm\theta} R_o d\theta$$

$$= \ell R_o \sum_{m=-\infty}^{+\infty} \frac{2}{m} (\varepsilon_s \tilde{E}_{rm}^a - \varepsilon_o \tilde{E}_{rm}^b) \sin m(\tfrac{\pi}{2} - \theta_o) \tag{12}$$

The electric flux normal to the outer and inner surfaces of the electrode are computed from Eqs. 5 and 6a, respectively:

$$\varepsilon_s \tilde{E}_{rm}^a - \varepsilon_o \tilde{E}_{rm}^b = \varepsilon_s f_m(\infty,R_o)\tilde{\Phi}^a - \varepsilon_o f_m(R,R_o)\tilde{\Phi}_m^b - \varepsilon_o g_m(R_o,R)\tilde{\Phi}_m^c \tag{13}$$

The amplitudes $(\tilde{\Phi}_m^a, \tilde{\Phi}_m^b)$ are given in terms of v(t) by Eq. 2, while $\tilde{\Phi}_m^c$ is given by Eq. 10. Thus Eq. 13 is evaluated in terms of (v,θ_r):

$$q = C_s v(t) - A_r P_o \cos\theta_r(t) \tag{14}$$

where C_s, the stator self-capacitance, is independent of θ_r and is

$$C_s = \frac{4\ell R_o}{\pi} \sum_{\substack{m=-\infty \\ \text{odd}}}^{+\infty} \frac{\sin m(\frac{\pi}{2} - \theta_o)}{m^2} \frac{\sin m\theta_o}{m\theta_o} \sin(\tfrac{m\pi}{2}) \left[\varepsilon_s f_m(\infty,R_o) - \varepsilon_o f_m(R,R_o) + \frac{\varepsilon_o g_m(R_o,R) g_m(R,R_o)}{f_m(R_o,R) - f_m(0,R)} \right] \tag{15}$$

and A_r is a constant having the units of area

$$A_r = \frac{2\ell R_o g_1(R_o,R)}{f_1(R_o,R) - f_1(0,R)} \cos\theta_o \tag{16}$$

The required electrical terminal relation is Eq. 14.

For reasons that stem from the approximations made in the field description, the model represented by Eqs. 11 and 14 is not self-consistent. At the dielectric air-gap interface between electrodes, the potential is continuous, but $\vec{n}\cdot[\![\vec{D}]\!]$ is not. In physical terms, this means that the fields are as though segmented electrodes existed at $r = R_o$ in these transition regions having the linear potential distribution of Fig. 4.4.2 and supporting a surface charge that can be computed from Eq. 13. This charge is not included in Eq. 14 and might for some purposes be ignored. But, if the mechanical and electrical terminal relations are used as stated, the electromechanical system, which after all does not include energy dissipating elements, is given a model that does not conserve energy. In fact, once the torque is known, energy conservation formalisms introduced in Sec. 3.5 not only provide an alternative to computing the electrical terminal relations, but lead to a self-consistent model and a recognition that Eq. 15 can be considerably simplified.

In terms of lumped parameters, the system can be pictured as having the terminal pairs of Fig. 4.4.3. The electrical terminal pairs are interconnected so that $v_1 = -v_2 = v$ and by symmetry,

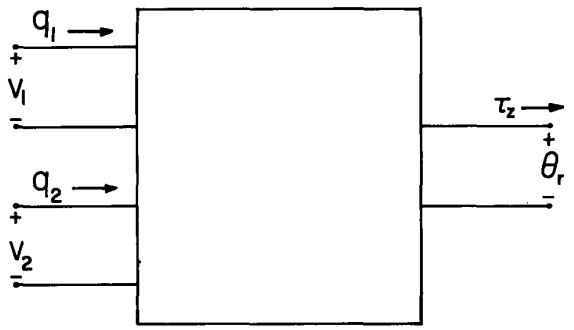

Fig. 4.4.3. Three-terminal pair lumped parameter system representing system of Fig. 4.4.1.

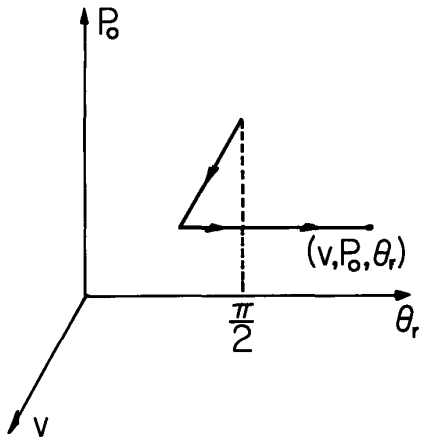

Fig. 4.4.4. State space integration contour.

$q_1 = -q_2 = q$. Thus, the incremental energy conservation equation is

$$\delta w = 2v\delta q - \tau_z d\theta_r \tag{17}$$

Not accessible through the external electrical terminals is the electric energy storage due to the permanent polarization. In Eq. 17 it is understood that P_o is held fixed. Transformation to a hybrid energy function $w''(v,P_o,\theta_r)$ is made by replacing $v\delta(2q) \rightarrow \delta(2qv) - 2q\delta v$ and defining $w'' = 2qv-w$, so that

$$\delta w'' = 2q\delta v + \tau_z d\theta_r \tag{18}$$

This expression is integrated on the state-space contour shown in Fig. 4.4.4. First, with the rotor at $\theta_r = \pi/2$, the polarization is brought up to its final state. Then the voltage is raised. Finally, with P_o and v held fixed, the rotor is turned to the angle θ_r of interest. With the rotor at $\theta_r = \pi/2$, the net charge induced on the upper electrode because of the polarization is zero. Hence, the net charge on the upper stator electrode is computed from Eq. 13, but with $\varepsilon_o E_r^b$ determined as if the rotor were not present. From Eq. 6,

$$\varepsilon_o \tilde{E}_{rm}^b = \varepsilon_o f_m(0,R_o)\tilde{\Phi}_m^b \tag{19}$$

Hence, Eq. 12 gives

$$q = C_s v; \quad C_s = \frac{4\ell R_o}{\pi} \sum_{\substack{m=-\infty \\ \text{odd}}}^{\infty} \frac{\sin m(\frac{\pi}{2} - \theta_o)}{m^2} \frac{\sin m\theta_o}{m\theta_o} \sin(\tfrac{m\pi}{2})[\varepsilon_s f_m(\infty,R_o) - \varepsilon_o f_m(0,R_o)] \tag{20}$$

In view of Eqs. 20 and 11, the integration of Eq. 18 on v and then on θ_r leads to

$$w'' = 2[\tfrac{1}{2} C_s v^2] + \left[\frac{4R\ell g_1(R,R_o)}{f_1(R_o,R) - f_1(0,R)} \frac{\sin\theta_o}{\theta_o}\right] vP_o \cos\theta_r \tag{21}$$

Finally, because $w'' = w''(v,P_o,\theta_r)$, the required terminal charge follows as

$$q = \frac{1}{2}\frac{\partial w''}{\partial v} = C_s v - A_r P_o \cos\theta_r \tag{22}$$

where

$$A_r = \frac{-2R\ell g_1(R,R_o)}{f_1(R_o,R) - f_1(0,R)} \frac{\sin\theta_o}{\theta_o} \tag{23}$$

and C_s is given by Eq. 20. Simplification of Eq. 15 leads to Eq. 20, but for the reasons discussed, Eqs. 16 and 23 differ by the factor $[\sin\theta_o/\theta_o]/\cos\theta_o$. The use of Eqs. 22 and 23 for the electrical terminal relation has the advantage that the model is then self-consistent in its representation of energy flow. The same advantage would exist if the energy relations were used to compute the electrical

torque from the electrical terminal relations. This more conventional technique would make use of Eq. 14 and an integration of Eq. 18 in the sequence, P_o, θ_r and v. To carry out the second leg of this integration without making a contribution requires that symmetry be used to argue that there is no electrical torque even though the rotor is polarized.

4.5 Constrained-Charge Transfer Relations

For field sources constrained in their relative distribution, the transfer relation approach can not only be used for sources confined to boundaries, but can also be used to describe interactions with sources distributed through the bulk of a subregion. The objective in this section is to develop the principles underlying this generalization of the transfer relations for electroquasistatic fields and to summarize useful relations. The method is extended to certain magnetoquasistatic systems in Sec. 4.7.

In a region having a given net charge density ρ and uniform permittivity ε, Gauss' law and the requirement of irrotationality for $\vec{E}$ (Eqs. 2.3.23a and 2.3.23b) show that the electric potential Φ must satisfy Poisson's equation:

$$\nabla^2\Phi = -\frac{\rho}{\varepsilon} \tag{1}$$

In solving this linear equation, consider the solution to be a superposition of a homogeneous part Φ_H satisfying Laplace's equation and a particular solution Φ_P which, at each point in the volume of interest, has a Laplacian $-\rho/\varepsilon$:

$$\Phi = \Phi_H + \Phi_P \tag{2}$$

It is this latter component that balances the "drive" provided by the charge density when the total solution Φ is inserted into Eq. 1. By definition

$$\nabla^2\Phi_P = -\frac{\rho}{\varepsilon} \tag{3}$$

$$\nabla^2\Phi_H = 0 \tag{4}$$

In the three standard coordinate systems, the particular solution can be written as a superposition of the same variable-separable solutions used in Sec. 2.16 for the homogeneous solution. Thus,

$$\Phi_P = \begin{cases} \text{Re } \tilde{\Phi}_P(x,t)\, \exp[-j(k_y y + k_z z)] & \text{(Cartesian)} \\ \text{Re } \tilde{\Phi}_P(r,t)\, \exp[-j(m\theta + kz)] & \text{(cylindrical)} \\ \text{Re } \tilde{\Phi}_P(r,t)\, P_n^m(\cos\theta)\, \exp[-jm\phi] & \text{(spherical)} \end{cases} \tag{5}$$

With n used to denote the normal component at the respective bounding surfaces of the region described by the transfer relations, the homogeneous transfer relations of Tables 2.16.1, 2.16.2 and 2.16.3 relate the components of the homogeneous part of the solutions evaluated at the respective surfaces. Thus, in these relations, the substitution is made

$$\begin{aligned} &\tilde{\Phi}^\alpha \to \tilde{\Phi}^\alpha_H = \tilde{\Phi}^\alpha - \tilde{\Phi}^\alpha_P; \quad \tilde{\Phi}^\beta \to \tilde{\Phi}^\beta_H = \tilde{\Phi}^\beta - \tilde{\Phi}^\beta_P \\ &\tilde{D}^\alpha_n \to \tilde{D}^\alpha_{nH} = \tilde{D}^\alpha_n - \tilde{D}^\alpha_{nP}; \quad \tilde{D}^\beta_n \to \tilde{D}^\beta_{nH} = \tilde{D}^\beta_n - \tilde{D}^\beta_{nP} \end{aligned} \tag{6}$$

The transfer relations, which take the general form of Eq. 2.17.6, therefore relate the new surface variables and the particular solution evaluated at the surfaces:

$$\begin{bmatrix} \tilde{\Phi}^\alpha - \tilde{\Phi}^\alpha_P \\ \tilde{\Phi}^\beta - \tilde{\Phi}^\beta_P \end{bmatrix} = \begin{bmatrix} -A_{11} & A_{12} \\ -A_{21} & A_{22} \end{bmatrix} \begin{bmatrix} \tilde{D}^\alpha_n - \tilde{D}^\alpha_{nP} \\ \tilde{D}^\beta_n - \tilde{D}^\beta_{nP} \end{bmatrix} \tag{7}$$

Multiplied out, the transfer relations for regions with a bulk distribution of charge are

$$\begin{bmatrix} \tilde{\Phi}^\alpha \\ \tilde{\Phi}^\beta \end{bmatrix} = \begin{bmatrix} -A_{11} & A_{12} \\ -A_{21} & A_{22} \end{bmatrix} \begin{bmatrix} \tilde{D}^\alpha_n \\ \tilde{D}^\beta_n \end{bmatrix} + \begin{bmatrix} \tilde{h}^\alpha \\ \tilde{h}^\beta \end{bmatrix} \tag{8}$$

where

$$\begin{bmatrix} \tilde{h}^{\alpha} \\ \tilde{h}^{\beta} \end{bmatrix} = \begin{bmatrix} \tilde{\Phi}_P^{\alpha} \\ \tilde{\Phi}_P^{\beta} \end{bmatrix} + \begin{bmatrix} A_{11}\tilde{D}_{nP}^{\alpha} - A_{12}\tilde{D}_{nP}^{\beta} \\ A_{21}\tilde{D}_{nP}^{\alpha} - A_{22}\tilde{D}_{nP}^{\beta} \end{bmatrix} \tag{9}$$

Associated with the surface variables related by these transfer relations are the bulk distributions of potential. These are obtained from the distributions of potential for no charge density by again using the substitutions summarized by Eq. 6. For example, in Cartesian coordinates, the potential distribution is the sum of Eq. 2.16.15 with $(\tilde{\Phi}^{\alpha},\tilde{\Phi}^{\beta})$ replaced by $(\tilde{\Phi}^{\alpha} - \tilde{\Phi}_P^{\alpha}, \tilde{\Phi}^{\beta} - \tilde{\Phi}_P^{\beta})$ and the particular solution.

$$\tilde{\Phi} = (\tilde{\Phi}^{\alpha} - \tilde{\Phi}_P^{\alpha}) \frac{\sinh \gamma x}{\sinh \gamma \Delta} - (\tilde{\Phi}^{\beta} - \tilde{\Phi}_P^{\beta}) \frac{\sinh \gamma(x - \Delta)}{\sinh \gamma \Delta} + \tilde{\Phi}_P(x) \tag{10}$$

The same substitution generalizes the cylindrical coordinate potentials, Eqs. 2.16.20, 2.16.21 and 2.16.25 as well as those in spherical coordinates, Eq. 2.16.36.

Particular Solutions (Cartesian Coordinates): Any Φ_p having the form of Eq. 5 can be used in Eqs. 8 and 9. "Inspection" yields solutions in many cases. However, it is often true that the most useful solutions belong to a class that can be generated by the procedure now illustrated in Cartesian coordinates.

Within the planar region (shown in Table 2.16.1) there is a charge distribution that has an arbitrary dependence on the transverse coordinate x but the y-z dependence of Eq. 5a for complex amplitude, Fourier series or Fourier transform representations:

$$\rho = \mathrm{Re} \sum_{i=0}^{\infty} \tilde{\rho}_i(t)\Pi_i(x)e^{-j(k_y y + k_z z)} \tag{11}$$

Here, the distribution has been represented as a superposition of modes $\Pi_i(x)$ having individual complex amplitudes $\tilde{\rho}_i(t)$. These as yet to be determined modes are defined such that the particular solution can be written as a superposition of the same modes:

$$\Phi_P = \mathrm{Re} \sum_{i=0}^{\infty} \tilde{\Phi}_i(t)\Pi_i(x)e^{-j(k_y y + k_z z)} \tag{12}$$

The same functions are used for both ρ and Φ_p because then substitution into Poisson's equation, Eq. 3, shows that a particular solution has been found, provided that the modes satisfy the Helmholtz equation:

$$\frac{d^2\Pi_i}{dx^2} + \nu_i^2\Pi_i = 0; \quad \nu_i^2 = \frac{\tilde{\rho}_i}{\varepsilon\tilde{\Phi}_i} - k_y^2 - k_z^2 \tag{13}$$

It follows from Eq. 13 that Π_i is a linear combination of $\sin(\nu_i x)$ and $\cos(\nu_i x)$. Boundary conditions, selected as a matter of convenience and to give orthogonal modes that can be used to expand an arbitrary charge distribution in a quickly convergent series, complete the specification of the modes. For example, the transfer relations, Eqs. 8 and 9, are simplified if

$$\tilde{D}_{nP}^{\alpha} \equiv -\varepsilon \left.\frac{d\tilde{\Phi}_P}{dx}\right|_{\alpha} = 0; \quad \tilde{D}_{nP}^{\beta} \equiv -\varepsilon \left.\frac{d\tilde{\Phi}_P}{dx}\right|_{\beta} = 0 \tag{14}$$

so these will be used as boundary conditions in solving Eq. 13. It follows that for a layer with α and β surfaces at $x = \Delta$ and $x = 0$, respectively,

$$\Pi_i = \cos \nu_i x; \quad \nu_i = \frac{i\pi}{\Delta}; \quad i = 0,1,2,\cdots \tag{15}$$

From the definition of ν_i, Eq. 13, the potential and charge-density amplitudes called for in Eqs. 11 and 12 are related by

$$\tilde{\Phi}_i = \frac{\tilde{\rho}_i}{\varepsilon(\nu_i^2 + k_y^2 + k_z^2)} \tag{16}$$

The charge-density amplitudes are determined from a given distribution Re $\tilde{\rho}(x,t)\exp[-j(k_y y + k_z z)]$ by a Fourier analysis. That is, Eq. 11 is multiplied by Π_k, integrated from $0 \to \Delta$, solved for $\tilde{\rho}_k$ and $k \to i$:

$$\tilde{\rho}_i = \frac{2}{\Delta}\int_o^\Delta \tilde{\rho}(x,t)\Pi_i(\nu_i x)dx;\ i \neq 0:\ \tilde{\rho}_o = \frac{1}{\Delta}\int_o^\Delta \tilde{\rho}\ (x,t)dx \tag{17}$$

The associated transfer relations, Eqs. 8 and 9 evaluated using Eqs. 12, 15 and 16, with A_{ij}'s from Table 2.16.1, become

$$\begin{bmatrix} \Phi^\alpha \\ \tilde{\Phi}^\beta \end{bmatrix} = \frac{1}{\varepsilon\gamma}\begin{bmatrix} -\coth\gamma\Delta & \frac{1}{\sinh\gamma\Delta} \\ \frac{-1}{\sinh\gamma\Delta} & \coth\gamma\Delta \end{bmatrix}\begin{bmatrix} \tilde{D}_x^\alpha \\ \tilde{D}_x^\beta \end{bmatrix} + \sum_{i=0}^{+\infty}\frac{\tilde{\rho}_i}{\varepsilon(\nu_i^2+\gamma^2)}\begin{bmatrix} (-1)^i \\ 1 \end{bmatrix} \tag{18}$$

The potential distribution is given in terms of these amplitudes and the particular solution (Eqs. 12, 15 and 16) by Eq. 10. Note that to make use of Eq. 10 the origin of the x axis need not be coincident with the β surface. The equation applies to a region with the β surface at x = a if the substitution is made $x \to x + a$.

Cylindrical Annulus: In cylindrical coordinates, the given charge distribution and particular solution take the form

$$\rho = \mathrm{Re}\sum_{i=0}^{\infty}\tilde{\rho}_i(t)\Pi_i(r)e^{-j(m\theta+kz)};\quad \Phi_P = \mathrm{Re}\sum_{i=0}^{\infty}\tilde{\Phi}_i(t)\Pi_i(r)e^{-j(m\theta+kz)} \tag{19}$$

Thus, Poisson's equation, Eq. 1, requires that

$$\frac{d^2\Pi_i}{dr^2} + \frac{1}{r}\frac{d\Pi_i}{dr} + \left(\nu_i^2 - \frac{m^2}{r^2}\right)\Pi_i = 0;\ \nu_i^2 \equiv \frac{\tilde{\rho}_i}{\varepsilon\tilde{\Phi}_i} - k^2 \tag{20}$$

and the potential amplitudes are related to the charge density amplitudes by

$$\tilde{\Phi}_i = \frac{\tilde{\rho}_i}{\varepsilon(\nu_i^2 + k^2)} \tag{21}$$

Boundary conditions used in selecting solutions to Eq. 20 might be selected analogous to those of Eq. 14. This would simplify the transfer relations, but require solution of a relatively complicated transcendental equation for the ν_i's. Instead, the particular solution is required to vanish on the outer surface only and solutions that are singular at the origin are excluded. In cylindrical coordinates this is sufficient to result in a complete set of orthogonal modes:

$$\tilde{D}_{rP}^\alpha = -\varepsilon\left.\frac{d\tilde{\Phi}_P}{dr}\right|_\alpha = 0 \tag{22}$$

Comparison of Eq. 20 to Eq. 2.16.19 shows that the solutions that are not singular at the origin are Bessel's functions of first kind and order m:

$$\Pi_i = J_m(\nu_i r) \tag{23}$$

To satisfy the boundary condition, Eq. 22, the ν_i's must be roots of

$$\nu_i J_m'(\nu_i \alpha) = 0 \tag{24}$$

In now evaluating the transfer relations, Eqs. 8 and 9, the normal flux density is zero at the α surface, but otherwise all of the particular solution entries make a contribution:

$$\begin{bmatrix} \tilde{\Phi}^{\alpha} \\ \tilde{\Phi}^{\beta} \end{bmatrix} = \frac{1}{\varepsilon} \begin{bmatrix} F_m(\beta,\alpha) & G_m(\alpha,\beta) \\ G_m(\beta,\alpha) & F_m(\alpha,\beta) \end{bmatrix} \begin{bmatrix} \tilde{D}_r^{\alpha} \\ \tilde{D}_r^{\beta} \end{bmatrix} + \sum_{i=0}^{\infty} \frac{\tilde{\rho}_i}{\varepsilon(\nu_i^2 + k^2)} \begin{bmatrix} J_m(\nu_i\alpha) + \nu_i G_m(\alpha,\beta) J_m'(\nu_i\beta) \\ J_m(\nu_i\beta) + \nu_i F_m(\alpha,\beta) J_m'(\nu_i\beta) \end{bmatrix} \tag{25}$$

An important limiting case is $\beta \to 0$ so that the region is a "solid" cylinder. This limit is most conveniently taken by first using the limiting form of the transfer relation, Eq. (b) of Table 2.16.2, which becomes

$$\tilde{\Phi}^{\alpha} - \tilde{\Phi}_P^{\alpha} = \frac{1}{\varepsilon} F_m(0,\alpha)[\tilde{D}_r^{\alpha} - \tilde{D}_{rP}^{\alpha}] \tag{26}$$

Put in the form of Eq. 25, the transfer relation for a solid cylinder is

$$\tilde{\Phi}^{\alpha} = \frac{1}{\varepsilon} F_m(0,\alpha)\tilde{D}_r^{\alpha} + \sum_{i=0}^{\infty} \frac{\tilde{\rho}_i}{\varepsilon(\nu_i^2 + k^2)} J_m(\nu_i\alpha) \tag{27}$$

The charge-density amplitudes $\tilde{\rho}_i$ are evaluated in terms of the given charge distribution by exploiting the orthogonality of the Π_i's.

Orthogonality of Π_i's and Evaluation of Source Distributions: The given transverse distribution of ρ is used to evaluate the mode amplitudes, $\overline{\Pi}_i(x)$ or $\overline{\Pi}_i(r)$ and hence $\tilde{\rho}_i$. Because the particular solutions are in each case a superposition of solutions to the Helmholtz equation, with appropriate boundary conditions, the eigenmodes Π_i are orthogonal. In the Cartesian coordinate cases, this means that

$$\int_0^{\Delta} \Pi_i(\nu_i x)\Pi_j(\nu_j x)dx = \frac{\Delta}{2}\delta_{ij} \tag{28}$$

This relation is the basis for evaluating the Fourier coefficients, for example Eq. 17. Proof of orthogonality and determination of the coefficients is possible in this case by direct integration. But, in the circular geometry, a more powerful method is needed, one based on the properties of $\Pi_i(\nu_i r)$ that can be deduced from the differential equation and boundary conditions. The proof of orthogonality and determination of the normalizing factor is as follows.

Multiply Eq. 20 by $r\Pi_j$ and integrate from the origin to the outer radius. The first term can then be integrated by parts to obtain

$$r\Pi_j(\nu_j r)\frac{d\Pi(\nu_i r)}{dr}\bigg|_0^{\alpha} - \int_0^{\alpha} r\frac{d\Pi_i(\nu_i r)}{dr}\frac{d\Pi_j(\nu_j r)}{dr}dr + \int_0^{\alpha} r(\nu_i^2 - \frac{m^2}{r^2})\Pi_i\Pi_j dr = 0 \tag{29}$$

This expression also holds with i and j reversed. The latter equation, subtracted from Eq. 29, gives

$$(\nu_i^2 - \nu_j^2)\int_0^{\alpha} r\Pi_i\Pi_j\,dr = r\Pi_i\frac{d\Pi_j}{dr}\bigg|_0^{\alpha} - r\Pi_j\frac{d\Pi_i}{dr}\bigg|_0^{\alpha} \tag{30}$$

Thus, it is clear that either for $\Pi_i = 0$ or $d\Pi_i/dr = 0$ at $r = \alpha$, the functions Π_i and Π_j are orthogonal in the sense that the integral appearing in Eq. 30 vanishes provided $i \neq j$.

The value of the integral for $i = j$ is required in evaluating the coefficients in the charge density expansion, and is deduced by taking the limit where $\nu_j \to \nu_i$, or $\Delta\nu \to 0$ in $(\nu_j = \nu_i + \Delta\nu)$

$$\Pi_j(\nu_j r) = \Pi_j[\nu_i r + (\Delta\nu)r] \simeq \Pi_j(\nu_i r) + [\Pi_j'(\nu_i r)]r\Delta\nu \tag{31}$$

Again, the prime indicates a derivative with respect to the argument $(\nu_j r)$. Expansion of Eq. 31 to first order in $\Delta\nu$ shows that in the limit $\Delta\nu \to 0$,

$$\int_0^{\alpha} r\Pi_i\Pi_j dr = \delta_{ij}\frac{\alpha^2}{2}\left\{[\Pi_i'(\nu_i\alpha)]^2 + [1 - \frac{m^2}{(\nu_i\alpha)^2}]\Pi_i^2(\nu_i\alpha)\right\} \tag{32}$$

In obtaining this result, the fact that Π_i satisfies Bessel's equation, Eq. 20, has again been used to

substitute for Π_i'' in terms of Π_i and Π_i'.

An example exploiting the cylindrical constrained-charge transfer relations and orthogonality relations is developed in Sec. 4.6.

4.6 Kinematics of Traveling-Wave Charged-Particle Devices

Synchronous interactions between a "stator" potential wave and a traveling wave of charge are abstracted in Part 3 of Table 4.3.1. In the most common practical devices exploiting such electric interactions, the space-charge wave is itself created by the electromechanical interaction between a structure potential and a uniformly charged beam. These examples are not "kinematic" in the sense that the relative distribution of space charge cannot be prescribed. Nevertheless, by representing the interaction as though independent control can be obtained over the beam and structure traveling waves, the energy conversion principles are highlighted. In addition, this section illustrates how the constrained-charge transfer relations of Sec. 4.5 are put to work. Self-consistent interactions through electrical stresses will be developed in Chaps. 5 and 8.

In the model shown in Fig. 4.6.1, the space-charge wave has the shape of a circular cylinder of radius R and charge density

$$\rho = -\rho_B \cos(\omega t - kz + k\delta) = \mathrm{Re}\ \tilde{\rho} \exp(-jkz);\ \tilde{\rho} \equiv [-\rho_B \exp(jk\delta)] \exp(j\omega t) \qquad (1)$$

where ρ_B is a constant.

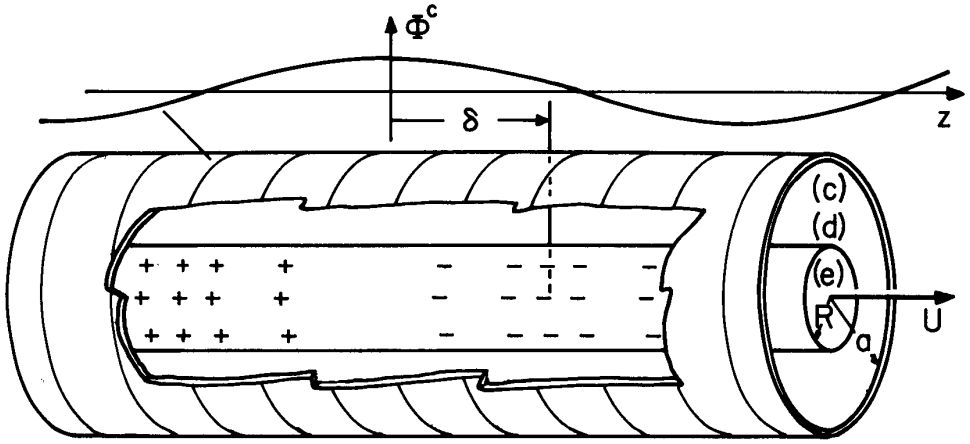

Fig. 4.6.1. Regions of positive and negative charge represent concentrations and rarefactions in the local charge density of an initially uniformly charged beam moving in the z direction with the velocity U.

In an electron beam device,[1] the stream is initially of uniform charge density. But, perhaps initiated by means of a modulating field introduced upstream, the particles become bunched. The resulting space charge can be viewed as the superposition of uniform and periodic space-charge components. The uniform component gives rise to an essentially radial field which tends to spread the beam. (Through the $q\vec{v} \times \vec{B}$ force attending any radial motion of the particle, a longitudinal magnetic field is often used to confine the beam and prevent its spreading. In any case, here the effect of this radial field is considered negligible.)

In traveling-wave beam devices, the interaction is with a traveling wave of potential on a slow-wave (perhaps helical) structure, such as that shown schematically in Fig. 4.6.2a. The structure is designed to propagate an electromagnetic wave with velocity less than that of light, so that it can be in synchronism with the space-charge wave. For the present purposes, this potential is imposed on a wall at r = c:

$$\Phi^c = V_o \cos(\omega t - kz) = \mathrm{Re}\tilde{V}_o e^{-jkz};\ \tilde{V}_o = V_o e^{j\omega t} \qquad (2)$$

In the kinematic model of Fig. 4.6.1, the coupling can either retard or accelerate the beam, depending on whether operation is akin to a generator or motor (Table 4.3.1). Traveling-wave electron beam amplifiers and oscillators are generators, in that they convert the steady kinetic energy of the beam to an a-c electrical output. The result of the interaction is a time-average retarding force that tends

---

1. Basic electron beam electromechanics are discussed in the text Field and Wave Electrodynamics, by Curtis C. Johnson, McGraw-Hill Book Company, New York, 1965, p. 275.

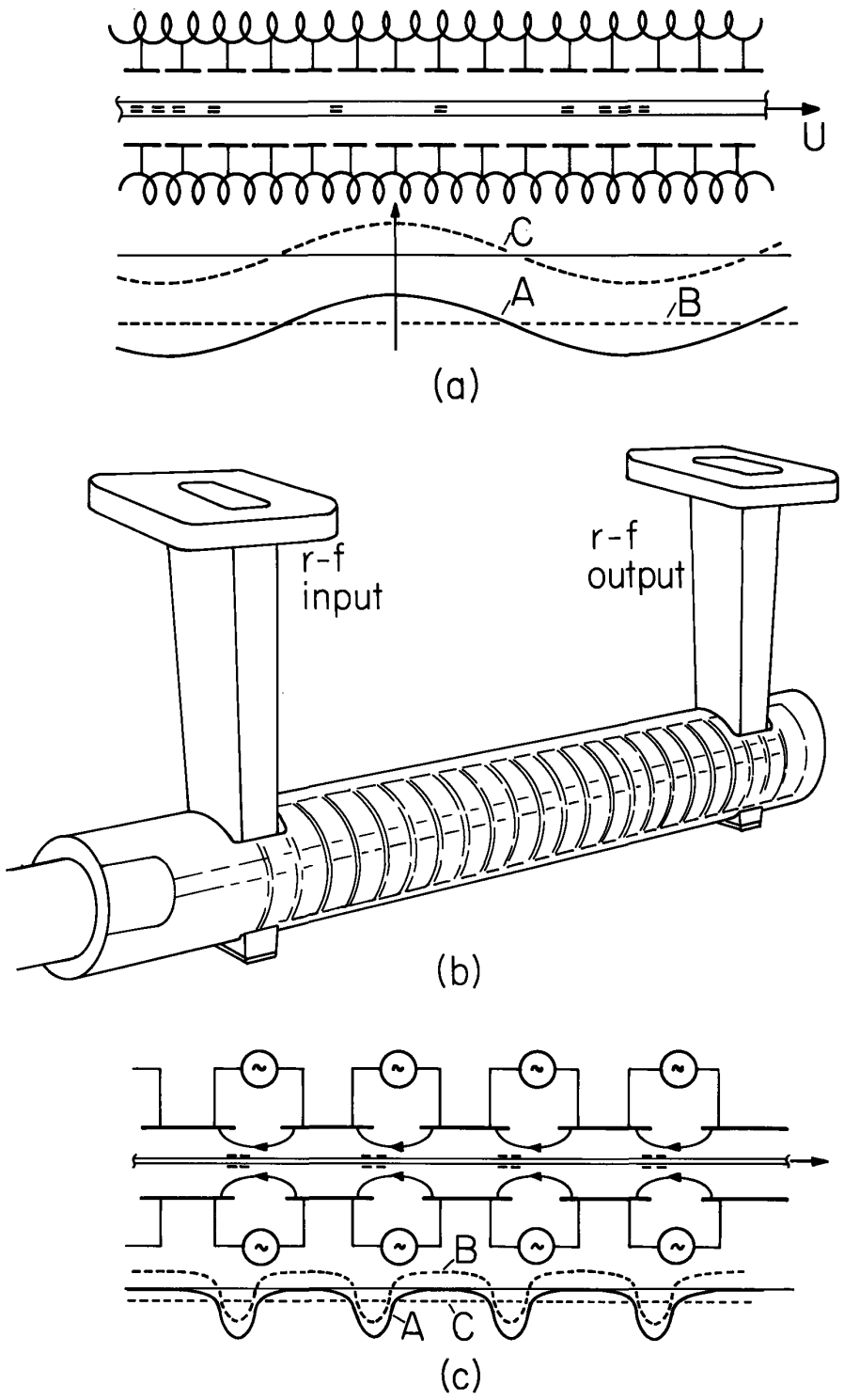

Fig. 4.6.2. (a) Schematic representation of traveling-wave electron beam device with slow-wave structure modeled by distributed circuit coupled to beam through the electric field. Below structure is distribution of space charge in the beam (A), and the equivalent distribution of a uniform charge density (B) and a periodic distribution (C). (b) Combination cutaway and phantom view of low-noise low-power traveling-wave tube that operates in part of the frequency range 2 to 40 GHz. (c) Schematic of linear accelerator designed so that oscillating gap voltages "kick" particles as they pass. Shown below are "bunches" of particles and hence space charge (A) and the equivalent superposition of periodic and uniform parts (B) and (C).

to slow the beam.

The "motor" of particle beam devices is the particle accelerator typified by Fig. 4.6.2c. Here, the object is to accelerate bunches of particles to extremely high velocities by subjecting them to alternating electric fields phased in such a way that when a bunch arrives at an accelerating gap, the fields tend to give it an additional "kick" in the axial direction.[2] The complex fields associated with the traveling particle bunches and accelerating fields are typically represented as traveling waves, as suggested by Fig. 4.6.2c. The principal periodic component of the space-charge wave is represented in the model of Fig. 4.6.1.

In this section it is presumed that the particle velocities are unaffected by the interaction; U is a constant. In fact, the object of the generator is to slow the beam, and of the accelerator is to increase the velocity; a more refined analysis is likely to be required for particular design purposes.

In yet another physical situation, the constraints on mechanical motion and wall potentials assumed in this section are imposed. At low frequencies and velocities, it is possible to deposit charge on a moving insulating material. Then, the relative charge velocity is known. Moreover, at low frequencies it is possible to use segmented electrodes and voltage sources to impose the postulated potential distribution.

As will be seen, at low velocities it is difficult to achieve competitive energy conversion densities using macroscopic electric forces. So, at low frequencies, the class of devices discussed in this section might be used as high-voltage generators rather than as generators of bulk power.

The net force on a section of the beam having length ℓ is found by integrating the stress over a surface adjacent to the outer wall (see Fig. 4.2.1b for detailed discussion of this step):

$$f_z = 2\pi a\ell\left\langle D_r^c E_z^c \right\rangle_z = \pi a\ell \mathrm{Re}[(\tilde{D}_r^c)^* jk\tilde{V}_o] \tag{3}$$

To compute $\tilde{D}^c$, and hence f_z, the potential is related to the normal electric flux and charge density by the transfer relation for a "solid" cylinder of charge, Eq. 4.5.27 with m = 0:

$$\tilde{\Phi}^\alpha = \frac{1}{\varepsilon_o} F_o(0,\alpha)\tilde{D}_r^\alpha + \sum_{i=0}^{\infty} \frac{\tilde{\rho}_i J_o(\nu_i \alpha)}{\varepsilon_o(\nu_i^2 + k^2)} \tag{4}$$

Table 2.16.2 summarizes $F_o(0,\alpha)$.

Single-Region Model: It is instructive to consider two alternative ways of representing the fields. First, consider that the beam and the surrounding annular region comprise a single region with a charge density distribution as sketched in Fig. 4.6.3. Then, in Eq. 4, the radius $\alpha = a$ and the position $(\alpha) \to (c)$. Multiplication of Eq. 4.5.19a by $r\Pi_j(\nu_j r)$ and integration $0 \to a$ then gives

$$\int_o^R \tilde{\rho} r J_o(\nu_j r)dr = \sum_{i=0}^{\infty} \tilde{\rho}_i \int_o^a r J_o(\nu_i r) J_o(\nu_j r)dr \tag{5}$$

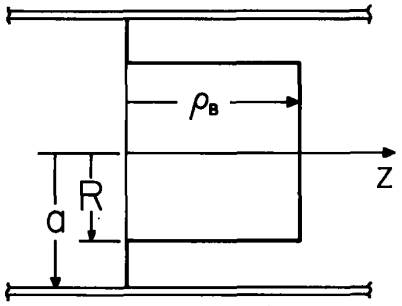

Fig. 4.6.3
Radial distribution of charge density.

The right-hand side is integrated using Eq. 4.5.32, while the left-hand side is an integral that can be evaluated from tables or by using the fact that $J_o(\nu_i r)$ satisfies Eq. 4.5.20 with m = 0 and Eq. 2.16.26c holds for J_o:

$$\tilde{\rho}\frac{R}{\nu_j} J_1(\nu_j R) = \tilde{\rho}_j \frac{a^2}{2} J_o^2(\nu_j a) \Rightarrow \tilde{\rho}_i = \frac{2\tilde{\rho}RJ_1(\nu_i R)}{\nu_i a^2 J_o^2(\nu_i a)};\ i \neq 0 \tag{6}$$

2. A discussion of synchronous-type particle accelerators is given in Handbook of Physics, E. U. Condon and H. Odishaw, eds., McGraw-Hill Book Company, New York, 1958, pp. 9-156.

The root $\nu_i = 0$ to Eq. 4.5.24 is handled separately in integrating Eq. 5. In that case $J_o = 1$ and $\tilde{\rho}_o = R^2\tilde{\rho}/a^2$.

Because $\tilde{\Phi}^c = \tilde{V}_o$, Eq. 4 can now be solved for $\tilde{D}_r^c$:

$$\tilde{D}_r^c = \varepsilon F_o^{-1}(0,a)\left\{\tilde{V}_o - \tilde{\rho}\left[\frac{R^2}{\varepsilon(ak)^2} + \sum_{i=1}^{\infty}\frac{2RJ_1(\nu_i R)}{\varepsilon\nu_i a^2(\nu_i^2 + k^2)J_o(\nu_i a)}\right]\right\} \tag{7}$$

It follows from Eq. (3) that, for the distribution of charge and structure potential given by Eqs. 1 and 2, the required force on a length ℓ of the beam is

$$f_z = -(\pi R^2 \ell)(kV_o\rho_B \sin k\delta)L_1 \tag{8}$$

where

$$L_1 = -\frac{a}{R}\left\{\left(\frac{R}{a}\right)\frac{1}{(ak)^2} + \sum_{i=1}^{\infty}\frac{2J_1[(\nu_i a)\frac{R}{a}]}{(\nu_i a)[(\nu_i a)^2 + (ak)^2]J_o(\nu_i a)}\right\} aF_o^{-1}(0,a)$$

Hence, the force has the characteristic dependence on the spatial phase shift between structure potential and beam space-charge waves identified for synchronous interactions in Sec. 4.3.

Two-Region Model: Consider next the alternative description. The region is divided into a part having radius R and described by Eq. 4 (with the position $\alpha \to e$ and radius $\alpha \to R$) and an annulus of free space. Because the charge density is uniform over the inner region, only the $i = 0$ term (having the eigenvalue $\nu_o = 0$) in the series of Eq. 4.5.1 is required to exactly describe the charge and potential distributions. With variables labeled in accordance with Fig. 4.6.1, Eq. 4 becomes

$$\tilde{\Phi}^e = \frac{D_r^e F_o(0,R)}{\varepsilon} + \frac{\tilde{\rho}}{\varepsilon k^2} \tag{9}$$

The annular region of free space is described by Eqs. (a) of Table 2.16.2:

$$\begin{bmatrix}\tilde{D}_r^c \\ \tilde{D}_r^d\end{bmatrix} = \varepsilon\begin{bmatrix}f_o(R,a) & g_o(a,R) \\ g_o(R,a) & f_o(a,R)\end{bmatrix}\begin{bmatrix}\tilde{\Phi}^c \\ \tilde{\Phi}^d\end{bmatrix} \tag{10}$$

Boundary conditions splice the regions together:

$$\tilde{\Phi}^c = \tilde{V}_o,\ \tilde{\Phi}^d = \tilde{\Phi}^e,\ \tilde{D}_r^d = \tilde{D}_r^e \tag{11}$$

In view of these conditions, Eqs. 9 and 10b combine to show that

$$\tilde{\Phi}^d = \frac{g_o(R,a)\tilde{V}_o + \tilde{\rho}\,F_o^{-1}(0,R)\varepsilon^{-1}k^{-2}}{F_o^{-1}(0,R) - f_o(a,R)} \tag{12}$$

From Eq. 10a $\tilde{D}_r^c$ can be found and the force, Eq. 3, evaluated. The result is the same as Eq. 8 except that L_1 is replaced by

$$L_2 = \frac{[ag_o(a,R)][aF_o^{-1}(0,R)]}{(ka)^2(\frac{R}{a})^2[aF_o^{-1}(0,R) - af_o(a,R)]} = \frac{1}{kR}\frac{I_o'(kR)}{I_o(ka)} \tag{13}$$

To obtain the second expression, note that the reciprocity condition, Eq. 2.17.10, requires that $ag_o(a,R) = -Rg_o(R,a)$.

Numerically, Eqs. 8 and 13 are the same. They are identical in form in the limit where the charge completely fills the region $r<a$, as can be seen by taking the limit $R \to a$ in each expression

$$L_1 \to L_2 = -\frac{aF_o^{-1}(0,a)}{(ak)^2} \tag{14}$$

In the example considered here the second representation gives the simpler result. But, if the splicing approach exemplified by Eq. 13 were used to represent a more complicated radial distribution of charge, the clear advantage would be with the single region representation illustrated by Eq. 8.

The dependence of L_2 on the wavenumber normalized to the wall radius is shown in Fig. 4.6.4. As would be expected, the coupling to the wall becomes weaker with increasing k (decreasing wavelength). The part of the coupling represented by L_2 also becomes smaller as the beam becomes more confined to the center. Note however that there is an R^2 factor in Eq. 8 that makes the effect of decreasing R much stronger than reflected in L_2 (or L_1) alone.

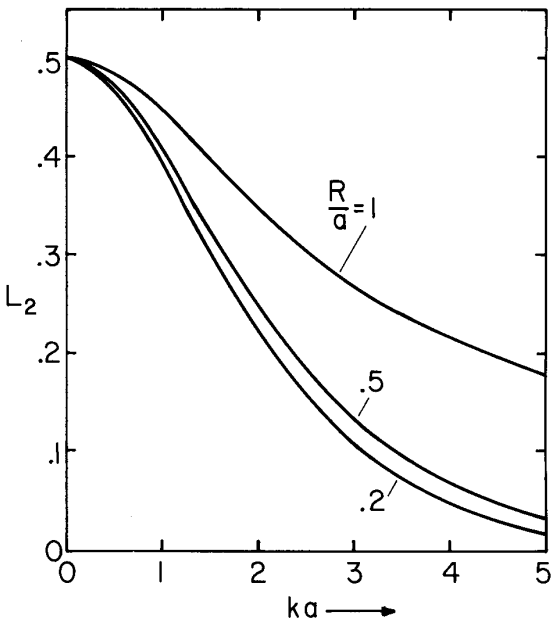

Fig. 4.6.4. Function L_2 defined by Eq. 4.6.8.

4.7 Smooth Air-Gap Synchronous Machine Model

A specific result in this section is the terminal relations that constitute the lumped-parameter model for a three-phase two-pole smooth air-gap synchronous machine. The derivations are aimed at exemplifying the pattern that can be followed in describing a wide class of magnetic field devices modeled by coupling at surfaces.

In the cross-sectional view of the smooth air-gap machine shown in Fig. 4.7.1a, the stator structure consists of a laminated circular cylindrical material having permeability μ_s with outside radius a and inner radius b. Imbedded in slots on this inner surface are three windings, having turns densities that vary sinusoidally with θ. These slots are typically as shown in Fig. 4.7.2b, where the laminations used for construction of rotor and stator for the generator of Fig. 4.7.2a are pictured. Only one of these stator windings is shown in Fig. 4.7.1, the "a" phase with its magnetic axis at $\theta = -90^o$. The "b" and "c" phases are similarly distributed but rotated so that their magnetic axes are respectively at the angles 30^o and 150^o. Thus the peak surface current density for the respective windings comes at the angles $\theta = 0$, $\theta = 120^o$, and $\theta = 240^o$. These stator windings have peak turns densities N_a, N_b, N_c, respectively, and carry the terminal currents (i_a, i_b, i_c). Because the stator windings essentially form a current sheet at the radius b, their contribution to the field is modeled by the surface current density

$$K_z^s = i_a(t)N_a \cos\theta + i_b(t)N_b \cos(\theta - \tfrac{2\pi}{3}) + i_c(t)N_c \cos(\theta - \tfrac{4\pi}{3}) = \mathrm{Re}\,\tilde{K}^s e^{-j\theta};\ \tilde{K}^s = i_a N_a + i_b N_b e^{j(\frac{2\pi}{3})} + i_c N_c e^{j(\frac{4\pi}{3})} \quad (1)$$

There is only one phase on the rotor, consisting of sinusoidally distributed windings of peak turns density N_r excited through slip rings by the terminal current i_r. With the rotor angular position denoted by θ_r, the rotor current is modeled by a surface current density at r = c of

$$K_z^r = i_r(t)N_r \cos(\theta - \theta_r) = \mathrm{Re}\,\tilde{K}^r e^{-j\theta};\ \tilde{K}^r = i_r N_r e^{j\theta_r} \quad (2)$$

These excitations have been written in the complex amplitude notation. Fields in each region are described by the polar coordinate transfer relations of Table 2.19.1 with m = 1.

The objective in the following calculations is to relate the electrical and mechanical terminal relations so that electromechanical coupling, represented schematically in Fig. 4.7.3, is specified in the form

$$\begin{bmatrix} \lambda_a \\ \lambda_b \\ \lambda_c \\ \lambda_r \end{bmatrix} = \begin{bmatrix} L_{aa} & L_{ab} & L_{ac} & L_{ar} \\ L_{ba} & L_{bb} & L_{bc} & L_{br} \\ L_{ca} & L_{cb} & L_{cc} & L_{cr} \\ L_{ra} & L_{rb} & L_{rc} & L_{rr} \end{bmatrix} \begin{bmatrix} i_a \\ i_b \\ i_c \\ i_r \end{bmatrix} \quad (3)$$

$$\tau_z = \tau_z(i_a, i_b, i_c, i_r, \theta_r) \quad (4)$$

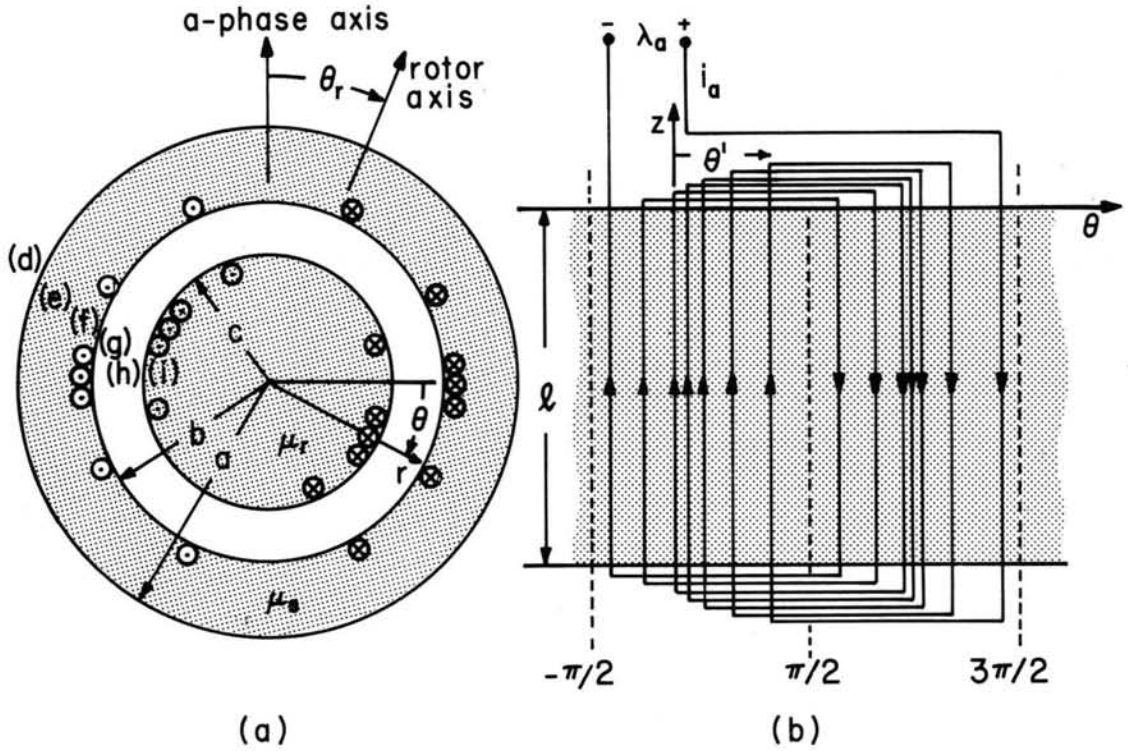

Fig. 4.7.1. (a) Cross-sectional view of smooth air-gap synchronous machine showing only one of three phases on stator. (b) Distribution of "a"-phase windings on stator as seen looking radially inward.

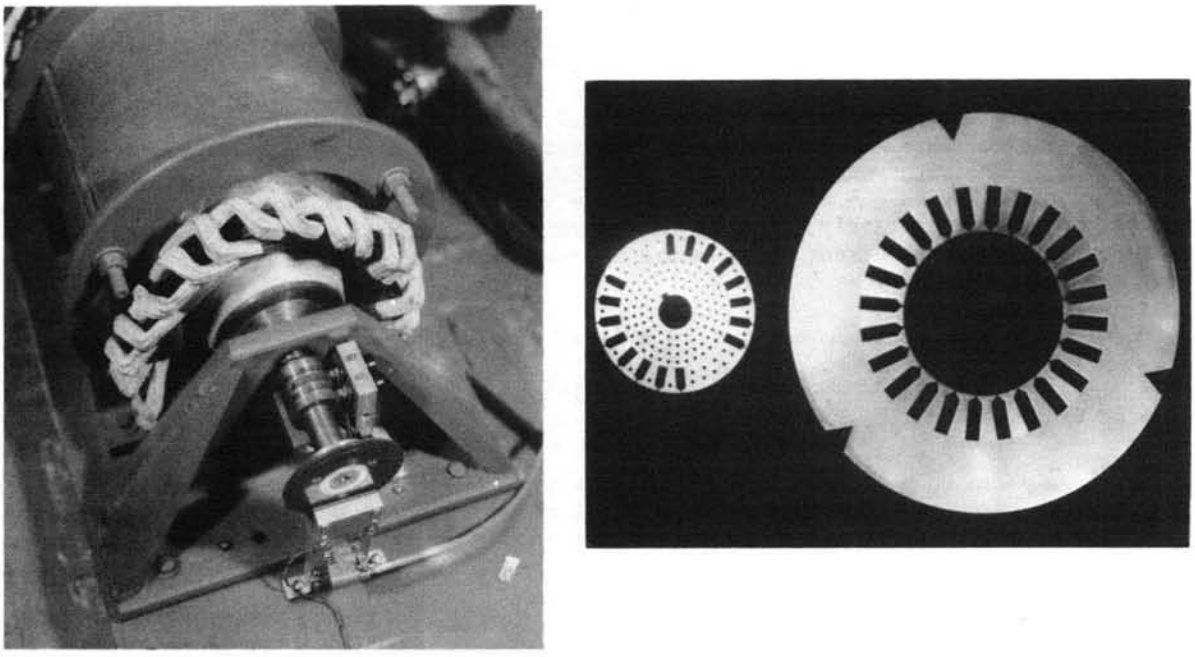

(a) (b)

Fig. 4.7.2. (a) Model synchronous alternator having rating of about one kVA and modeling 900 MVA machine. Unit is one of several used in MIT Electric Power Systems Engineering Laboratory as part of model power system. Slip rings for supplying field current are on shaft near bearing. Disk with holes is for measurement of angular position of rotor. (b) Rotor and stator laminations used for model machine of (a). Rectangular slots carry windings. Conducting rods inserted through the circular holes in the rotor are shorted at the ends of the rotor to simulate transient eddy-current (induction machine) effects in full-scale machine. The scaling requires that the model have extremely narrow air gap of about 0.23 mm, as compared to the gap of about 7 cm in the full-scale machine.

Boundary Conditions: The field excitations represented by Eqs. 1 and 2, written in complex-amplitude notation, can be matched by single components of the fields represented in each region by the polar coordinate transfer relations of Table 2.19.1. In view of the θ dependence of the current sheets, m = 1.

Positions adjacent to the boundaries between current-free regions of uniform permeability in Fig. 4.7.1a are denoted by (d) - (i). Fields are assumed to vanish far from the outer surface. At each surface, the normal flux density is continuous (Eq. 2.10.22). This means that the vector potential is continuous, and hence

$$\tilde{A}^d = \tilde{A}^e \tag{5}$$

$$\tilde{A}^f = \tilde{A}^g \tag{6}$$

$$\tilde{A}^h = \tilde{A}^i \tag{7}$$

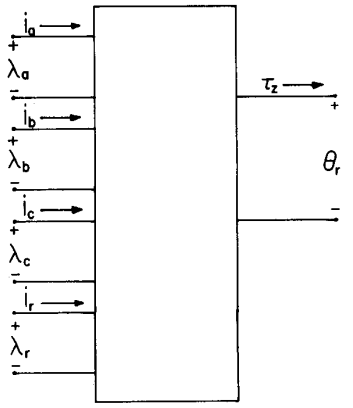

Fig. 4.7.3. Electromechanical coupling network for system of Fig. 4.7.1.

The jump in the tangential field intensity is equal to the surface current density (Eq. 2.10.21), and hence

$$\tilde{H}_\theta^d - \tilde{H}_\theta^e = 0 \tag{8}$$

$$\tilde{H}_\theta^f - \tilde{H}_\theta^g = \tilde{K}^s \tag{9}$$

$$\tilde{H}_\theta^h - \tilde{H}_\theta^i = \tilde{K}^r \tag{10}$$

Bulk Relations: Each of the uniform regions is described by Eq. (c) of Table 2.19.1. In the exterior region, $\alpha \to \infty$, $\beta = a$, and $\mu = \mu_o$

$$\tilde{H}_\theta^d = \frac{1}{\mu_o} f_1(\infty,a)\tilde{A}^d \tag{11}$$

In the stator, $\alpha = a$, $\beta = b$, and $\mu = \mu_s$:

$$\begin{bmatrix} \tilde{H}_\theta^e \\ \tilde{H}_\theta^f \end{bmatrix} = \frac{1}{\mu_s}\begin{bmatrix} f_1(b,a) & g_1(a,b) \\ g_1(b,a) & f_1(a,b) \end{bmatrix}\begin{bmatrix} \tilde{A}^e \\ \tilde{A}^f \end{bmatrix} \tag{12}$$

In the air gap, $\alpha = b$, $\beta = c$, and $\mu = \mu_o$:

$$\begin{bmatrix} \tilde{H}_\theta^g \\ \tilde{H}_\theta^h \end{bmatrix} = \frac{1}{\mu_o}\begin{bmatrix} f_1(c,b) & g_1(b,c) \\ g_1(c,b) & f_1(b,c) \end{bmatrix}\begin{bmatrix} \tilde{A}^g \\ \tilde{A}^h \end{bmatrix} \tag{13}$$

and finally, in the rotor, $\alpha = c$, $\beta \to 0$, and $\mu = \mu_r$:

$$\tilde{H}_\theta^i = \frac{1}{\mu_r} f_1(0,c)\tilde{A}^i \tag{14}$$

Torque as a Function of Terminal Currents and Rotor Angle: With the surface of integration for the stress tensor just inside the stator, it follows from Eq. 4.2.3 that the rotor torque is

$$\tau_z = (2\pi b^2 \ell)\frac{1}{2}\mathrm{Re}\left[(\tilde{H}_\theta^g)^* \tilde{B}_r^g\right] = \pi b^2 \ell \mathrm{Re}\left[(\tilde{H}_\theta^g)^* \left(\frac{-j\tilde{A}^g}{b}\right)\right] \tag{15}$$

It will be seen shortly that the electrical terminal relations can be computed from $\tilde{A}^g$. It is therefore convenient to also express Eq. 15 in terms of $\tilde{A}^g$ and the given surface currents. To this end, Eqs. 5 and 8 are used to replace (d) → (e) in Eq. 11, while Eqs. 6 and 9 are used to replace $\tilde{H}_\theta^f$ and $\tilde{A}^f$ in Eq. 12b. Thus, Eqs. 12 can be solved for $\tilde{H}_\theta^g$ as a function of $\tilde{K}^s$ and $\tilde{A}^g$:

$$\tilde{H}_\theta^g = -\tilde{K}^s + \frac{\tilde{A}^g}{\mu_s}\left\{ f_1(a,b) + \frac{g_1(b,a)g_1(a,b)}{\left[\frac{\mu_s}{\mu_o} f_1(\infty,a) - f_1(b,a)\right]} \right\} \tag{16}$$

Because the geometric quantity multiplying $\tilde{A}^g$ is real, it is clear that substitution of Eq. 16 into Eq. 15 gives only

$$\tau_z = \pi b \ell \mathrm{Re}[(\tilde{K}^s)^* j\tilde{A}^g] \tag{17}$$

To evaluate $\tilde{A}^g$ in terms of $\tilde{K}^s$ and $\tilde{K}^r$ (and hence in terms of the terminal currents and θ_r), Eqs. 7 and 10 are used in Eq. 14, which is solved for $\tilde{H}^h$. This latter quantity is substituted into Eq. 13b. Simultaneous solution of Eqs. 13 then gives a second expression for $\tilde{H}_\theta^g$:

$$\tilde{H}_\theta^g = \frac{\tilde{K}^r g_1(b,c)}{f_1(b,c) - \frac{\mu_o}{\mu_r} f_1(0,c)} + \frac{\tilde{A}^g}{\mu_o}\left\{ f_1(c,b) + \frac{g_1(b,c)g_1(c,b)}{\frac{\mu_o}{\mu_r} f_1(0,c) - f_1(b,c)} \right\} \tag{18}$$

By equating Eqs. 16 and 18, it is now possible to solve for $\tilde{A}^g$ in terms of the surface currents:

$$\tilde{A}^g = \frac{\mu_o}{D}\tilde{K}^s + \frac{\mu_o g_1(b,c)}{D[f_1(b,c) - \frac{\mu_o}{\mu_r} f_1(0,c)]}\tilde{K}^r \tag{19}$$

where

$$D \equiv \frac{\mu_o}{\mu_s}\left\{ f_1(a,b) + \frac{g_1(b,a)g_1(a,b)}{\left[\frac{\mu_s}{\mu_o} f_1(\infty,a) - f_1(b,a)\right]} \right\} - \left\{ f_1(c,b) + \frac{g_1(b,c)g_1(c,b)}{\left[\frac{\mu_o}{\mu_r} f_1(0,c) - f_1(b,c)\right]} \right\}$$

A methodical approach to solving the boundary and bulk relations is suited to those comfortable with the reduction of determinants or inclined to use matrix computations. Following this alternative, the boundary conditions, Eqs. 5 to 10, are used to eliminate the "d", "f", and "i" variables in the bulk relations, Eqs. 11 to 14. These latter equations are then written in the form

$$\begin{bmatrix}
-1 & \frac{1}{\mu_o} f_1(\infty,a) & 0 & 0 & 0 & 0 \\
-1 & \frac{1}{\mu_s} f_1(b,a) & 0 & \frac{1}{\mu_s} g_1(a,b) & 0 & 0 \\
0 & \frac{1}{\mu_s} g_1(b,a) & -1 & \frac{1}{\mu_s} f_1(a,b) & 0 & 0 \\
0 & 0 & -1 & \frac{1}{\mu_o} f_1(c,b) & 0 & \frac{1}{\mu_o} g_1(b,c) \\
0 & 0 & 0 & \frac{1}{\mu_o} g_1(c,b) & -1 & \frac{1}{\mu_o} f_1(b,c) \\
0 & 0 & 0 & 0 & -1 & \frac{1}{\mu_r} f_1(0,c)
\end{bmatrix}
\begin{bmatrix} \tilde{H}_\theta^e \\ \tilde{A}^e \\ \tilde{H}_\theta^g \\ \tilde{A}^g \\ \tilde{H}_\theta^h \\ \tilde{A}^h \end{bmatrix}
=
\begin{bmatrix} 0 \\ 0 \\ \tilde{K}^s \\ 0 \\ 0 \\ -\tilde{K}^r \end{bmatrix} \tag{20}$$

Cramer's rule is then used to deduce $\tilde{A}^g$, Eq. 19.

Substitution of Eq. 19 into the torque expression, Eq. 17, shows that

$$\tau_z = \frac{\pi b \ell \mu_o}{D[f_1(b,c) - \frac{\mu_o}{\mu_r} f_1(0,c)]} \mathrm{Re}[j\tilde{K}^r(\tilde{K}^s)^*] \tag{21}$$

It follows from Eqs. 1 and 2 that the torque, expressed in terms of the terminal currents, is

$$\tau_z = \frac{-\pi b \ell \mu_o g_1(b,c)}{D[f_1(b,c) - \frac{\mu_o}{\mu_r} f_1(0,c)]} i_r N_r [i_a N_a \sin\theta_r + i_b N_b \sin(\theta_r - \tfrac{2\pi}{3}) + i_c N_c \sin(\theta_r - \tfrac{4\pi}{3})] \tag{22}$$

Electrical Terminal Relations: The flux linked by one turn of the "a"-phase coil running in the +z direction at $\theta = \theta'$ and returning in the -z direction at $\theta = \theta' + \pi$ is

$$\Phi_\lambda = \ell[A(b,\theta') - A(b,\theta' + \pi)] = \ell \mathrm{Re}\tilde{A}^g[e^{-j\theta'} - e^{-j(\theta'+\pi)}] \tag{23}$$

Here, use has been made of the relation between the vector potential and the flux, as described in Sec. 2.18 (Eq. (f) of Table 2.18.1).

The flux linked by the turns in the azimuthal interval $bd\theta'$ is then $\Phi_\lambda(bd\theta' N_a \cos\theta')$, and the total flux linked by the "a" phase is

$$\lambda_a = -b\ell N_a \int_{-\pi/2}^{\pi/2} \mathrm{Re}\,\frac{1}{2}\,[e^{j\theta'} + e^{-j\theta'}]\tilde{A}^g[\underbrace{e^{j\pi}}_{-1} - 1]e^{-j\theta'}d\theta' = \ell b N_a \pi \mathrm{Re}\tilde{A}^g \tag{24}$$

Substitution of $\tilde{A}^g$ from Eq. 19 and the surface currents from Eqs. 1 and 2 then gives the terminal relation for the "a" phase, in the form of Eq. 3a, where

$$L_{aa} = \frac{\pi\ell b\mu_o N_a^2}{D},\quad L_{ab} = -\frac{\pi\ell b\mu_o N_a N_b}{2D},\quad L_{ac} = -\frac{\pi\ell b\mu_o N_a N_c}{2D},\quad L_{ar} = L_o \ell b N_a N_r \cos\theta_r;$$

$$L_o \equiv \frac{\pi\mu_o g_1(b,c)}{D[f_1(b,c) - \frac{\mu_o}{\mu_r} f_1(0,c)]} \tag{25}$$

By symmetry, the inductances for the "b" and "c" phases are obtained without carrying out the evaluation by simply replacing indices in Eq. 25. For the "b" phase, replace indices $a \to b$, $b \to c$, $c \to a$, and $\theta_r \to \theta_r - 2\pi/3$ and for the "c" phase, $a \to c$, $b \to a$, $c \to b$, and $\theta_r \to \theta_r - 4\pi/3$.

The remaining flux linkage, λ_r, is computed by first recognizing that the flux linked by one turn on the rotor winding running in the z direction at θ' and returning at $\theta' + \pi$ is

$$\Phi_\lambda = -\ell \mathrm{Re}\tilde{A}^h[e^{j\pi} - 1]e^{-j\theta'} \tag{26}$$

Hence, the total flux linking the rotor winding is

$$\lambda_r = \int_{\theta_r - \frac{\pi}{2}}^{\theta_r + \frac{\pi}{2}} N_r \cos(\theta' - \theta_r)\Phi_\lambda c d\theta' = N_r c \ell \pi \mathrm{Re}\tilde{A}^h e^{j\theta_r} \tag{27}$$

The vector potential amplitude required to evaluate this expression follows from Eqs. 7, 10, 13b, and 14:

$$\tilde{A}^h = \frac{g_1(c,b)\tilde{A}^g - \mu_o \tilde{K}^r}{\frac{\mu_o}{\mu_r} f_1(0,c) - f_1(b,c)} \tag{28}$$

where $\tilde{A}^g$ is again Eq. 19, and the surface currents are evaluated in terms of the terminal currents using Eqs. 1 and 2. Thus, with the use of the transfer function reciprocity relation, $cg_1(c,b) = -bg_1(b,c)$, Eq. 2.17.10,

$$L_{ra} = L_o \ell b N_r N_a \cos\theta_r,\quad L_{rb} = L_o \ell b N_r N_b \cos(\theta_r - \tfrac{2\pi}{3}),\quad L_{rc} = L_o \ell b N_r N_c \cos(\theta_r - \tfrac{4\pi}{2}),$$

$$L_{rr} = L_o \ell b N_r^2 \left\{ \frac{g_1(b,c)}{D[f_1(b,c) - \frac{\mu_o}{\mu_r} f_1(0,c)]} - \frac{1}{g_1(c,b)} \right\} \tag{29}$$

Energy Conservation: Because the electromechanical coupling network represented by Fig. 4.7.3 is conservative, there is considerable redundancy in the terminal relations that have been derived. Conservation of energy requires that (Eq. 3.5.7 applied to a magnetic system)

$$\delta w' = \lambda_a \delta i_a + \lambda_b \delta i_b + \lambda_c \delta i_c + \lambda_r \delta i_r + \tau_z \delta \theta_r \tag{30}$$

From the assumption that w' is a state function, it follows that (see Eq. 3.5.4)

$$\lambda_k = \frac{\partial w'}{\partial i_k};\ k = a,b,c,r;\ \tau_z = \frac{\partial w'}{\partial \theta_r} \tag{31}$$

Lumped-parameter reciprocity conditions are generated by taking cross-derivatives of these relations:

$$\frac{\partial \lambda_k}{\partial i_\ell} = \frac{\partial \lambda_\ell}{\partial i_k};\ \frac{\partial \tau_z}{\partial i_k} = \frac{\partial \lambda_\ell}{\partial \theta_r};\ \begin{cases} k = a,b,c,r \\ \ell = a,b,c,r \end{cases} \tag{32}$$

The four relations among the electrical terminal variables show that

$$L_{k\ell} = L_{\ell k} \tag{33}$$

and these conditions are met by the results summarized by Eqs. 25 and the subsequent substitution of indices and Eq. 29. The reciprocity conditions between the torque and the flux linkages, Eq. 32, is also satisfied by Eqs. 22 and Eqs. 25 and 29. Note that to make it clear that the lumped-parameter reciprocity relations are satisfied, the reciprocity condition for the air-gap transfer relations was used in writing Eq. 29.

4.8 Constrained-Current Magnetoquasistatic Transfer Relations

By way of exemplifying how transfer relations can be used to represent fields in bulk regions, including volume distributions of known current density, these relations are derived in this section for one important class of physical situations. The current density (which is typically the result of exciting distributions of wire) is z-directed, while the magnetic field is in the (r,θ) plane. Thus, the relations are directly applicable to rotating machines with negligible end effects. Such an application is taken up in the next section.

In a broad sense, the objective in this section is to magnetic field systems what the objective in Sec. 4.5 was to electric field systems. But, the solution of the vector Poisson's equation, Eq. 2.19.2, is more demanding than the scalar Poisson's equation, Eq. 4.5.1, and hence the technique now illustrated is limited to certain configurations in which only one component of the vector potential describes the fields. Such cases are discussed in Sec. 2.18 and the associated transfer relations for a region of free space are derived in Sec. 2.19. The following discussion relates to the polar-coordinate situations of Tables 2.18.1 and 2.19.1.

In the two-dimensional cylindrical coordinates, the vector Poisson's equation (Eq. 2.19.2) has only a z component and the Laplacian is the same as the scalar Laplacian:

$$\nabla^2 A = -\mu J_z \tag{1}$$

Following the line of attack used in Sec. 4.5, the solution is divided into homogeneous and particular parts,

$$A = A_H + A_P \tag{2}$$

defined such that

$$\nabla^2 A_P = -\mu J_z;\ \nabla^2 A_H = 0 \tag{3}$$

The imposed current is now represented in the complex amplitude form

$$J_z = \mathrm{Re}\tilde{J}(r,t)e^{-jm\theta} \tag{4}$$

Of course, by superposition, such solutions could be the basis for a Fourier representation of an arbitrary current distribution. Substitution of Eq. 4 into Eq. 3 shows that $\tilde{A}_p$ must satisfy the equation

$$\frac{d^2\tilde{A}_P}{dr^2} + \frac{1}{r}\frac{d\tilde{A}_P}{dr} - \frac{m^2}{r^2}\tilde{A}_P = -\mu\tilde{J}(r) \tag{5}$$

The particular solution can be any solution to Eq. 5. The magnetic field associated with this particular

solution is, by the definition of the vector potential (Eq. 2.18.1),

$$H_{\theta P} = -\frac{1}{\mu}\frac{d\tilde{A}_P}{dr};\ \tilde{B}_{rP} = -\frac{jm}{r}\tilde{A}_P \tag{6}$$

From Eq. 2 it follows that the homogeneous solution is the total solution with the particular solution subtracted off. That is,

$$\tilde{A}_H = \tilde{A} - \tilde{A}_P;\ \tilde{H}_{\theta H} = \tilde{H}_\theta - \tilde{H}_{\theta P} \tag{7}$$

The homogeneous parts are related by the transfer relations, Eqs. (d) of Table 2.19.1, so that substitution from Eq. 7 shows that

$$\begin{bmatrix} \tilde{A}^\alpha - \tilde{A}_P^\alpha \\ \tilde{A}^\beta - \tilde{A}_P^\beta \end{bmatrix} = \mu \begin{bmatrix} F_m(\beta,\alpha) & G_m(\alpha,\beta) \\ G_m(\beta,\alpha) & F_m(\alpha,\beta) \end{bmatrix} \begin{bmatrix} \tilde{H}_\theta^\alpha - \tilde{H}_{\theta P}^\alpha \\ \tilde{H}_\theta^\beta - \tilde{H}_{\theta P}^\beta \end{bmatrix} \tag{8}$$

These relations, multiplied out, are the transfer relations for the cylindrical annulus supporting a given distribution of z-directed current density:

$$\begin{bmatrix} \tilde{A}^\alpha \\ \tilde{A}^\beta \end{bmatrix} = \mu \begin{bmatrix} F_m(\beta,\alpha) & G_m(\alpha,\beta) \\ G_m(\beta,\alpha) & F_m(\alpha,\beta) \end{bmatrix} \begin{bmatrix} \tilde{H}_\theta^\alpha \\ \tilde{H}_\theta^\beta \end{bmatrix} + \begin{bmatrix} \tilde{A}_P^\alpha \\ \tilde{A}_P^\beta \end{bmatrix} - \mu \begin{bmatrix} F_m(\beta,\alpha) & G_m(\alpha,\beta) \\ G_m(\beta,\alpha) & F_m(\alpha,\beta) \end{bmatrix} \begin{bmatrix} \tilde{H}_{\theta P}^\alpha \\ \tilde{H}_{\theta P}^\beta \end{bmatrix} \tag{9}$$

Following the format used in Sec. 4.5, it would be natural to now proceed to generate particular solutions that form a complete set of orthogonal functions which are solutions to the Helmholtz equation. Such an approach to evaluating the particular solutions in Eq. 9 is required if an arbitrary radial distribution of current density is to be represented. The approach parallels that presented in Sec. 4.5.

In important physical configurations, to which the remainder of this section is confined, the radial distribution is uniform:

$$\tilde{J}(r) = \tilde{J} \tag{10}$$

Fortunately, inspection of Eq. 5 in this case yields simple particular solutions:

$$\tilde{A}_P = \mu\tilde{J}\begin{cases} \dfrac{r^2}{m^2-4}; & m \neq 2 \\ -\dfrac{1}{4}r^2 \ln r; & m = \pm 2 \end{cases} \tag{11}$$

Thus, for the case of a radially uniform current density distribution, substitution of Eq. 11 into Eq. 9 yields the transfer relations

$$\begin{bmatrix} \tilde{A}^\alpha \\ \tilde{A}^\beta \end{bmatrix} = \mu_o \begin{bmatrix} F_m(\beta,\alpha) & G_m(\alpha,\beta) \\ G_m(\beta,\alpha) & F_m(\alpha,\beta) \end{bmatrix} \begin{bmatrix} \tilde{H}_\theta^\alpha \\ \tilde{H}_\theta^\beta \end{bmatrix} + \mu_o\tilde{J} \begin{bmatrix} h_m(\alpha,\beta) \\ h_m(\beta,\alpha) \end{bmatrix} \tag{12}$$

where

$$h_m(x,y) = \begin{cases} \dfrac{1}{m^2-4}\left[x^2 + 2xF_m(y,x) + 2yG_m(x,y)\right]; & m \neq 2 \\ \dfrac{x}{8}\left[x + g_m(x,y)y^2 \ln\left(\dfrac{x}{y}\right)\right]; & m = \pm 2 \end{cases}$$

and the functions F_m, G_m, and g_m are defined in Table 2.16.2 with k = 0.

The radial distribution of A within the volume of the annular region described by Eq. 12 is obtained by adding to the homogeneous solution, which is Eq. 2.19.5 with $\tilde{A}^\alpha \to \tilde{A}^\alpha - \tilde{A}^\alpha_p$, and $\tilde{A}^\beta \to \tilde{A}^\beta - \tilde{A}^\beta_p$, the particular solution $\tilde{A}_p$:

$$\tilde{A} = (\tilde{A}^\alpha - \tilde{A}^\alpha_p)\frac{\left[(\frac{\beta}{r})^m - (\frac{r}{\beta})^m\right]}{\left[(\frac{\beta}{\alpha})^m - (\frac{\alpha}{\beta})^m\right]} + (\tilde{A}^\beta - \tilde{A}^\beta_p)\frac{\left[(\frac{r}{\alpha})^m - (\frac{\alpha}{r})^m\right]}{\left[(\frac{\beta}{\alpha})^m - (\frac{\alpha}{\beta})^m\right]} + \tilde{A}_p \qquad (13)$$

For Eq. 12, the particular solution is given by Eq. 11, so the associated volume distribution is evaluated using Eq. 11.

The constrained-current transfer relations are applied to a specific problem in the next section.

4.9 Exposed Winding Synchronous Machine Model

The structure shown in cross section in Fig. 4.9.1 consists of a stator supporting three windings (a,b,c) and a rotor with a single winding (r). It models a three-phase two-pole synchronous alternator, and is similar to the configuration taken up in Sec. 4.7. The difference is that the windings on both rotor and stator are not embedded in slots of highly permeable material and take up a radial thickness that is appreciable compared to the air gap. As a result, the surface current model used in Sec. 4.7 is not appropriate.

The configuration considered here is an example to which the constrained-current transfer relations of Sec. 4.8 can be applied. It closely resembles models that have been developed for synchronous alternators making use of superconducting field (rotor) windings.[1] With superconductors, it is possible to generate magnetic fields that more than saturate magnetizable materials. As a result, the magnetic materials in which conductors are embedded in conventional machines can be dispensed with. This makes it possible to design for greater voltages than would be possible in a conventional machine, where the slot material in which a conductor is embedded must be grounded. But, because the conductors are exposed to the full magnetic force, methods of construction must be radically altered. A machine built

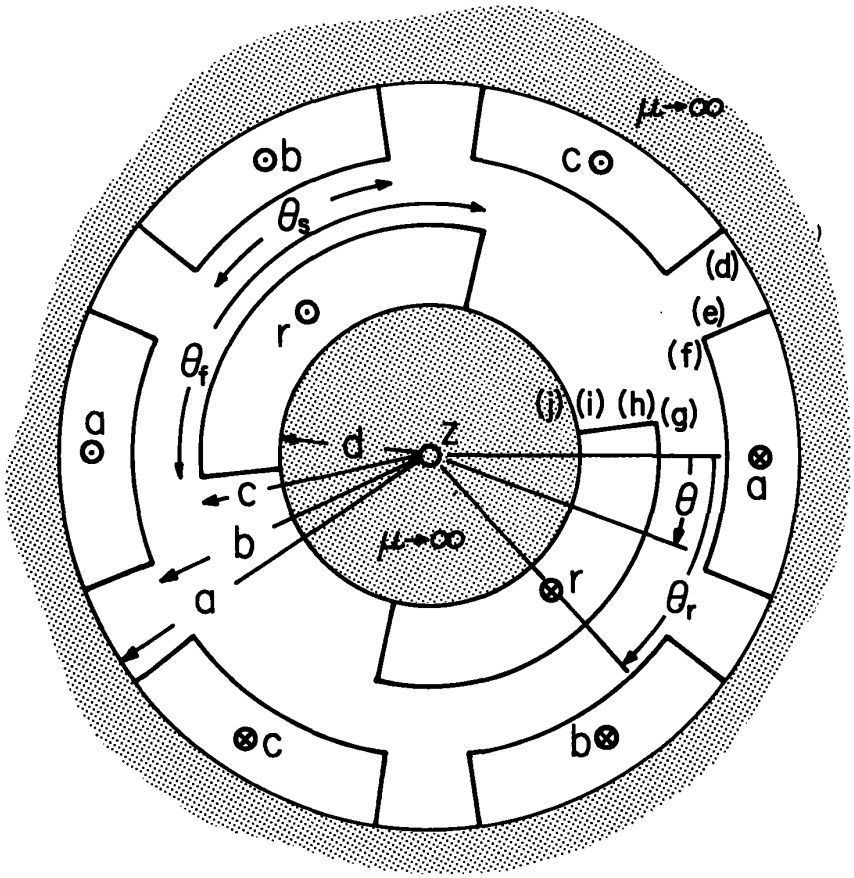

Fig. 4.9.1.

Cross section of synchronous machine model typifying structure used in superconducting field alternator.

1. J. L. Kirtley, Jr., "Design and Construction of an Armature for an Alternator with a Superconducting Field Winding," Ph.D. Thesis, Department of Electrical Engineering, Massachusetts Institute of Technology, Cambridge, Mass., 1971; J. L. Kirtley, Jr., and M. Furugama, "A Design Concept for Large Superconducting Alternators," IEEE Power Engineering Society, Winter Meeting, New York, Jan. 1975.

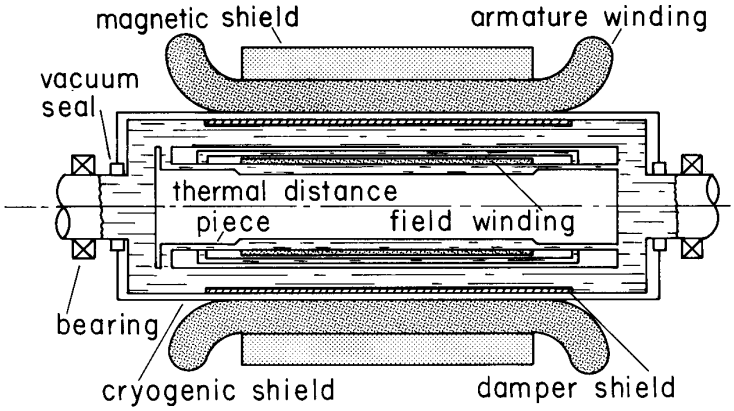

Fig. 4.9.2. Cross section of superconducting field alternator projected in design for 1000 and 10,000 MVA machines on basis of M.I.T. experiments on 2-3 MVA.[1] Not included in model of this section is conducting shell between rotor and stator to help prevent time-varying fields due to transients from reaching superconductors. Also, magnetic core of rotor used to simplify model in this section is not present in machine shown. Phenolic materials are used in projected design to construct stator and rotor.

to test approaches to constructing a rotating "refrigerator" required if the field is to be superconducting is shown in Fig. 4.9.2.

In the configuration considered here, it is assumed that surrounding the stator is a highly permeable shield material with inner radius (a) equal to the outer radius of the stator windings. Similarly, the rotor windings are bounded from inside by a "perfectly" permeable core. The magnetic materials are introduced into the model to make the example reasonably free of algebraic complications. In a machine having a superconducting field, a magnetic core would not be used. Development of a model without the magnetic rotor core follows the same pattern as now described.

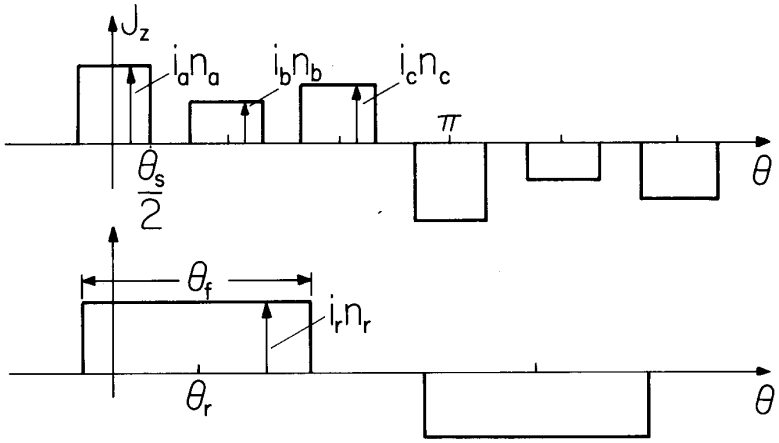

Fig. 4.9.3
Azimuthal current density distribution on stator and rotor.

The distribution of stator and rotor current densities with azimuthal position is shown in Fig. 4.9.3. The turns densities (n_a,n_b,n_c,n_r) (conductors per unit area) respectively carry the terminal currents (i_a,i_b,i_c,i_r). The conductors are unformly distributed. Hence, these current

density distributions can be represented by the Fourier series

$$J_z^s = \sum_{m=-\infty}^{+\infty} \tilde{J}_m^s e^{-jm\theta}, \quad b < r < a; \quad J_z^r = \sum_{m=-\infty}^{+\infty} \tilde{J}_m^r e^{-jm\theta}, \quad d < r < c \tag{1}$$

For the stator winding, the Fourier amplitudes are (Sec. 2.15)

$$\tilde{J}_m^s = \begin{cases} \dfrac{2}{\pi m} \sin\left(\dfrac{m\theta_s}{2}\right)\left[i_a n_a + i_b n_b e^{\frac{jm\pi}{3}} + i_c n_c e^{\frac{jm2\pi}{3}}\right]; & \text{m odd} \\ 0 \quad ; & \text{m even} \end{cases} \tag{2}$$

while on the rotor the amplitudes are

$$\tilde{J}_m^r = \begin{cases} \dfrac{2}{\pi m} \sin\left(\dfrac{m\theta_f}{2}\right) i_r n_r e^{jm\theta_r}; & \text{m odd} \\ 0 \quad ; & \text{m even} \end{cases} \tag{3}$$

The constrained-current distribution is now as assumed in the previous section, Eqs. 4.8.4 and 4.8.10. The associated transfer relations relate the Fourier amplitudes of the tangential magnetic field intensities and vector potentials at the surfaces of the annular regions comprising the stator, the air gap and the rotor winding with designations (d) - (j) shown in Fig. 4.9.1.

Boundary Conditions: There are no surface currents in the model, so the tangential magnetic fields are continuous between regions and vanish on the stator and rotor magnetic materials. The normal flux density is continuous, and this requires that the vector potential be continuous:

$$\begin{aligned} &\tilde{H}_{\theta m}^d = 0; \ \tilde{H}_{\theta m}^e = \tilde{H}_{\theta m}^f; \ \tilde{H}_{\theta m}^g = \tilde{H}_{\theta m}^h; \ \tilde{H}_{\theta m}^i = 0 \\ &\tilde{A}_m^e = \tilde{A}_m^f; \ \tilde{A}_m^g = \tilde{A}_m^h \end{aligned} \tag{4}$$

Bulk Relations: The transfer relations, Eq. 4.8.12, are now applied in succession to the stator, the air gap and the rotor regions. In writing these expressions, the conditions of Eq. 4 are used to eliminate (e,h) variables in favor of the (f,g) variables:

$$\tilde{A}_m^d = \mu_o G_m(a,b)\tilde{H}^f{}_m + \mu_o \tilde{J}_m^s h_m(a,b)$$

$$\begin{bmatrix} -1. & \mu_o F_m(a,b) & 0 & 0 \\ -1 & \mu_o F_m(c,b) & 0 & \mu_o G_m(b,c) \\ 0 & \mu_o G_m(c,b) & -1 & \mu_o F_m(b,c) \\ 0 & 0 & -1 & \mu_o F_m(d,c) \end{bmatrix} \begin{bmatrix} \tilde{A}_m^f \\ \tilde{H}_{\theta m}^f \\ \tilde{A}_m^g \\ \tilde{H}_{\theta m}^g \end{bmatrix} = \begin{bmatrix} -\mu_o \tilde{J}_m^s h_m(b,a) \\ 0 \\ 0 \\ -\mu_o \tilde{J}_m^r h_m(c,d) \end{bmatrix} \tag{5}$$

$$\tilde{A}_m^i = \mu_o G_m(d,c)\tilde{H}_{\theta m}^g + \mu_o \tilde{J}_m^r h_m(d,c)$$

Because the boundary conditions on the magnetic materials uncouple them from the other relations, the first and last of these relations are written separately.

Torque as a Function of Terminal Variables: The torque is computed by integrating the Maxwell stress over the surface at (g) on the rotor side of the air gap (sec. 4.2). Because $B_r = (1/r)(\partial A/\partial\theta)$, the torque becomes (Eqs. 4.2.3 and 2.15.17):

$$\tau_z = 2\pi\ell c^2 \sum_{m=-\infty}^{+\infty} \left(\frac{-jm}{c} \tilde{A}_m^g\right)(\tilde{H}_{\theta m}^g)^* \tag{6}$$

To evaluate this expression, the amplitudes $\tilde{A}_m^g$ and $\tilde{H}_{\theta m}^g$ are found from the matrix equation of Eq. 5, using Cramer's rule:

$$\begin{aligned} \tilde{A}_m^g &= \tilde{J}_m^s C_1 + \tilde{J}_m^r C_2 \\ \tilde{H}_{\theta m}^g &= \tilde{J}_m^s C_3 + \tilde{J}_m^r C_4 \end{aligned} \tag{7}$$

where

$$C_1 = \frac{\mu_o^3}{D} h_m(b,a)G_m(c,b)F_m(d,c)$$

$$C_2 = \frac{\mu_o^3}{D} h_m(c,d)[F_m(a,b)F_m(b,c) - F_m(c,b)F_m(b,c) + G_m(c,b)G_m(b,c)]$$

$$C_3 = \frac{\mu_o^2}{D} h_m(b,a)G_m(c,b)$$

$$C_4 = \frac{\mu_o^2}{D} h_m(c,d)[F_m(a,b) - F_m(c,b)]$$

$$D = \mu_o^2\{G_m(c,b)G_m(b,c) - [F_m(c,b) - F_m(a,b)][F_m(b,c) - F_m(d,c)]\}$$

In using Eqs. 7 to evaluate Eq. 6, observe that $\tilde{J}_m^s(\tilde{J}_m^s)^*$ and $\tilde{J}^r(\tilde{J}_m^r)^*$ are even in m, as are also the functions h_m, F_m, and G_m. Because of the latter, the C_i's are also even in m. Thus, the summations of the self-field terms in $|\tilde{J}_m^s|^2$ and $|\tilde{J}_m^r|^2$ are odd functions of m and result in no contribution. The mth terms are canceled by the -mth terms. Only the cross terms appear, as Eq. 6 becomes

$$\tau_z = 2\pi\ell c \sum_{m=-\infty}^{+\infty} (-jm)[\tilde{J}_m^r(\tilde{J}_m^s)^* C_2C_3 + \tilde{J}_m^s(\tilde{J}_m^r)^* C_1C_4] \tag{8}$$

Substitution of Eqs. 2 and 3 therefore gives the torque as

$$\tau_z = \frac{16\ell c}{\pi} i_r n_r \sum_{\substack{m=1 \\ (\text{odd})}}^{\infty} \frac{(C_2C_3 - C_1C_4)}{m} \sin\left(\frac{m\theta_r}{2}\right) \sin\left(\frac{m\theta_s}{2}\right)[i_a n_a \sin m\theta_r + i_b n_b \sin m(\theta_r - \tfrac{\pi}{3}) + i_c n_c \sin m(\theta_r - \tfrac{2\pi}{3})] \tag{9}$$

where

$$(C_2C_3 - C_1C_4) = \frac{\mu_o^5}{D^2} h_m(c,d)h_m(b,a)G_m(c,b)[F_m(a,b)F_m(b,c) - F_m(c,b)F_m(b,c) + G_m(c,b)G_m(b,c) + F_m(d,c)F_m(c,b) - F_m(d,c)F_m(a,b)]$$

Electrical Terminal Relations: Each of the three phase windings of the stator, as well as the rotor winding, can be represented by the coil shown cross-sectionally in Fig. 4.9.4. For the "a" phase of the stator, variables are identified as $\theta_1 = \theta_s/2, \theta_2 = -\theta_s/2, \alpha = a, \beta = b$. For the rotor, $\theta_1 = \theta_r + \theta_f/2, \theta_2 = \theta_r - \theta_f/2, \alpha = c, \beta = d$.

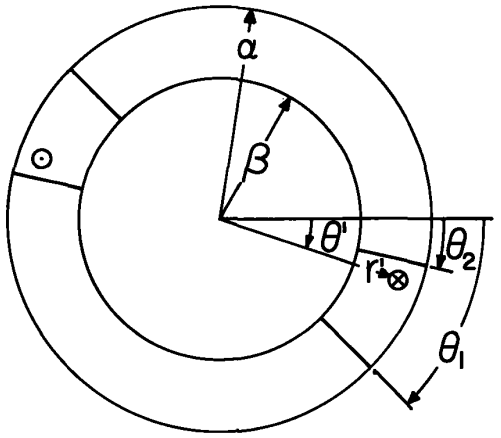

Fig. 4.9.4

Prototype coil representing each of the four in Fig. 4.9.1.

The flux linked by a single turn of the coil carrying current in the z direction at (r',θ') and returning it at $(r',\theta' + \pi)$ is conveniently evaluated in terms of the vector potential (Eq. (f) of Table 2.18.1):

$$\Phi_\lambda = \ell[A(r',\theta') - A(r',\theta' - \pi)] \tag{10}$$

With n defined as the turns per unit cross-sectional area, there are nr'dθ'dr' turns in a differential area and hence the total flux linked by the coil is

$$\lambda = \ell \int_{\beta}^{\alpha}\int_{\theta_2}^{\theta_1} \sum_{m=-\infty}^{+\infty} [\tilde{A}_m(r')e^{-jm\theta'} - \tilde{A}_m(r')e^{-jm(\theta'-\pi)}]nr'd\theta'dr' \tag{11}$$

The integration on θ' can be carried out directly to reduce Eq. 11 to

$$\lambda = 2j\ell n \sum_{\substack{m=-\infty \\ \text{odd}}}^{+\infty} \frac{\left(e^{-jm\theta_1} - e^{-jm\theta_2}\right)}{m} \int_{\beta}^{\alpha} \tilde{A}_m(r')r'dr' \tag{12}$$

To complete the radial integration, Eq. 4.8.13 is used to express $\tilde{A}_m$, while for the case being considered, $\tilde{A}_p$ is given by Eq. 4.8.11:

$$\lambda = 2j\ell n \sum_{\substack{m=-\infty \\ \text{odd}}}^{+\infty} \frac{\left(e^{-jm\theta_1} - e^{-jm\theta_2}\right)}{m} [\tilde{A}_m^{\alpha}M_m(\alpha,\beta) - \tilde{A}_m^{\beta}M_m(\beta,\alpha) - \mu_o\tilde{J}S_m(\alpha,\beta)] \tag{13}$$

where

$$M_m(x,y) = \frac{1}{2}[x^2 - m^2h_m(x,y)]$$

$$S_m(x,y) = \begin{cases} \dfrac{x^2}{m^2-4}M_m(x,y) - \dfrac{y^2}{m^2-4}M_m(y,x) - \dfrac{1}{4}\dfrac{(x^4 - y^4)}{m^2-4}, & m \neq \pm 2 \\ -\dfrac{1}{4}x^2 \ln xM_m(x,y) + \dfrac{1}{4}y^2 \ln yM_m(y,x) + \dfrac{1}{16}[x^4(\ln x - \frac{1}{4}) - y^4(\ln y - \frac{1}{4})], & m = \pm 2 \end{cases}$$

By appropriate identification of variables, Eq. 13 can now be used to compute the flux linked by each of the four electrical terminal pairs. The procedure is illustrated by considering the field winding. Then, variables are identified:

$$\lambda = \lambda_r,\ d \to c,\ \beta \to d,\ \theta_1 = \theta_r - \frac{\theta_f}{2},\ \theta_2 = \theta_r + \frac{\theta_f}{2},\ n = n_r,\ \tilde{A}^{\alpha} \to \tilde{A}^{g},\ \tilde{A}^{\beta} \to \tilde{A}^{i},\ \tilde{J} = \tilde{J}_m^r \tag{14}$$

The amplitudes $(\tilde{A}_m^g, \tilde{A}_m^i)$ are respectively evaluated from Eqs. 7a and the combination of Eqs. 5f and 7b. Thus, identified with the field winding, Eq. 13 becomes

$$\lambda_r = -\mu_o 4\ell n_r \sum_{\substack{m=-\infty \\ \text{odd}}}^{+\infty} \frac{1}{m} \sin\left(\frac{m\theta_f}{2}\right)e^{-jm\theta_r} \Big\{ \tilde{J}_m^s[C_1M_m(\alpha,\beta) - \mu_oG_m(d,c)C_3M_m(\beta,\alpha)]$$
$$+ \tilde{J}_m^r[C_2M_m(\alpha,\beta) - \mu_oG_m(d,c)C_4M_m(\beta,\alpha) + \mu_oM_m(\beta,\alpha)h_m(d,c) - \mu_oS_m(\alpha,\beta)] \Big\} \tag{15}$$

The current density amplitudes are in turn related to the terminal currents by Eqs. 2 and 3. Thus, Eq. 15 is expressed in terms of three mutual inductances and a self-inductance, in the form of Eq. 4.7.3d. In writing these inductances, observe that F_m and G_m are even functions of m. It follows that h_m and hence M_m and S_m are also even functions of m, and that finally the coefficients of $(\tilde{J}_m^s, \tilde{J}_m^r)$ in Eq. 15 are even in m. Thus, the summation can be converted to one on positive values of m:

$$\begin{bmatrix} L_{ra} \\ L_{rb} \\ L_{rc} \end{bmatrix} = -\frac{16\ell n_r}{\pi} \sum_{\substack{m=1 \\ \text{odd}}}^{\infty} \frac{\sin(\frac{m\theta_f}{2})}{m} \frac{\sin(\frac{m\theta_s}{2})}{m} [C_1M_m(\alpha,\beta) - \mu_oG_m(d,c)C_3M_m(\beta,\alpha)] \begin{bmatrix} n_a \cos m\,\theta_r \\ n_b \cos m(\theta_r + \frac{\pi}{3}) \\ n_c \cos m(\theta_r + \frac{2\pi}{3}) \end{bmatrix} \tag{16}$$

$$L_{rr} = -\frac{8\ell n_r^2}{\pi} \sum_{\substack{m=1 \\ \text{odd}}}^{\infty} \frac{\sin(\frac{m\theta_f}{2})}{m} \frac{\sin(\frac{m\theta_s}{2})}{m} [C_2 M_m(\alpha,\beta) - \mu_o G_m(d,c) C_4 M_m(\beta,\alpha) + \mu_o M_m(\beta,\alpha) h_m(d,c) - \mu_o S_m(\alpha,\beta)] \quad (17)$$

Because of the energy-conserving nature of the electromechanical coupling, there is redundancy of information in the electrical and mechanical terminal relations. Reciprocity, as expressed by Eq. 4.7.32b, can be made the basis for finding the θ_r dependent parts of the mutual inductances from the torque, Eq. 9. (Here, there are rotor positions at which each of the mutual inductances vanish, and hence Eq. 9 uniquely specifies the mutual inductances.) The reciprocity condition shows that an alternative to the coefficient used to express the mutual inductances in Eq. 16 is

$$[C_1 M_m(\alpha,\beta) - \mu_o G_m(d,c) C_3 M_m(\beta,\alpha)] = c[C_2 C_3 - C_1 C_4] \quad (18)$$

where the quantity on the right is given with Eq. 9.

With the reciprocity relations in view, one efficient approach to determining the complete lumped-parameter terminal relations is to first find the torque, Eq. 9, then use the reciprocity conditions to find the mutual inductances and finally compute the self-inductances from Eq. 13. This last step only requires evaluation of $(\tilde{A}_m^{\alpha},\tilde{A}_m^{\beta})$ with self-current excitations (with currents in other windings removed).

A more conventional approach is to compute the full inductance matrix from Eq. 13 and use the lumped-parameter energy method (Sec. 3.5) to find the torque.

4.10 D-C Magnetic Machines

The wide use of the d-c rotating machine justifies the model development undertaken in this section. But, these devices are also a prototype for a family of "conduction" machines which includes the homopolar generator[1] and magnetohydrodynamic energy convertors, to be taken up in Chap. 9. Analogous electric field devices are the Van de Graaff generator, considered in Sec. 4.14, and electrogas dynamic pumps and generators, described in Chaps. 5 and 9.

The developed model for the d-c machine given in Sec. 4.3 (Table 4.3.1, Part 3) is given a more complete characterization in Figs. 4.10.1 through 4.10.4. What is by convention termed the "field" winding is on the stator, which consists of a highly permeable structure wound with a total of $2n_f$ turns excited through the terminal pair (i_f,v_f). The "armature" is the rotor, with a winding connected through the commutator to the terminal pair (i_a,v_a), so that the distribution of current is essentially stationary in space. The θ dependence is shown in Fig. 4.10.2. The rotor core, like the stator magnetic circuit, is modeled here as being infinitely permeable.

With the assumption that the stator is infinitely permeable, it is clear that the magnetic potential on the stator surface, Ψ^f, is constant for those points at $r = R_o$ contiguous with the stator. Integration of Ampere's integral law, Eq. 2.7.1b, over any contour passing between the pole faces through the field winding and closing through the air gap shows that the pole faces differ in Ψ by $2n_f i_f$. The horizontal mid-plane is defined as the reference $\Psi = 0$. As an approximation that specifies the fringing field in the ranges of θ between pole faces, the magnetic potential is taken as the linear interpolation shown in Fig. 4.10.2a. Because the rotor is modeled as infinitely permeable, the tangential magnetic field at the rotor surface is equal to the surface current density K_z, as shown in Fig. 4.10.2b (an application of Eq. 2.10.21). The number of turns per unit azimuthal length on the rotor is N_a.

The commutator, which consists of conducting segments that are sequentially connected to the armature terminals through brushes, as shown in Fig. 4.10.3a,[2] is attached to one end of the rotor. Thus it rotates with the same angular velocity Ω (defined as positive in the positive θ direction) as the rotor. The model now developed does not include "end effects," in that the rotor is assumed to have a length ℓ that is much greater than the air gap R_o-R.

The boundary conditions, pictured graphically in Fig. 4.10.2, are first represented by Fourier series (Eqs. 2.15.7 and 2.15.8 with $k_n z \to n_\theta$ and $\ell \to 2\pi R$). Thus, with (f) denoting the radial position $r=R_o$,

$$\Psi^f = \sum_{\substack{m=-\infty \\ \text{(odd)}}}^{\infty} \tilde{\Psi}_m^f e^{-jm\theta}; \quad \tilde{\Psi}_m^f = \frac{2n_f i_f \sin m\theta_o}{m\pi(\theta_o m)} j e^{\frac{jm\pi}{2}} \quad (1)$$

---

1. H. H. Woodson and J. R. Melcher, Electromechanical Dynamics, Part I, John Wiley & Sons, New York, 1968, p. 312.

2. A. E. Fitzgerald, Ch. Kingsley, Jr., and A. Kusko, Electric Machinery, McGraw-Hill Book Company, New York, 1971, p. 192.

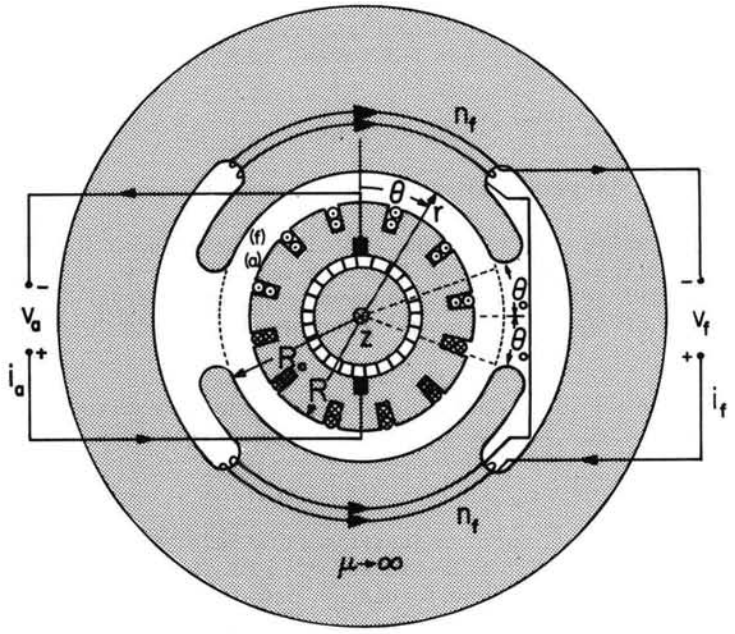

Fig. 4.10.1. Cross section of d-c machine.

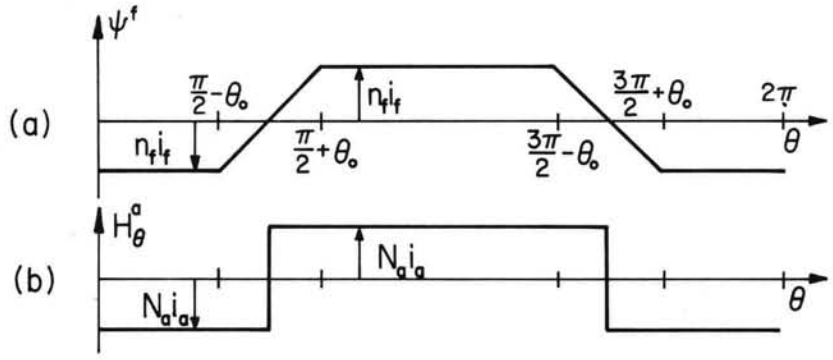

Fig. 4.10.2. Circumferential distribution of magnetic potential at $r = R_o$ and tangential magnetic field intensity at r = R.

and at the rotor surface where r = R,

$$H^a_\theta = \sum_{\substack{m=-\infty \\ (\text{odd})}}^{\infty} \tilde{H}^a_{\theta m} e^{-jm\theta}; \quad \tilde{H}^a_{\theta m} = \frac{2N_a i_a}{m\pi} j e^{\frac{jm\pi}{2}} \tag{2}$$

Fields in the air gap are represented by the transfer relations, Eqs. (a) of Table 2.16.2 with k = 0. Hence, with positions (α) → (f) and (β) → (a) and with radii α → R_o and β → R,

$$\begin{bmatrix} \tilde{B}^f_{rm} \\ \tilde{B}^a_{rm} \end{bmatrix} = \mu_o \begin{bmatrix} f_m(R,R_o) & g_m(R_o,R) \\ g_m(R,R_o) & f_m(R_o,R) \end{bmatrix} \begin{bmatrix} \tilde{\Psi}^f_m \\ R\tilde{H}^a_{\theta m}/jm \end{bmatrix} \tag{3}$$

where $\tilde{H}^a_{\theta m}$ has been introduced by using $H_\theta = -(\nabla\Psi)_\theta$.

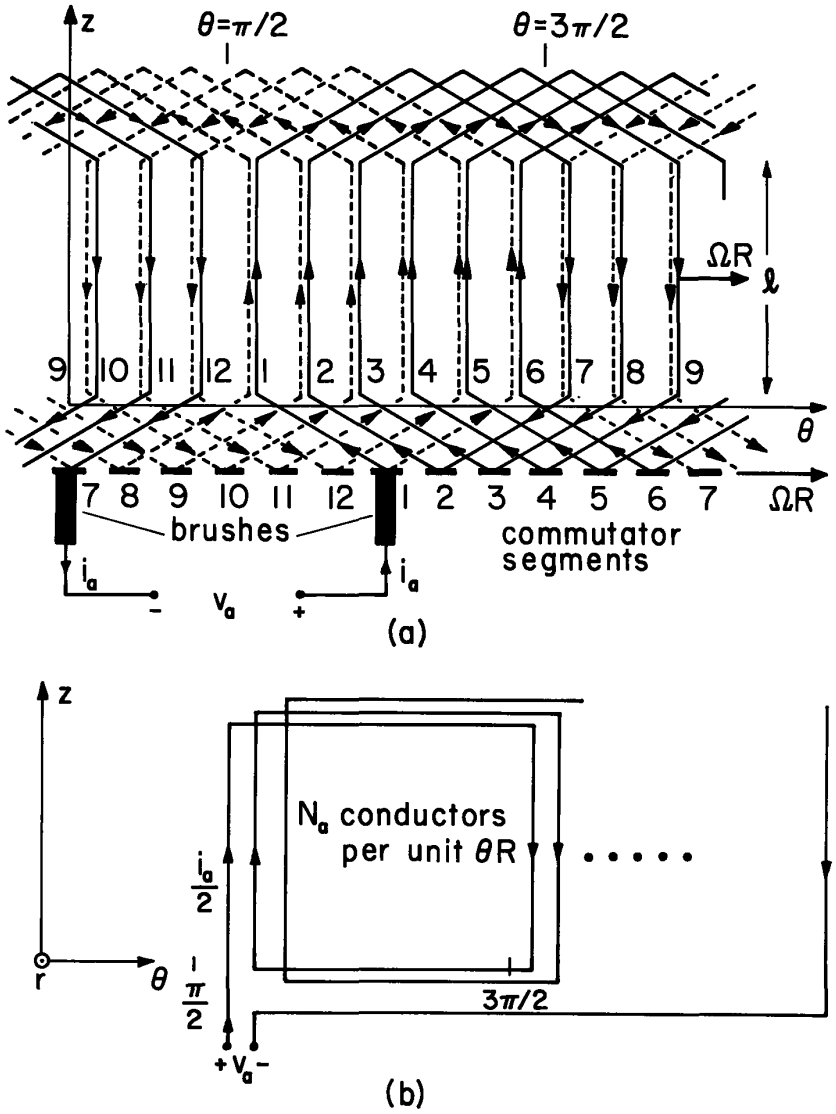

Fig. 4.10.3. (a) Typical winding scheme for armature of d-c machine shown in Fig. 4.10.1. The r axis is directed out of the paper. Brushes make contact with commutator segments which move to the right with armature conductors.[2] (b) Winding distribution of solid wires.

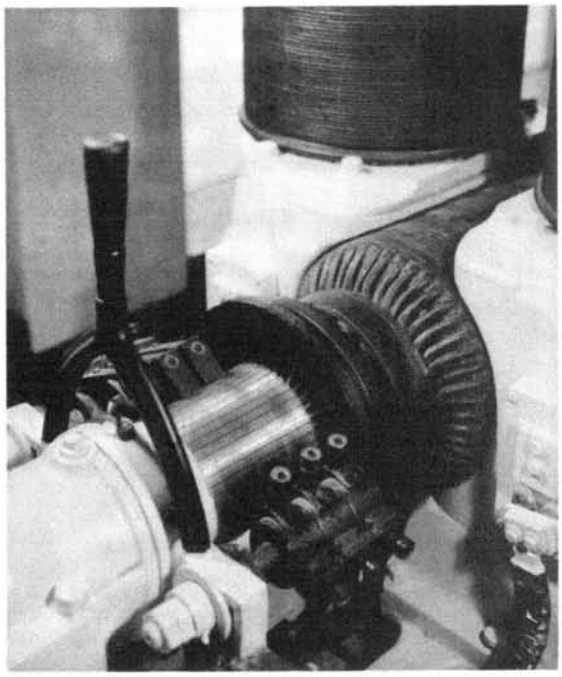

Fig. 4.10.4

This venerable d-c machine, of historical interest because it generated electric power for Boston at the turn of the century, has the advantage of putting the commutator segments and brushes in clear view. The pole faces surrounding the rotor at the upper right have a shape similar to that shown in Fig. 4.10.1, but the associated magnetic circuit is driven by armature coils wrapped on a horse-shoe magnetic circuit closing above the rotor. This is one of the first machines made after Thomas A. Edison moved from New York City to Schenectady in 1886.

Mechanical Equations: The rotor torque can be computed by integrating the Maxwell stress over a surface at $r = R_o$ just inside the stator. This is an application of Eq. 4.2.3:

$$\tau = (2\pi R_o \ell) R_o \left\langle B_r^f H_\theta^f \right\rangle_\theta \tag{4}$$

Because $\tilde{H}_{\theta m}^f = \tilde{\Psi}_m^f (jm/R_o)$, and in view of the averaging theorem (Eq. 2.15.17), substitution of Eqs. 1 and 2 converts Eq. 4 to

$$\tau = 2\pi R_o^2 \ell \sum_{m=-\infty}^{\infty} (\tilde{B}_{rm}^f)^* \left(\frac{jm}{R_o}\right) \tilde{\Psi}_m^f \tag{5}$$

With the substitution of Eq. 3a into Eq. 5, the "self-torque" (involving $\tilde{\Psi}_m^f (\tilde{\Psi}_m^f)^*$) sums to zero. (Because f_m/m is an odd function of m, the mth term in the sum cancels the -mth term.) The remaining expression is a sum on $\tilde{H}_{\theta m}^a \tilde{\Psi}_m^f$. These amplitudes are evaluated using Eqs. 1 and 2. The resulting magnetic torque is thus expressed as a function of the terminal currents:

$$\tau = -G_m i_f i_a ; G_m = \frac{16}{\pi} R R_o \ell \mu_o N_a n_f \sum_{\substack{m=1 \\ (\text{odd})}}^{+\infty} \frac{g_m(R_o, R)}{m^2} \frac{\sin(m\theta_o)}{m\theta_o} \tag{6}$$

The speed coefficient, G_m, is positive. This is consistent with the $(\vec{J} \times \vec{B})$ density expected with i_f and i_s positive, as shown in Fig. 4.10.1. But the use of the force density $\vec{J} \times \vec{B}$ misrepresents the actual distribution of force density on the rotor. With the conductors embedded in slots of highly permeable material, the flux lines actually tend to avoid the conductors and pass through the rotor surface between the slots. This means that the magnetic flux in the region where there is a current density tends to zero as the permeability becomes infinite. In fact, the magnetic torque is largely the result of the magnetization force density acting on the rotor magnetic material between the slots. Fortunately, the stress tensor used to find Eq. 6 includes the magnetization force density, so the deductions are sound. But, because the stress tensor is evaluated in free space, the same calculations would be carried out and the same answer obtained even if the essential role of the magnetization force density were not recognized. That the torque is not transmitted to the rotor through the conductor is important, because it alleviates problems encountered in maintaining insulation in the face of mechanical stress and vibration.

In terms of the electrical and mechanical terminal variables (i_f, i_a, τ_θ), Eq. 6 represents the

electrical-to-mechanical coupling.

Electrical Equations: To complete the model, it is necessary to express the mechanical-to-electrical coupling in terms of the terminal variables. This is done by taking advantage of Faraday's law, written for a contour of integration that is fixed in the laboratory frame of reference and passes through the appropriate winding:

$$\oint_C (\vec{E} - \vec{v} \times \mu_o \vec{M}) \cdot d\vec{\ell} = -\int_S \frac{\partial \vec{B}}{\partial t} \cdot \vec{n} da \tag{7}$$

For the armature, the circuit C is composed of whatever is externally connected to the terminals (v_a, i_a) and the armature windings. The brushes are idealized as making continuous contact with the moving conductors. A particular possible winding that would give the uniform distribution of rotor current density is shown in Fig. 4.10.3.

The fixed frame electric field integrated on the left in Eq. 7 is related to the conductor current density $\vec{J}$ by Ohm's Law, Eqs. 3.3.6, 2.5.11b, and 2.5.12b. Hence, $\vec{E} = \vec{J}/\sigma - \vec{v} \times \mu_o \vec{H}$ and

$$\vec{E} - \vec{v} \times \mu_o \vec{M} = \frac{\vec{J}}{\sigma} - \vec{v} \times \vec{B} \tag{8}$$

where $\vec{v} = \Omega R \vec{i}_\theta$ is the velocity of the moving conductors. At a given instant, the armature winding amounts to a superimposed parallel pair of windings connected through the brushes to the armature terminals. One of the pair is shown in Fig. 4.10.3b. The other coil, represented by the dotted wires of Fig. 4.10.3a, links the same flux. Each of these windings carries half of the armature current and has the turns density N_a.

For the "solid" windings, Eq. 7 becomes

$$-v_a + \int_{\text{wire}} \frac{\vec{J}}{\sigma} \cdot d\vec{\ell} + \int_{\text{wire}} \Omega R B_r \vec{i}_z \cdot d\vec{\ell} = -\frac{d}{dt} \int_S B_r da \tag{9}$$

where S is an integration over the surface enclosed by the contour C composed of the wire. The integration of $\vec{E}$ between the terminals external to the machine gives the term $-v_a$.

The current density in the wire is the net current $i_a/2$ divided by the cross-sectional area of the wire, A_a. Hence, the second term in Eq. 9 becomes

$$\int_{\text{wire}} \frac{\vec{J}}{\sigma} \cdot d\vec{\ell} = \frac{i_a}{2A_a} \frac{1}{\sigma_a} \ell_a = R_a i_a; \; R_a \equiv \frac{\ell_a}{2A_a \sigma_a} \tag{10}$$

where A_a is the cross-sectional area of the wire and ℓ_a is the total length of the wire joining the brushes at the given instant (the total length of the "solid" wire in Fig. 4.10.3a). Hence, R_a is the d-c resistance "seen" at the armature terminals.

The third term in Eq. 9 is evaluated by recognizing that those conductors between θ and $\theta + d\theta$ number $(N_a R)d\theta$, and therefore give a contribution $\Omega R B_r(\theta) N_a R d\theta$. This integrand makes a positive contribution in the interval $\pi/2 < \theta < 3\pi/2$, where the contour is in the positive z direction, and a negative contribution in the interval $-\pi/2 < \theta < \pi/2$ where the wires are returning in the -z direction:

$$\begin{aligned} \int_{\text{wire}} \Omega R B_r^a \vec{i}_z \cdot d\vec{\ell} &= \ell \int_{\pi/2}^{3\pi/2} \Omega R^2 N_a B_r^a d\theta - \ell \int_{-\pi/2}^{\pi/2} \Omega R^2 N_a B_r^a d\theta \\ &= -4\Omega \ell R^2 N_a \sum_{\substack{m=-\infty \\ (\text{odd})}}^{+\infty} \frac{\tilde{B}_{rm}^a}{m} j e^{-j\frac{m\pi}{2}} \end{aligned} \tag{11}$$

The second equality results from substitution of the Fourier series and carrying out the integration. It follows from substitution for B_{rm}^a using Eq. 3b with Eqs. 1 and 2 used to relate $\tilde{\psi}_m^f$ and $\tilde{H}_{\theta m}^a$ to the terminal currents that

$$\int_{\text{wire}} \Omega R B_r^a \vec{i}_z \cdot d\vec{\ell} = -\Omega G_m i_f \tag{12}$$

where G_m is the same as defined with Eq. 6. To complete these steps, observe that f_m/m^3 is an odd function of m, so that the contribution that is proportional to i_a sums to zero. Also, $Rg_m(R,R_o) = -R_o g_m(R_o,R)$, as can be seen from the definition in Table 2.16.2 or by application of the reciprocity condition, Eq. 2.17.10. There is no contribution to Eq. 12 of the part of B_r^a induced by the armature current because this "self-field" contribution to $\vec{v} \times \vec{B}$ at a winding location θ is cancelled by that at $-\theta$.

To evaluate the right-hand side of Eq. 9, first observe that the flux linked by the coils having their left edges in the range $d\theta'$ in the neighborhood of θ' is the product of the flux linked by one turn and the number of turns in that range of θ':

$$-\left[\ell\int_{\theta'}^{\theta'+\pi} B_r^a R d\theta\right] N_a R d\theta' \tag{13}$$

As a result, the total flux linked by all of the turns is

$$\int_S B_r da = -\int_{\pi/2}^{3\pi/2}\left[\ell\int_{\theta'}^{\theta'+\pi} B_r^a R d\theta\right] N_a R d\theta' \tag{14}$$

Again, substitution of the Fourier series for B_r^a and evaluation of the integrals gives

$$\int_S B_r da = 4\ell N_a R^2 \sum_{\substack{m=-\infty \\ (\text{odd})}}^{+\infty} \frac{\tilde{B}_{rm}^a}{m^2} e^{-j\frac{m\pi}{2}} \tag{15}$$

Further evaluation, using Eqs. 3b, 1 and 2, with the observation that g_m/m^3 is an odd function of m so that the contribution proportional to i_f vanishes, gives

$$\int_S B_r da = L_a i_a;\ L_a \equiv \frac{16\ell N_a^2 \mu_o R^3}{\pi} \sum_{\substack{m=1 \\ \text{odd}}}^{\infty} \frac{f_m(R_o,R)}{m^4} \tag{16}$$

That i_f makes no contribution to the net flux linked by the armature winding is evident from Fig. 4.10.1. The armature and field magnetic axes are perpendicular. Thus, with the substitution of Eqs. 10, 12 and 16, the armature circuit equation, Eq. 9, becomes

$$v_a = R_a i_a - \Omega G_m i_f + L_a \frac{di_a}{dt} \tag{17}$$

where R_a, G_m and L_a are given by Eqs. 10, 6 and 16.

The circuit equation for the field winding is similarly found by applying Faraday's integral law, Eq. 7, to a contour composed of the field winding. The right-hand side of Eq. 7 is approximated by the flux contribution over the surfaces of the respective poles:

$$\int_S B_r da = n_f \ell \int_{-\frac{\pi}{2}+\theta_o}^{\frac{\pi}{2}-\theta_o} B_r^f R_o d\theta - n_f \ell \int_{\frac{\pi}{2}+\theta_o}^{\frac{3\pi}{2}-\theta_o} B_r^f R_o d\theta \tag{18}$$

Substitution of the Fourier series for B_r^f and integration gives

$$\int_S B_r^f da = 4 n_f \ell R_o \sum_{\substack{m=1 \\ (\text{odd})}}^{\infty} \frac{e^{-j\frac{m\pi}{2}}}{(-jm)} \tilde{B}_r^f \cos m\theta_o \tag{19}$$

This expression can now be evaluated using first Eq. 3a and then Eqs. 1 and 2. Because g_m/m^3 is an odd function of m, the term proportional to i_a sums to zero with the result

$$\int_S B_r^f da = L_f i_f;\ L_f \equiv -\frac{16 n_f^2 \ell R_o \mu_o}{\pi} \sum_{\substack{m=1 \\ (\text{odd})}}^{\infty} \frac{\cos m\theta_o}{m^2} \frac{\sin m\theta_o}{m\theta_o} f_m(R,R_o) \tag{20}$$

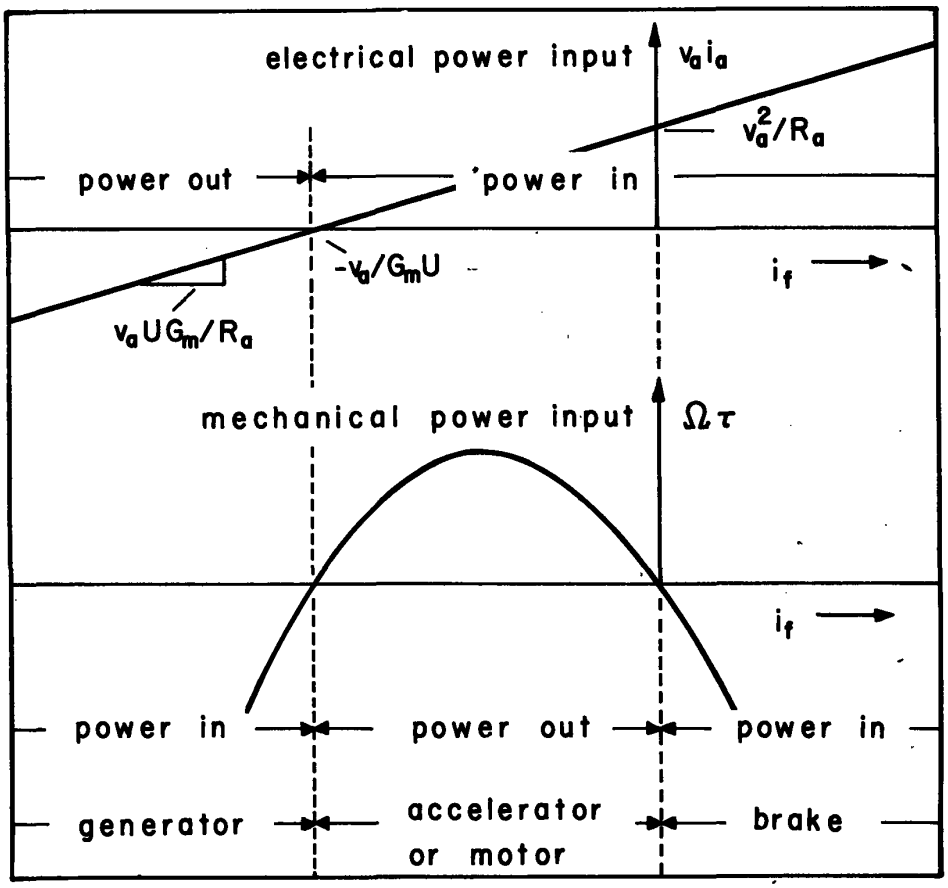

Fig. 4.10.5. Regimes of energy conversion for a d-c magnetic field type interaction. Armature voltage v_a is fixed and field current i_f is varied. With the identification of variables $i_f \to v_f$, $v_a \to i_a$, $R_a \to R_a^{-1}$, $G_m \to G_e$, the power characteristics also represent the Van de Graaff type of device developed in Sec. 4.14.

Note from the definition of f_m in Table 2.16.2 or the energy relation, Eq. 2.17.12, that $f_m(R,R_o) < 0$, so that L_f is positive. The left-hand side of Eq. 7 is evaluated as for the armature except that the conductor is fixed. Hence, Eq. 7 becomes the required circuit equation for the field:

$$v_f = R_f i_f + L_f \frac{di_f}{df} \tag{21}$$

The total resistance of the field winding is $R_f = A_f \ell_f/\sigma_f$, and L_f is given by Eq. 20.

The Energy Conversion Process: Simple consideration of Eqs. 6 and 17 relates the discrete electrical and mechanical terminal variables to the energy conversion process. Consider the field excitation current i_f and the armature voltage v_a as constrained by external sources. The steady-state dependence of the armature current and the magnetic torque on the constrained variables implied by Eqs. 6 and 17 is then

$$i_a = \frac{v_a}{R_a} + \frac{\Omega G_m}{R_a} i_f \tag{22}$$

$$\tau = - G_m i_f \left[\frac{v_a}{R_a} + \frac{\Omega G_m}{R_a} i_f\right] \tag{23}$$

The electrical power input to the device follows from Eq. 22 as

$$i_a v_a = \frac{v_a}{R_a} [v_a + \Omega G_m i_f] \tag{24}$$

while the mechanical power output is given by Eq. 23 multiplied by the angular velocity

$$\Omega\tau = -\frac{\Omega G_m}{R_a} i_f[v_a + G_m i_f] \tag{25}$$

These last two expressions are sketched in Fig. 4.10.5 to show the power-flow dependence on the field current i_f with Ω assumed positive.

In view of the physical significance of $i_a v_a$ and $\Omega\tau$, it is possible to classify the regimes of operation as also sketched in Fig. 4.10.5. It is because the electromechanical coupling has been defined to include the electrical losses (by contrast with the point of view in Sec. 4.9, for example) that the brake regime is possible.

The power conversion characteristics exemplified by this d-c machine and summarized in Fig. 4.10.5 are in common to the family of d-c or conduction type interactions. For example, with appropriate redefinition of variables, the same characteristics pertain to the Van de Graaff machine of Sec. 4.14.

4.11 Green's Function Representations

In dealing with fields that are related to sources (the charge density or current density) through linear differential equations, it is possible to use yet another approach that is based on the fact that superposition of sources implies superposition of fields. This approach, which is an alternative applicable to situations illustrated in Secs. 4.5 - 4.9, is familiar from the use of the superposition integral to find the potential response from charge specified throughout all space or from the Biot-Savart law for finding the magnetic field, given the distribution of current density throughout space.

Volume source distributions can often be considered the sum of distributions of surface charge or surface current. The transfer relations are a convenient vehicle for obtaining the response to such singular sources. By then integrating over the actual given source distribution, the field is represented as the sum of field responses to the surface sources.

The determination of the fields and force associated with the charge beam of Sec. 4.6 illustrates the method. Figure 4.11.1 shows a cross section of the configuration pictured in Fig. 4.6.1, but with the only volume charge in a shell having radial thickness dr' at the radius r', where the density is $\rho(r')$. The fields due to an arbitrary radial distribution of charge can be constructed once the response to this surface charge, having density $\tilde{\rho}(r')dr'$, is determined. At the outset, consider the field to be a superposition of fields due to the potential $\tilde{V}_o$ imposed at the surface r = a and to the distribution of charge in the volume. The latter is determined by using the boundary conditions

$$\tilde{\Phi}^c = 0,\ \tilde{\Phi}^d = \tilde{\Phi}^e,\ \tilde{D}_r^d - \tilde{D}_r^e = \tilde{\rho}(r')dr' \tag{1}$$

Implicit is the understanding that there is no θ dependence, and that the z dependence is exp(-jkz).

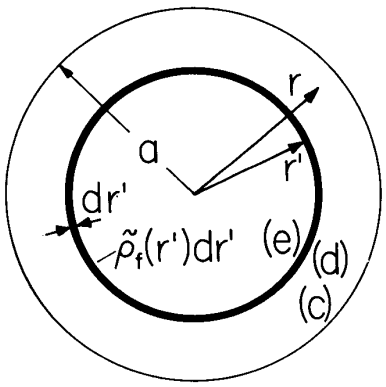

Fig. 4.11.1

Shell having surface-charge density $\tilde{\rho}_f(r')dr'$ gives rise to fields that can be summed to determine field due to arbitrary charge distribution.

In the region r > r', the flux-potential relations, Eq. (a) of Table 2.16.2, apply:

$$\begin{bmatrix} \tilde{D}_r^c \\ \tilde{D}_r^d \end{bmatrix} = \varepsilon \begin{bmatrix} f_o(r',a) & g_o(a,r') \\ g_o(r',a) & f_o(a,r') \end{bmatrix} \begin{bmatrix} \tilde{\Phi}^c \\ \tilde{\Phi}^d \end{bmatrix} \tag{2}$$

whereas in the inner region, r < r', the limiting form of Eq. (c) is appropriate:

$$\tilde{D}_r^e = \varepsilon f_o(0,r')\tilde{\Phi}^e \tag{3}$$

Subtraction of Eq. 3 from Eq. 2b and use of the boundary conditions of Eq. 1 gives

$$\tilde{\Phi}^d = \tilde{\Phi}^e = \frac{\tilde{\rho}(r')dr'}{\varepsilon[f_o(a,r') - f_o(0,r']} \tag{4}$$

By the judicious use of these amplitudes and the potential distribution given for a canonical annular region by Eq. 2.16.25, it is now possible to write the radial distribution of $\tilde{\Phi}$ for an arbitrary distribution of charge density. There are three terms. The first is simply the potential due to the voltage $\tilde{V}_o$ applied at the outer wall. For this part, Eq. 2.16.25 is evaluated with $\beta \to 0$ and $\tilde{\Phi}^\alpha = \tilde{V}_o$. The second term comes from evaluating Eq. 2.16.25 for the potential at r due to the charge shell at $r' < r$ (so that $\alpha = a$, $\beta = r'$, $\tilde{\Phi}^\alpha = \tilde{\Phi}^c = 0$ and $\tilde{\Phi}^\beta = \tilde{\Phi}^d$) and adding up all contributions attributable to charge inside the radius of observation r. Finally, the third term is written by again using Eq. 2.16.25 to express the potential, but this time due to charge at a greater radius than the r, at $r < r'$ (so that $\alpha = r'$, $\beta \to 0$ and $\tilde{\Phi}^\alpha = \tilde{\Phi}^d$) and integrating over the distribution outside the observation position r:

$$\tilde{\Phi}(r) = \tilde{V}_o \frac{J_o(jkr)}{J_o(jka)} + \int_o^r \frac{[J_o(jka)H_o(jkr) - H_o(jka)J_o(jkr)]}{[J_o(jka)H_o(jkr')-H_o(jka)J_o(jkr')]} \frac{\tilde{\rho}(r')dr'}{\varepsilon[f_o(a,r') - f_o(0,r')]}$$

$$+ \int_r^a \frac{J_o(jkr)}{J_o(jkr')} \frac{\tilde{\rho}(r')dr'}{\varepsilon[f_o(a,r') - f_o(0,r')]} \tag{5}$$

To find the axial force acting on the entire beam, it is only the normal flux density at the outer wall that is required. This can be found from Eq. 5, but is more easily determined directly from Eqs. 2a, used first with $\tilde{\Phi}^c = \tilde{V}_o$ and (d) $\to 0$ to find the flux density due to the wall potential alone and then with $\tilde{\Phi}^c = 0$ and $\tilde{\Phi}^d$ given by Eq. 4 to find the part due to the volume charge. The latter is summed over the total distribution of charge.

$$\tilde{D}_r^c = \varepsilon f_o(0,a)\tilde{V}_o + \int_o^a \frac{g_o(a,r')\tilde{\rho}(r')dr'}{[f_o(a,r') - f_o(0,r')]} \tag{6}$$

The force is thus determined by substituting this expression into Eq. 4.6.3. Equation 6 holds for an arbitrary charge distribution, but consider the uniform distribution of charge inside the radius R. Then the integration needs only be carried out from 0 to R. With $\tilde{V}_o$ and $\tilde{\rho}(r')$ selected consistent with Eqs. 4.6.1 and 4.6.2, it follows that the force is given by Eq. 4.6.8 with L_1 replaced by L_3, where

$$L_3 = \frac{a}{R^3}\int_o^R \frac{g_o(a,r')dr'}{[f_o(a,r') - f_o(0,r')]} = \frac{1}{(kR)^2}\int_o^{kR} (kr') \frac{I_o(kr')}{I_o(ka)}\, d(kr') \tag{7}$$

The integral is carried out by recognizing that $I_o(kr')$ is a solution to Eq. 2.16.19 with $r \to r'$ and $m = 0$:

$$\frac{d}{dr'}\left(r' \frac{dI_o(kr')}{dr'}\right) = k^2 r I_o(kr') \tag{8}$$

Hence, Eq. 7 gives the same result, Eq. 4.6.13, as found in Sec. 4.6 using the "splicing approach."

The same procedure applies if the charge has θ dependence $\exp(-jm\theta)$. Thus, by making use of a Fourier series representation in θ and z, the method can be used to describe fields associated with arbitrary dependence on θ and z.

The Green's function approach exemplified here is applicable to modeling the synchronous machines developed in Secs. 4.7 and 4.8.[1]

4.12 Quasi-One-Dimensional Models and the Space-Rate Expansion

The "narrow-air-gap" model for rotating machines and long-wave models for electromagnetic wave propagation are examples of quasi-one-dimensional models. The following sections illustrate the use of such models in the kinematic description of electromechanical interactions. Extensive use will be made in later chapters of models that similarly exploit a relatively slow variation of distributed quantities in a "longitudinal" direction relative to "transverse" directions.

---

1. This is the method used by Kirtley in "Design and Construction of an Armature for an Alternator with a Superconducting Field Winding," Ph.D. Thesis, Department of Electrical Engineering, MIT, Cambridge, Mass., 1971, for a configuration closely resembling that considered in Sec. 4.8.

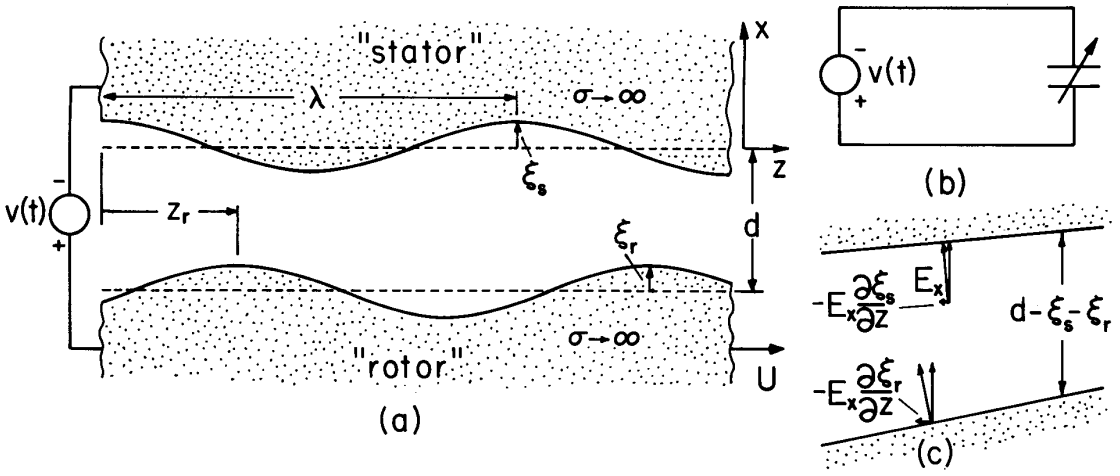

Fig. 4.12.1. (a) Cross-sectional view of synchronous electric field energy converter with stator and rotor composed of perfectly conducting materials constrained by a time-varying voltage source. The stator geometry is static, while the rotor moves to the right. (b) Interaction represented by time-varying capacitance. (c) Detail of air gap showing components of E_z to satisfy boundary conditions.

An example is shown in Fig. 4.12.1. Perfectly conducting surfaces having the potential difference v(t), vary from the planes x = 0 and x = -d by the amounts $\xi_s(z,t)$ and $\xi_r(z,t)$, respectively. What are the fields in the gap? This configuration is the basis for the study of the variable-capacitance machine in Sec. 4.13. Fields in the gap can be approximated by two techniques. If ξ_s and ξ_r are small compared to d, the boundary conditions can be linearized, and the fields found approximately. This is the approach used in Sec. 4.3 for describing the salient pole interactions (Eq. 4.3.16). It formally amounts to expanding the fields in an amplitude parameter expansion with the zero-order fields those with ξ_s and ξ_r equal to zero, the first-order terms those given by keeping only linear terms in (ξ_s,ξ_r) and so on. Thus, the validity of the model hinges on the amplitudes (ξ_s,ξ_r) being small.

In quasi-one-dimensional models, amplitudes are not necessarily small. Rather, certain spatial rates of change are small. In the configuration of Fig. 4.12.1, the distance λ typifying variations in the z direction is long compared to the distance d, $\gamma \equiv (d/\lambda)^2 << 1$.

The relationship between linearized and quasi-one-dimensional models is illustrated in Fig. 4.12.2. Linearized quasi-one-dimensional models must be consistent with the long-wave limit of the linearized model. In establishing complex models, this fact is often used to motivate the appropriate "zero-order" approximation which is the starting point in developing a quasi-one-dimensional model.

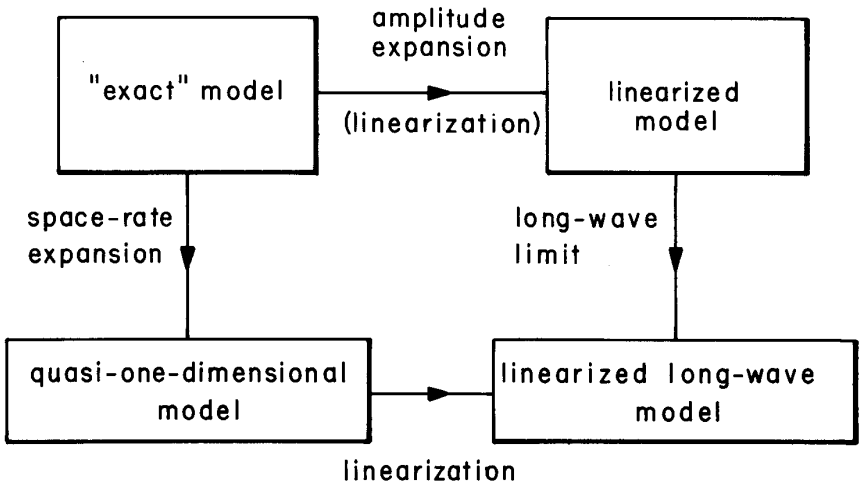

Fig. 4.12.2. Schematic characterization of relationships among three-dimensional, quasi-one-dimensional and linearized models.

Usually, quasi-one-dimensional models are motivated by physical reasoning, with little need for formality. This is partly because higher order terms are seldom used. But, at least once, it is worhwhile to see how higher order terms are found, and that the approximation used is the lowest order term in an expansion in powers of a space-rate parameter, in the example of Fig. 4.12.1, of $\gamma = (d/\lambda)^2$.

The procedure here is analogous to that of Sec. 2.3 on quasistatics. The spatial coordinate z, in which variables evolve slowly, plays the role of time. The physical idea that this slow variation ought to make one field component dominate the other is built into the normalization of variables. If modulations of the electrodes are slowly varying compared to the transverse distance d, each section of the electrodes tends to form a parallel-plate capacitor. With E_o a typical electric field in the x direction (the "dominant" field component), d taken as the typical length in the x direction, but λ as that length in the z direction, the appropriate normalization is

$$\begin{aligned} E_x &= E_o \underline{E}_x & x &= d\underline{x} \\ E_z &= E_o(d/\lambda)\underline{E}_z & z &= \lambda \underline{z} \\ \xi_r &= d\underline{\xi}_r,\ \xi_s = d\underline{\xi}_s & v &= (E_o d)\underline{v} \end{aligned} \tag{1}$$

In the gap, $\vec{E}$ is irrotational and solenoidal. In terms of the normalized variables, these conditions are

$$\begin{aligned} &\frac{\partial E_x}{\partial z} - \frac{\partial E_z}{\partial x} = 0 \\ &\frac{\partial E_x}{\partial x} = -\gamma \frac{\partial E_z}{\partial z} \end{aligned} \tag{2}$$

where the space-rate parameter $\gamma \equiv (d/\lambda)^2$. To complete the formulation in terms of normalized variables, boundary conditions at the scalloped perfect conductors are that the potential difference be v(t) and the tangential fields vanish:

$$E_z = -\frac{\partial \xi_s}{\partial z} E_x(x = \xi_s);\ E_z = -\frac{\partial \xi}{\partial z} E_x(x = \xi_r - 1);\ \int_{\xi_r - 1}^{\xi_s} E_x dx = v \tag{3}$$

Only two of these three expressions are independent.

The normalized field components are now expanded in series of the form

$$\begin{aligned} E_x &= E_{xo} + \gamma E_{x1} + \gamma^2 E_{x2} + \cdots \\ E_z &= E_{zo} + \gamma E_{z1} + \gamma^2 E_{z2} + \cdots \end{aligned} \tag{4}$$

Note that only one dimensionless parameter is involved, so for the particularly simple case at hand, there is no ambiguity as to what lengths are most critical.

Substitution of the series of Eq. 4 into Eqs. 2 gives a pair of expressions which are polynomial in γ. Coefficients of each order in γ must vanish; thus, the zero-order terms involve only the zero-order fields

$$\begin{aligned} &\frac{\partial E_{xo}}{\partial z} - \frac{\partial E_{zo}}{\partial x} = 0 \\ &\frac{\partial E_{xo}}{\partial x} = 0 \end{aligned} \tag{5}$$

but the first order expressions are "driven" by the zero order fields

$$\begin{aligned} &\frac{\partial E_{x1}}{\partial z} - \frac{\partial E_{z1}}{\partial x} = 0 \\ &\frac{\partial E_{x1}}{\partial x} = -\frac{\partial E_{zo}}{\partial z} \end{aligned} \tag{6}$$

It follows from Eqs. 3c and 5b that E_{xo} is quasi-one-dimensional. It only depends on (z,t):

$$E_{xo} = E_{xo}(z,t) = \frac{v}{\xi_s + 1 - \xi_r} \tag{7}$$

What has been deduced as the zero-order E_x is just the voltage divided by the distance between conductors. If variations with z are sufficiently slow, each section of the system forms a plane-parallel capacitor. To find the other component of the zero-order field, note that E_{xo} is only a function of (z,t), so Eq. 5a can be integrated to obtain

$$E_{zo} = x \frac{\partial E_{xo}}{\partial z} + f(z,t) \tag{8}$$

where f(z,t) is an integration function. This function is determined by substitution of Eq. 8 into Eq. 3a:

$$E_{zo} = x \frac{\partial E_{xo}}{\partial z} - \frac{\partial}{\partial z}(E_{xo}\xi_s) \tag{9}$$

Substitution now shows that the tangential field on the lower surface is zero, Eq. 3b is satisfied. The zero-order fields are represented in dimensionless form by Eqs. 7 and 9.

The first-order fields are predicted by Eqs. 6, now that the zero-order fields are known. From Eqs. 6b and 9,

$$-\frac{\partial E_{x1}}{\partial x} = -\frac{\partial E_{zo}}{\partial z} = -x \frac{\partial^2 E_{xo}}{\partial z^2} + \frac{\partial^2}{\partial z^2}(E_{xo}\xi_s) \tag{10}$$

The functional dependence on x on the right in this expression is explicit, and therefore integration gives

$$E_{x1} = -\frac{x^2}{2} \frac{\partial^2 E_{xo}}{\partial z^2} - x \frac{\partial^2}{\partial z^2}(E_{xo}\xi_s) + g(z,t) \tag{11}$$

Because the zero-order E_x already satisfies the boundary condition, E_{xo} integrates to v across the gap (Eq.3c), the same integral of Eq. 11 must vanish and that serves to determine the integration function g(z,t). At this point, two terms in the series of Eq. 4a have been found, and they are sufficient to show what is meant by the expansion

$$E_x = \frac{v}{(1 + \xi_s - \xi_r)} + \gamma \left\{ \frac{\partial^2 E_{xo}}{\partial z} \left[-\frac{x^2}{2} + \frac{1}{6} \frac{\xi_s^3 + (1 - \xi_r)^3}{\xi_s + (1 - \xi_r)} \right] + \frac{\partial^2}{\partial z^2}(E_{xo}\xi_s)\left(x - \frac{1}{2}[\xi_s - (1 - \xi_r)]\right) \right\} \tag{12}$$

By the definition of ℓ used in normalizing z, $\partial^2 E_{xo}/\partial z^2$ is on the order of E_{xo}. Hence, the first term in Eq. 12 gives an accurate picture of the field, provided $\gamma << 1$.

The procedure outlined is mainly of conceptual value. Certainly the quasi-one-dimensional modeling of a complex problem begins with a physically motivated approximation: here, Eq. 7. Because no more than the zero-order solutions are usually required, the formalism of normalizing the variables and identifying dimensionless space parameters is not usually required.

In retrospect, the zero-order fields have a dependence on the transverse direction (x) that is the lowest order polynomial in x consistent with the boundary conditions. Thus, E_{xo} varies as x^o (it is independent of x); while E_{zo} can satisfy the boundary conditions only if it includes a linear dependence on x.

4.13 Variable-Capacitance Machines

A model for one of the most commonly discussed "electrostatic" synchronous machines (which are themselves rather uncommon) is shown in Fig. 4.12.1a. Both the fixed and moving members have saliency and consist essentially of perfectly conducting material. The time-varying voltage between stator and rotor can either be the source of electrical power for producing a synchronous force in the z direction on the rotor, or it can serve as the voltage of a bus representing an energy sink for the device acting

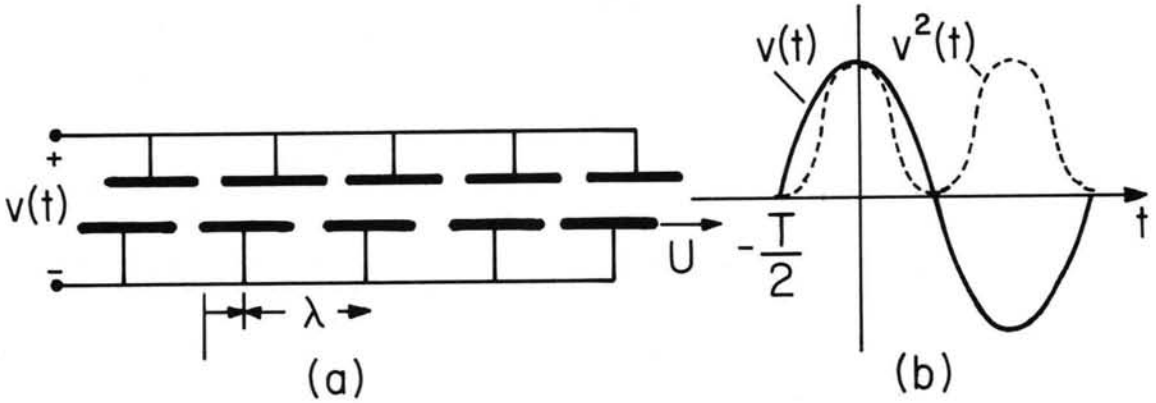

Fig. 4.13.1. Physical realization of variable-capacitance machine modeled in Fig. 4.12.1. (a) Stator and rotor structure consisting of vanes. (b) Sinusoidal voltage supplied through slip rings together with $v^2(t)$, showing temporal dependence of instantaneous force.

Image removed due to copyright restrictions.
Photograph of a variable-capacitance generator designed for use with vacuum insulation.

Fig. 4.13.1c. Variable-capacitance generator designed for use with vacuum insulation. Estimated output at 30,000 rpm is 6 kW at 20 kV (courtesy Goodrich High Voltage Corp.). Development of variable-capacitance machines was attempted for the generation of high-voltage power with application to ion propulsion in the space program. In space, vacuum insulation is easily obtained. See reports for Contract No. AF33(616)-7230 from Goodrich-High Voltage Astronautics, Inc., Burlington, Mass., to Aeronautical Systems Division, Air Force Systems Command, U.S. Air Force, Wright-Patterson Air Force Base, Ohio. For example, Phase II report by A. S. Denholm et al., 1961.

as a generator. In practice, the stator and rotor members might consist of metallic fins, as shown in Fig. 4.13.1. In the model, regions on the stator and rotor that project into the air gap represent the fins, while regions that dip into the stator and rotor material represent the gaps between fins.

The device is often referred to as a "variable-capacitance" machine because, when the relative position of rotor and stator is such that the projections into the gap are just opposite each other, the capacitance is at a maximum, while it reaches a minimum when the peak in rotor saliency falls just opposite a "valley" in the stator material.

One way to view the energy conversion process is simply to represent the capacitance seen by the voltage source as time-varying. Given the motion of the rotor, the capacitance C is a known function of time, and the electrical problem comes down to determining a suitable temporal variation for C, relative to a time-varying voltage, v. If power is supplied to the voltage source, it must come from the mechanical forces responsible for making the capacitance vary with time. Thus, the other side of the energy conversion process raises the question: How is a time-average force produced on the rotor by the combination of the salient configuration and the time-varying applied voltage? In this section, we will take up the second question first. What is the electrical force in the direction of motion on the moving member?

The field point of view taken here results in the relation between geometry and capacitance needed to model an actual system, even if the circuit point of view is taken. But also, it makes the example useful in conceptualizing electromechanical interactions that cannot be given a lumped-parameter model. For example, suppose that the undulations on the "rotor" were in fact material deformations produced by the field itself. This type of self-consistent electromechanical coupling is not kinematic and will be taken up in Chap. 9.

Synchronous Condition: With a sinusoidal voltage v(t) having period T, applied between the rotor and stator by means of a slip-ring, a time-average electrical force can act in the z direction on the rotor only if there is a synchronism between the applied voltage and the rotor motion. To this end, consider the physical origins of this force in terms of the model shown in Fig. 4.12.1. Regardless of the field polarity, at any position on the rotor surface there is an electric force per unit area that is directed perpendicular to the surface and into the air gap. This latter fact makes it clear that without the surface undulations, there can be no electrical force in the z direction.

To make a synchronous motor, on the time average, fields acting to the right over regions of the rotor surface with a negative slope must produce a greater force than those acting to the left on the regions where the slope is positive. What is the relationship between the excitation period T and the rotor velocity U that could result in there being a time-average electrical force? In terms of the displacement z_r of Fig. 4.12.1, a maximum in the force to the right is obtained with z_r in the neighborhood of $\lambda/4$. Thus, with the rotor in this position, the applied v^2 should be at its maximum. By the time the rotor is at $z_r = 3\lambda/4$, the force produced is in the wrong direction, and hence v^2 should be near a null. By the time $z_r = 5\lambda/4$, v^2 should be peaking again. It is concluded that in the time T/2, the rotor should move one wavelength: $UT/2 = \lambda$. Thus, the synchronism condition is met if

$$z_r = Ut + \delta;\ U = \frac{2\lambda}{T} \tag{1}$$

Here, δ is a spatial phase-angle determined by the mechanical load on a motor or the electrical load on a generator.

The quasi-one-dimensional electric field is given by Eqs. 4.12.7 and 4.12.9 un-normalized:

$$E_x = \frac{v}{d + \xi_s - \xi_r};\ E_z = (x + d)\frac{\partial E_x}{\partial z} - \frac{\partial}{\partial z}(\xi_r E_x) \tag{2}$$

The force on a section of the rotor one wavelength long and a length ℓ in the y direction is found by integrating the Maxwell stress tensor over an enclosing surface as pictured in Fig. 4.2.1a. The only surface giving a contribution is the one of constant x in the air gap:

$$f_z = \ell \int_z^{z+\lambda} \varepsilon_o E_x E_z dz \tag{3}$$

This integral can be evaluated using the fields of Eq. 2. That it does not matter what x = constant plane is used in carrying out the integration (except for physical reasons, to have the assurance that the surface does not cut through one of the electrode inward peaks) is evident from the fact that

$$\int_z^{z+\lambda} \varepsilon_o E_x(x+d) \frac{\partial E_x}{\partial z}\, dz = \varepsilon_o(x+d)\int_z^{z+\lambda} \frac{\partial}{\partial z}\left(\frac{1}{2} E_x^2\right)dz = \varepsilon_o(x+d)[E_x^2(z+\lambda) - E_x^2(z)] = 0 \qquad (4)$$

The final deduction follows from the spatial periodicity of the structure. The remaining contributions to the integral are expressed using the normalization

$$z = \lambda \underline{z},\ \xi_s = d\underline{\xi}_s,\ \xi_r = d\underline{\xi}_r,\ \delta = \lambda\underline{\delta},\ z_r = \lambda \underline{z}_r \qquad (5)$$

With $f_z \equiv (\varepsilon_o \ell v^2/d)\underline{f}_z$, Eq. 3 becomes

$$f_z = -\int_z^{z+1} \frac{1}{1 + \xi_s - \xi_r} \frac{\partial}{\partial z}\left[\frac{\xi_r}{1 + \xi_s - \xi_r}\right]dz \qquad (6)$$

Carrying out the differentiation in the integrand gives

$$f(z_r) \equiv -\int_z^{z+1} \frac{(1 + \xi_s)\frac{\partial \xi_r}{\partial z} - \xi_r \frac{\partial \xi_s}{\partial z}}{(1 + \xi_s - \xi_r)^3}\, dz \qquad (7)$$

Once the integral is completed, the function f depends on the amplitudes of ξ_s and ξ_r and on their relative displacement z_r. The time-average force is then computed by specifying this relative displacement in terms of Eq. 1. In normalized variables, with $t = T\underline{t}$

$$\left\langle f_z \right\rangle_t = \frac{\varepsilon_o \ell}{d}\int_{\underline{t}}^{\underline{t}+1} v^2(\underline{t})\underline{f}(2\underline{t} + \underline{\delta})d\underline{t} \qquad (8)$$

As an example, consider stator and rotor electrodes having sinusoidal shapes of equal amplitude and a sinusoidal excitation voltage (note that Eqs. 7 and 8 are general in regard to these specifications):

$$\underline{\xi}_s = \underline{\xi}_o \cos 2\pi \underline{z},\ \underline{\xi}_r = \underline{\xi}_o \cos 2\pi(\underline{z} - \underline{z}_r),\ v(t) = V \cos 2\pi \underline{t} \qquad (9)$$

Numerical integration of Eq. 7 then gives the dependence on relative displacement and amplitude shown in Fig. 4.13.2a. To highlight the nonlinear effects of ξ_o, f is normalized to ξ_o^2 so that much of the dependence on the electrode amplitudes is suppressed.

The electrodes make their closest approach to each other with $\underline{z}_r = 0.5$ and are furthest apart when $\underline{z}_r = 0$. Thus, for a given voltage, the fields tend to be more intense in the range $0.25<\underline{z}_r<0.5$ than they are in the range $0<\underline{z}_r<0.25$. This nonlinear efffect is reflected in the tendency of the force to be skewed toward relative deflections in the former range. As would be expected from the singularity in the denominator of Eq. 7, as the electrodes tend to touch ($\underline{\xi}_o \to 0.5$), the force tends to approach infinity just to the left of $\underline{z}_r = 0.5$. The function $f(z_r)$ is then used to numerically integrate Eq. 8, with the result the normalized time-average force shown as a function of relative displacement phase δ and amplitude $\underline{\xi}_o$ in Fig. 4.13.2b. Again, the dependence on ξ_o is partially suppressed in the normalization.

The electromechanical model exemplified by Eqs. 7 and 8 is nonlinear, in the sense that the electrode deflections can be of arbitrary amplitude in the range $0 < \underline{\xi}_o < 0.5$. The fact that the time-average force becomes infinite as $\underline{\xi}_o \to 0.5$ is to be expected. At some instant, the electrodes are then at the point of touching and the associated field is becoming extremely large where the electrodes are nearly in contact. (Physically, electrical breakdown would of course present a limit on the validity of the theory.) Within the validity of an air-gap dielectric that does not permit electrical breakdown, the procedure which has been followed is an example of the left vertical leg in Fig. 4.12.2.

Further linearization, based on $\xi_s \ll d$ and $\xi_r \ll d$, demonstrates what is meant by a "linearized quasi-one-dimensional" model and by the completion of the step represented by the lower horizontal leg in Fig. 4.12.2.

For small amplitudes, $(1 + \xi_s - \xi_r)^{-3} \simeq 1 - 3(\xi_s - \xi_r)$, and hence Eq. 7 becomes

$$f(z_r) \to \int_z^{z+1} [(1 + \xi_s)\frac{\partial \xi_r}{\partial z} - \xi_r \frac{\partial \xi_s}{\partial z} - 3(\xi_s - \xi_r)\frac{\partial \xi_r}{\partial z} + \cdots]dz = \xi_o \pi \sin 2\pi z_r \qquad (10)$$

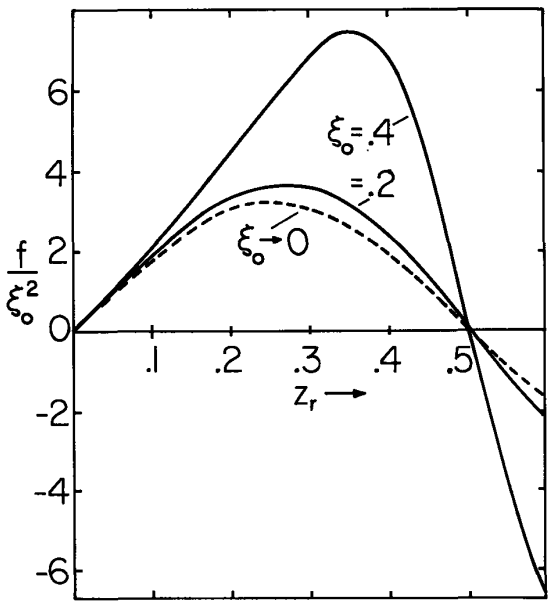

Fig. 4.13.2a. Electrical force on rotor of variable-capacitance machine (Fig. 4.12.1) as a function of normalized relative displacement $\underline{z}_r = z_r/\lambda$, with amplitude of electrodes as a parameter.

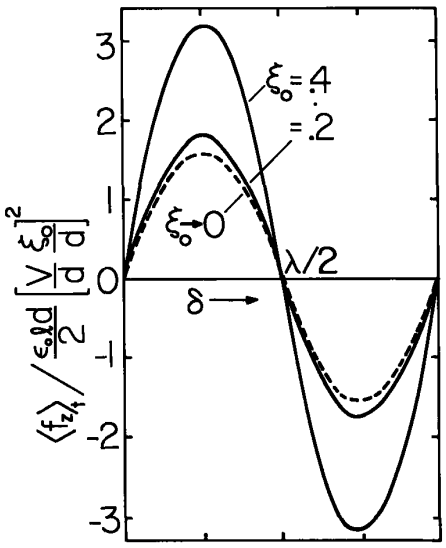

Fig. 4.13.2b. Normalized time-average force as a function of relative phase of sinusoidal excitation and rotor position.

(In carrying out this and the next integration it is helpful to represent the expressions of Eq. 9 in complex notation and make use of the averaging theorem, Eq. 2.15.14.) In turn, the time average called for by Eq. 8 can now be evaluated:

$$\left\langle f_{z/t} \right\rangle = \frac{\epsilon_o \ell V^2 \xi_o^2 \pi}{d} \int_{\underline{t}}^{\underline{t}+1} \cos^2 2\pi\underline{t} \sin 2\pi(2\underline{t} + \underline{\delta}) d\underline{t} \tag{11}$$

Carrying out this integration gives

$$\left\langle f_z \right\rangle_t = (\ell\lambda)\left[\epsilon_o \left(\frac{V}{d}\right)^2\right] \frac{d}{\lambda} \left(\frac{\xi_o}{d}\right)^2 \frac{\pi}{4} \sin\left(\frac{2\pi\delta}{\lambda}\right) \tag{12}$$

This approximation to the time-average force is shown by the broken curve of Fig. 4.13.2b.

Note that the small-amplitude force of Eq. 12 takes the form of the area $\ell\lambda$ multiplied by the electric pressure $\epsilon_o(V/d)^2$ times factors representing the fraction of this product obtained by dint of the geometry and the relative phase of the rotor and the driving voltage.

The variable-capacitance machine is closely related to the salient-pole machine described in Sec. 4.3 (Case 4b of Table 4.3.1). In that example, the stator is "smooth" with electrodes constrained by a traveling wave of potential. The effect of having a stator with saliencies driven by a simple voltage source (which is likely to be more convenient) is to produce a similar time-average force.

Linearized from the outset, the variable-capacitance machine of this section could also be viewed in terms of an interaction between the rotor traveling wave and one of two stator waves, the sum of which is equivalent to the physical stator structure considered. The result of such an analysis would be a model without restrictions as to the gap width relative to the wavelength. For the related example of Sec. 4.3, Eq. 4.3.27b retains information (represented by the denominator, $\sinh^2(kd)$) about the effect of the air gap in the limit where d becomes large. This result, restricted to small amplitude but valid for arbitrary air-gap spacing, is typical of the amplitude parameter expansion or linearization modeling step of Fig. 4.12.2. Taking the long-wave limit for the example from Sec. 4.3 constitutes taking the limit of Eq. 4.3.27b, $kd << 1$. Following this route of first linearizing and then taking the long-wave limit for the variable-capacitance machine considered in this section is an alternative derivation of Eq. 12, and is considered in the problems.

4.14 Van de Graaff Machine

A cross-sectional view of a Van de Graaff generator is shown in Fig. 4.14.1. An insulating belt is charged to one polarity as it passes over the lower pulley. This charge is carried upward to the essentially field-free region under the high-voltage terminal dome where it is removed and replaced by charge of opposite polarity, which then makes the return trip on the downward moving portion of the belt. Surrounding the belt are equipotential rings which help in controlling the field distribution by supporting much of the charge imaging that on the belt. The electric field consists of a generated field that is essentially vertical and a self-field associated with the charge on the belt. The equipotential rings help to insure that the self-field is essentially perpendicular to the belt surface and hence does not reinforce the generated field. To achieve relatively high electric stress (exceeding 10^7 V/m), the machine is operated in electronegative gases at elevated pressure.

An objective in this section, achieved while developing a lumped-parameter model for the simplified Van de Graaff generator shown in Fig. 4.14.2, is to further illustrate the use of quasi-one-dimensional models. This makes it possible to point out the analogies between d-c magnetic machines, Sec. 4.10, and what might be termed "d-c electric machines."

In several regards, the model shown in Fig. 4.14.2 does not include features of the machine shown in Fig. 4.14.1. To avoid undue complexity, the equipotential rings are uniformly distributed between the high-voltage dome and the ground at the bottom. In the machine pictured in Fig. 4.14.1, charging is by means of a corona discharge (ion impact charging). An alternative scheme, which has the advantage of being more easily related to a physical model, makes use of induction charging of a belt consisting of conductors linked by insulators.[1] For the present purposes, the belt (having thickness d) is considered to carry metallic segments that are insulated from each other. "Field" voltage sources v_f are used to induce belt charges of opposite polarity at the top and bottom. As the belt passes over the lower pulley, successive segments contact a grounded brush and hence form essentially plane-parallel capacitors having a voltage v_f across the belt thickness d. With the assumption that the belt electrodes essentially cover all of the belt surface, the belt surface charge is related to the field voltage by

$$\sigma_f = \frac{\varepsilon v_f}{d} \tag{1}$$

The current i_a' both supplies the charge carried upward by the belt and neutralizes that coming downward. Hence, for a pulley angular velocity Ω and radius R,

$$i_a' = 2\sigma_f \ell(\Omega R) = \frac{2\ell R\varepsilon}{d}\Omega v_f \tag{2}$$

Quasi-One-Dimensional Fields: In the ideal, the generated field is uniformly distributed with respect to the z axis. To achieve this ideal, in spite of the metal pressure vessel, the equipotential rings are tapped onto a distributed bleeder resistance running from the dome to the ground plane. At least under steady-state conditions, this insures that the ring potential $\Phi_r(z)$ has the required linear distribution consistent with a uniform z-directed electric field. The following developments identify the implications of having time-varying terminal variables, (v_a, i_a) and (v_f, i_f).

The transverse field components are determined as though any local region along the z axis is one in which the x-directed fields are independent of z. Thus, in the region between rings and pressure vessel,

$$E_{x3} = \frac{\Phi_r}{c} \tag{3}$$

The fields E_{x2} and E_{x1} (Fig. 4.14.2) must satisfy Gauss' law at the belt surface and be consistent with the potential being the same on the ring where it faces the belt on the right and at the same z location on the left. Hence, with fields defined positive if they are as shown in Fig. 4.14.2,

$$\varepsilon_o(E_{x1} + E_{x2}) = \sigma_f \tag{4}$$

$$-2bE_{x2} + 2aE_{x1} = 0 \tag{5}$$

Here, E_{x2} is approximated as being uniform over the width of the belt, even though the rings are cylindrical and the belt is flat. The distance b is an average spacing. Simultaneous solution of these

1. W. D. Allen and N. G. Joyce, "Studies of Induction Charging Systems for Electrostatic Generators: The Laddertron," J. Electrostatics 1, 71-89 (1975).

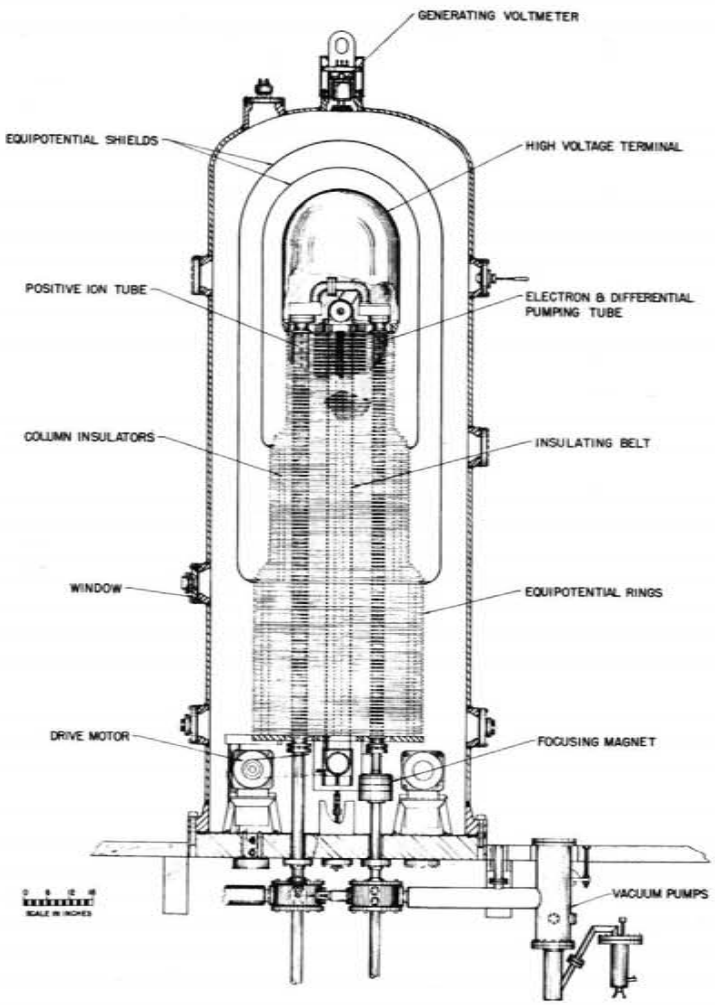

Fig. 4.14.1. Cross-sectional view of Van de Graaff high-voltage generator at M.I.T., High Voltage Research Laboratory. Device, used to provide accelerator potentials in medical research, operates at terminal voltages up to 5 MV.

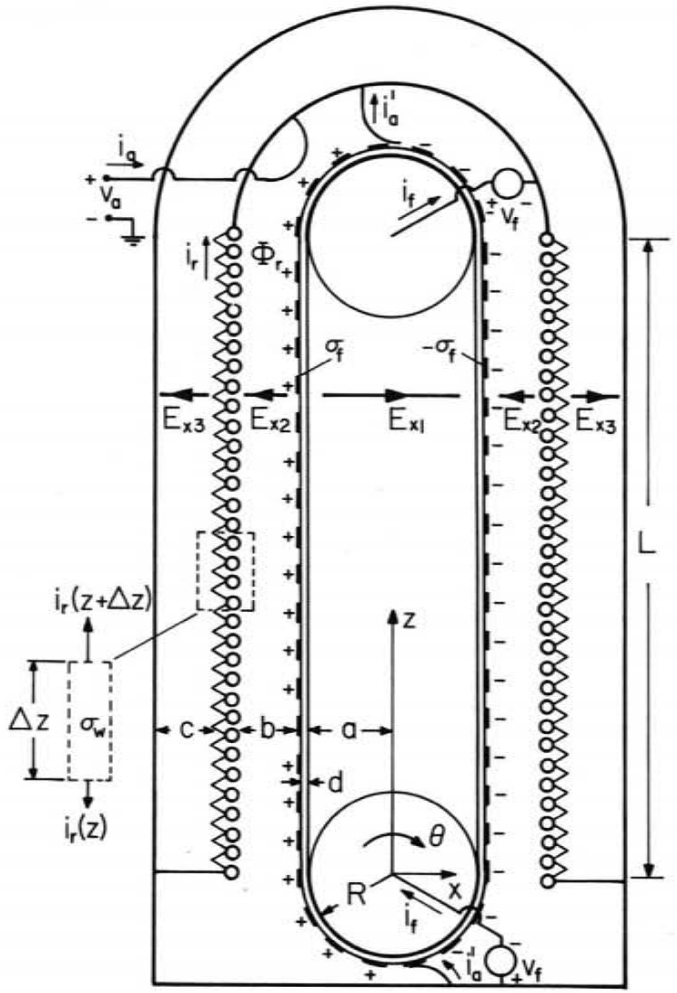

Fig. 4.14.2. Model for simple Van de Graaff machine exploiting inductive charging of belt carrying metal segments.

last two expressions shows that

$$E_{x2} = \frac{\sigma_f}{\varepsilon_o(1 + \frac{b}{a})} \tag{6}$$

These transverse fields make it possible to now write expressions that determine the field dependence on z. A section of the ring structure having incremental length Δz is shown in Fig. 4.14.2. Conservation of charge for this incremental section, which takes the form of a ring-shaped volume enclosing rings in the length Δz, is written be defining a ring charge per unit length (in the z direction), λ_r:

$$i_r(z + \Delta z) - i_r(z) = \frac{-\partial(\lambda_r \Delta z)}{\partial t} \tag{7}$$

In the limit $\Delta z \to 0$, Eq. 7 becomes

$$\frac{\partial i_r}{\partial z} = \frac{-\partial \lambda_r}{\partial t} \tag{8}$$

By symmetry, the contribution to the ring structure charge from the field inside (the images of the belt charges) cancel. What negative charge there is on the rings at the left imaging the positive belt charge on the upward-moving belt is canceled by the positive charge on the right imaging the downward moving negative belt charge. Hence, the only contribution to λ_r in Eq. 8 comes from the fields between the ring structure and the pressure vessel wall, approximated by Eq. 3; $\lambda_r \simeq 2\ell\varepsilon_o\Phi_r/c$. Thus, Eq. 8 becomes

$$\frac{\partial i_r}{\partial z} = \frac{2\ell\varepsilon_o}{c}\frac{\partial \Phi_r}{\partial t} \tag{9}$$

A second law is required to determine the distribution of (i_r, Φ_r). This is simply Ohm's law relating the z component of the electric field to the current carried by the bleeder resistance. With R_a the total resistance, and hence R_a/L the resistance per unit length, it follows that

$$-\frac{\partial \Phi_r}{\partial z} = \frac{R_a}{L} i_r \tag{10}$$

Quasistatics: There is now enough of the model developed that a meaningful discussion can be made of two quasistatic approximations implicit to a lumped parameter model for the Van de Graaff machine.

First, Eq. 1 is misleading in that it implies that the belt charge is instantaneously established in proportion to the field voltage over the full length of the belt. Of course, an abrupt change in v_f would result in a "wave" of surface charge carried to the high-voltage dome by the moving belt. In the model developed here, temporal variations are presumed to be long compared to a transport time $L/\Omega R$. With this caveat as to the dynamic range of the resulting model, the belt charge is taken as proportional to the field voltage over the full length of the machine. The machine dynamics are quasistatic relative of the time required for the belt to traverse the distance between pulleys.

A second quasistatic approximation is necessary to approximate the field distribution governed by Eqs. 9 and 10 in a way that leads to a lumped-parameter model. Elimination of i_r between these equations results in the diffusion equation. The potential (and hence the ring charge) diffuses in the z direction, and the resulting dynamics are not in general representable in lumped-parameter terms. The subject of charge diffusion on heterogeneous structures is taken up in Sec. 5.15. Here, the quasistatic concepts of Sec. 2.3 are revisited to obtain a low-frequency lumped parameter model. But, now the critical rate process is represented by a charge diffusion time, not an electromagnetic wave transit time.

If the fields were truly static, Eq. 9 shows that the current would be independent of z. Thus, the zero-order current is $i_r = i_{ro}(t)$. The associated potential distribution can then be found by integrating Eq. 10:

$$\Phi_{ro} = v_a \frac{z}{L}; \quad v_a = R_a i_{ro} \tag{11}$$

This is the desired potential distribution. It assures a uniform generated field (z-directed) over the region of the moving belt.

Because the voltages (v_f, v_a) are in general time-varying, there is an additional capacitative current. The capacitance is distributed between the high-voltage terminal and ground, and is deduced

by considering the first-order current i_{r1}, determined from Eq. 9 with the zero-order voltage (given by Eq. 11) introduced for Φ_r. (Note that the procedure followed here is an informal version of that outlined in Sec. 2.3.):

$$\frac{\partial i_{r1}}{\partial z} = \frac{2\ell\varepsilon_o}{c}\frac{dv_a}{dt}\frac{z}{L} \tag{12}$$

The z dependence is given explicitly, so this expression can be integrated to obtain

$$i_{r1} = \frac{\ell\varepsilon_o}{cL}\frac{dv_a}{dt}z^2 + f(t) \tag{13}$$

with f(t) an integration function to be determined shortly by boundary conditions. Introduction of Eq. 13 on the right in Eq. 10 gives an expression for Φ_{r1} that is similarly integrated to obtain

$$\Phi_{r1} = \frac{R_a}{L}\left[\frac{\ell\varepsilon_o}{cL}\frac{dv_a}{dt}\frac{z^3}{3} + f(t)z\right] \tag{14}$$

Because $\Phi_r = 0$ at $z = 0$, the second integration function has been set equal to zero.

The total voltage and current distributions consist of the sum of zero and first order parts. Because the zero-order distributions already satisfy the correct boundary conditions, the first order voltage must vanish at $z = L$. This serves to evaluate f(t) in Eq. 14. If f(t) is then introduced into Eq. 13, and that expression evaluated at $z = L$, the current $i_r(L,t)$ has been found:

$$i_r \simeq i_{ro} + i_{r1} = \frac{v_a}{R_a} + \frac{2\ell L\varepsilon_o}{3c}\frac{dv_a}{dt} \tag{15}$$

Note that because of the essentially linear distribution of voltage over the length of the structure, the equivalent capacitance is 1/3 what it would be if the structure formed a plane-parallel capacitor with the vessel wall. (This same equivalent capacitance can be computed with much less trouble and much less insight by simply finding the total electric energy storage and setting it equal to $\frac{1}{2} C_{eq} v_a^2$.)

Electrical Terminal Relations: The high-voltage terminal has a total current i_a which is the sum of $-i_a'$ given by Eq. 2, the ring-structure current i_r from Eq. 15, and a current required to charge the dome. With the last of these modeled as charging half of a spherical capacitor, the high-voltage terminal relation has the form

$$i_a = \frac{v_a}{R_a} - G_e\Omega v_f + C_a\frac{dv_a}{dt} \tag{16}$$

where

$$G_e \equiv \frac{2\ell R\varepsilon}{d}; \quad C_a \equiv \frac{2\ell L\varepsilon_o}{3c} + 2\pi\varepsilon_o(a + b)$$

The field terminal relations depend on details of the specific geometry in the region of the pulleys. They take the form

$$i_f = \frac{v_f}{R_f} + C_f\frac{dv_f}{dt} \tag{17}$$

where R_f is the resistance of the belt material and the pulley mounting and C_f is the capacitance of the pulley relative to ground or to the high-voltage terminal.

Mechanical Terminal Relations: The electrical torque acting in the θ direction on the lower pulley is computed by simply multiplying the z-directed force per unit area, $\sigma_f E_z$, by the total belt area $2\ell L$ and the lever arm R. In view of Eq. 1 for σ_f and the fact that $E_z = -v_a/L$,

$$\tau = -G_e v_f v_a \tag{18}$$

where the coefficient G_e is the same as defined with Eq. 16.

Analogy to the Magnetic Machine: The terminal relations summarized by these last three equations have a canonical form not only found to describe other electric machines of quite different configuration, but also to describe magnetic d-c machines. For example, compare these relations to Eqs. 4.10.17, 4.10.21, and 4.10.6. The analogy is complete provided that the identification is $i_f \to v_f$, $v_a \to i_a$, $R_a \to R_a^{-1}$, $G_m \to G_e$.

The Energy Conversion Process: Modes of energy conversion are explored by considering the machine constrained in such a way that the high-voltage terminal current i_a is fixed, as is also the angular velocity Ω. Then, the machine is made to pass from one energy conversion regime to another by varying the field voltage v_f.

Under steady-state conditions, the electrical power input is expressed by solving Eq. 16 for v_a and multiplying by i_a:

$$v_a i_a = R_a i_a (i_a + \Omega G_e v_f) \tag{19}$$

The mechanical power output is also written in terms of (v_f, i_a) by substituting for v_a in Eq. 18 and multiplying by Ω:

$$\Omega\tau = -\Omega G_e R_a v_f (i_a + \Omega G_e v_f) \tag{20}$$

With the appropriate identification of variables, plots of these expressions, and the implied modes of energy conversion, are as shown in Fig. 4.10.5.

4.15 Overview of Electromechanical Energy Conversion Limitations

This chapter has two broad objectives. On the one hand, examples are chosen to illustrate techniques for using a field description in deducing lumped-parameter models. On the other hand, the examples convey an overview of systems that are electromechanically kinematic while providing a background for understanding the kinematic systems taken up in Chaps 5 and 6 and the coupling to deformable media developed in later chapters.

The Maxwell stress acting on a "control volume" enclosing the moving material, introduced in Sec. 4.2 as a convenient way to relate the fields to the total force or torque, is also useful in obtaining a qualitative perception of basic limitations on the energy conversion processes. These volumes are represented in an abstract way by Fig. 4.15.1. The longitudinal direction, denoted by (ℓ), generally represents the direction of material motion. Perpendicular to this is the transverse direction denoted by (t).

The net magnetic or electric force on the volume in general has contributions from both the transverse and longitudinal surfaces, A_ℓ and A_t. But, in all of the examples of this chapter, shear stresses rather than normal stresses contribute to the energy conversion process. To exploit this fact, the active volume of the devices has a longitudinal dimension that is large compared to transverse dimensions. For example, in rotating machines, maximum use of the magnetic or electric stress is made by having an "air gap" that is narrow compared to the circumference of the rotor. In the Van de Graaff machine, the same considerations lead to a "slender" configuration with the belt charges producing an electric field E_t across a narrow gap and the generated field being E_ℓ.

In all of these "shearing" types of electromechanical energy converters, the mechanical power output takes the form

$$P_m = UA_tK[\,\mu H_\ell H_t\,] \quad \Big| \quad P_m = UA_tK[\,\epsilon E_\ell E_t\,] \tag{1}$$

Here, U and A_t are respectively the material velocity and an effective transverse area, e.g., the rotor surface velocity and area respectively in a rotating machine. The largest possible net contribution of the magnetic or electric shear stress contribution, $[\,\mu H_\ell H_t\,]$ and $[\,\epsilon E_\ell E_t\,]$ respectively, is obtained if stress contributions to one of the surfaces of the control volume are minimized. Generally, this is accomplished by designing field sources into the volume. The factor K in Eq. 1 reflects geometry, material properties and phase angles. In a synchronous machine, it accounts for the air-gap spacing, the sinusoidal spatial dependence of the excitations and the relative phase of stator and rotor excitations. In the variable-capacitance machine of Sec. 4.13, this factor (which represents the "cut" of the ideal power output that is obtained) is also proportional to the product of the saliency amplitudes on rotor and stator.

Because of their higher energy conversion density, it is generally recognized that conventional magnetic electromechanical energy conversion systems are more practical than their electric counterparts. This predisposition has its basis in the extreme disparity between electric and magnetic shear stresses that can be produced under ordinary conditions.

In conventional magnetic equipment, the limit on the magnetic flux density, set by the saturation of magnetic materials, is in the range of 1-2 tesla (10 - 20 kgauss). The electric field intensity in air at atmospheric pressure (over macroscopic dimensions in the range of 1 mm to 10 cm usually of interest) is limited to less than the breakdown strength, 3×10^6 V/m. Thus under conventional conditions, the ratio of powers converted by electric and magnetic devices having the same

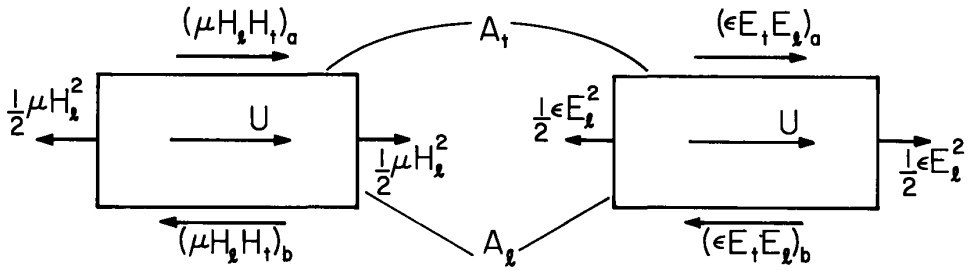

Fig. 4.15.1. Abstraction of regions of active electromechanical coupling in magnetic and electric field systems.

velocity U, effective area A_t and factor K is (from Eq. 1) the ratio of the respective shear stresses. Using as typical numbers, B = 1 and E = 10^6 V/m, this ratio is

$$\frac{(P_m)_{electric}}{(P_m)_{magnetic}} \simeq \frac{\epsilon_o E_\ell E_t}{B_\ell B_t/\mu_o} \simeq 10^{-5} \qquad (2)$$

The disadvantage inherent to electric energy conversion devices can be made up by increasing the velocity, the effective area, or the electrical breakdown strength. Now, illustrated by some examples is the way in which rough estimates of the energy converted can be made with Eqs. 1, provided the factors are evaluated with some appreciation for the underlying engineering limitations.

Synchronous Alternator: A large synchronous machine, driven by a turbine in a modern power plant, would have the typical parameters:

rotor radius b ≃ 0.5 m

rotor surface velocity U = 2π60b = 188 m/sec

rotor length ℓ = 7 m

air gap transverse and longitudinal flux densities ≃ 1 tesla

These figures are typical of the full-scale generator modeled by the machine shown in Fig. 4.7.1c. An upper bound on the factor K in Eq. 1 to take into account the sinusoidal field distributions on rotor and stator, is reasonably taken as 1/2. Thus, from Eq. 1a, the mechanical power requirement (and with reasonable efficiency, therefore the maximum electrical power output) is expected to be approximately

$$P_m = (188)[(2\pi)(0.5)(7)](0.5)(1)/4\pi \times 10^{-7} = 1.6 \times 10^9 \text{ watts} \qquad (3)$$

This is about 50% more than the power rating of existing equipment having roughly the parameters used.

Superconducting Rotating Machine: The limit on practical magnetic shear stress set by the saturation of magnetic materials more basically arises from the Ohmic heating limit on current density. A synchronous machine like that described in Sec. 4.9 but with no magnetic materials is in principle not limited by saturation. But it is limited by the current density consistent with available means for removing the heat from the windings. (A current density of 3 x 10^6 A/m^2 is projected for the normal conducting armature of the machine shown in Fig. 4.9.2.) The incremental increase in magnetic field associated with increasing the current density once the magnetic materials have been saturated makes conventional operation in this range generally unattractive.

One way to obtain higher field intensities than are practical using conventional conductors is to make use of superconductors. In time-varying fields, superconductors in fact have losses and are difficult to stabilize. But, for slowly varying and d-c fields they can be used to produce magnetic field intensities greater than the 1-2 tesla range of conventional equipment. Under balanced synchronous conditions, the field winding is only subject to d-c fields, while the armature winding carries a-c currents and is subject to a-c fields. Thus, in the machine of Fig. 4.9.2, the rotor winding is superconducting while the stator is composed of normal conductors. With that machine, the projected (rotor) field is in the range of 5-6 tesla and the area A_t required for a given power conversion accordingly reduced. For example, a two-pole 60 Hz machine having B_r = 1 tesla, B_θ = 5 tesla and rotor length and radius ℓ = 5 m and R = 0.3 m, respectively, has an estimated mechanical power input of $A_t T_{\theta r} R\Omega$ = $(2\pi\ell R)(B_r B_\theta/2\mu_o)(R)(2\pi f) \simeq 2 \times 10^9$ watts. These are representative of the parameters for a projected

2000 MVA superconducting alternator.[1]

Variable-Capacitance Machine: In machines exploiting electrical shear stresses, the limit on power converted posed by electrical breakdown can be pushed back by either making the insulation an electronegative gas under pressure, or vacuum. Typical improvements in breakdown strength with increasing pressure above atmospheric are shown in Fig. 4.15.2.[2] In principle the field intensity can be increased to more than 3 x 10^7 V/m, and hence the electric shear stress can be increased by a factor of more than 100 over that used in calculating Eq. 2.

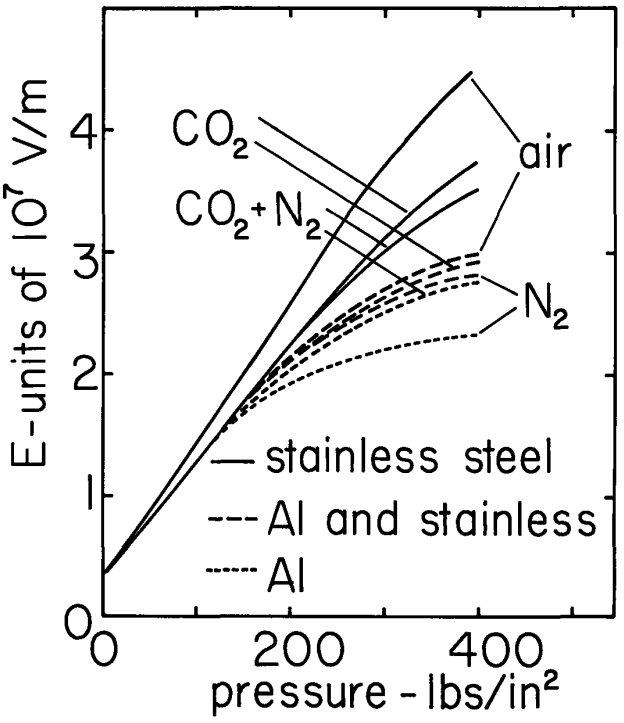

Fig. 4.15.2. Breakdown strength of common gases as a function of gas pressure for several different electrode combinations.[2]

The machine shown in Fig. 4.13.1c is designed for operation in vacuum. Here, the mean free path is very long compared to the distance between electrodes. As a result, breakdown results as particles are emitted from the electrode surfaces, accelerating until impacting the opposite electrode where they can produce further catastrophic results. Because the voltage difference between electrodes determines the velocity to which particles are accelerated, breakdown is voltage-dependent. Put another way, the breakdown field that can be supported by vacuum is a decreasing function of the gap distance. It also depends on the electrodes. Using steel electrodes having exposed areas of 20 cm^2, a typical breakdown strength under practical conditions appears to be 4 x 10^7 volts across a 1-mm gap.[3]

The electric machines illustrate how the power conversion density can be increased by dividing the device volume into active subregions. In an electric machine, current densities are small and as a result little conducting material is required to make an electrode function as an equipotential. By making stator and rotor blades (as well as intervening vacuum gaps) thin, it is possible to pack a larger amount of area A_t into a given volume. The limitation on the thickness and hence on the degree of reticulation that can be achieved in practice comes from the mechanical strength and stability of the rotor. Because of material creep and fracture, centrifugal forces pose a limit on the rotational velocity; but more important in this case, if a blade passes through a high-field region slightly off center, the result can be a transverse deflection that is reinforced by the next pulsation. The tendency for the blades to undergo transverse vibrations as they respond parametrically to the pulsating electric stress on each of their surfaces limits the effective area.

As numbers typical of the machine shown in Fig. 4.13.1c (where there are six gaps), consider:

R = mean radius of blades = 0.2 m
blade length = 0.12 m

U = mean blade velocity at 30,000 rpm = 630 m/sec (an extremely high velocity)

E = 5 x 10^6 V/m

$A_t = (0.2)(2\pi)(0.12) = 0.9\ m^2$

Remember that the maximum electric field appears where the electrodes have their nearest approach, so the average field used is considerably less than the maximum possible. According to Eq. 1b with K=1, the power output is then at most 125 kW. Actually, the factor K significantly modifies this rough estimate. According to Fig. 4.13.2b, for $\xi_o/d = 0.4$ and a $\lambda/4$ phase,

$$K = (3.2)\left[\frac{d}{2\lambda}\left(\frac{\xi_o}{d}\right)^2\right] \qquad (4)$$

1. J. L. Kirtley, Jr., and M. Furugama, "A Design Concept for Large Superconducting Alternators," IEEE Power Engineering Society, Winter Meeting, New York, January 1975.

2. J. G. Trump et al., "Influence of Electrodes on D-C Breakdown in Gases at High Pressure," Electrical Engineering, November (1950).

3. A. S. Denholm, "The Electrical Breakdown of Small Gaps in Vacuum," Can. J. Phys. 36, 476 (1959).

For $d/\lambda \simeq 0.1$, $K \simeq 2.5 \times 10^{-2}$, and the fraction of the ideal energy conversion is not very large. Instead of 125 kW, the postulated machine is predicted to produce 3 kW.

Electron-Beam Energy Converters: One class of electric field energy convertors that often have very respectable energy conversion densities make use of electrons themselves as the moving material. The model of Sec. 4.6 is developed with this class of devices in mind. A high-energy conversion density can result from the extremely large electron velocities that are easily obtained. For example, an electron having mass m and charge q accelerated to the potential Φ has the velocity

$$U = \sqrt{\frac{2q\Phi}{m}} \tag{5}$$

For the electron, $m = 9.1 \times 10^{-31}$ kg and $q = 1.6 \times 10^{-19}$ C. Thus, an accelerating potential of 10 kV results in a beam velocity of 6×10^{7} m/sec!

In electron-beam devices, the electric shear stress is not usually limited by electrical breakdown, but rather by the necessity for maintaining columnated electrons in spite of their tendency to repel each other. To inhibit lateral motion of the charged particles due to their space charge, a magnetic field is commonly imposed in the direction of electron streaming. The Lorentz force, Eq. 3.1.1, then tends to convert any radial motion into an orbital motion, while letting electrons stream in the same direction as the imposed magnetic field.[4]

Electron beams are typically used to convert d-c electrical energy to high-frequency a-c. In fact, the high beam velocity requires that for a synchronous interaction, the frequency f is the beam velocity U divided by the wavelength of charge bunches; $f = U/\lambda$. Hence, for a wavelength $\lambda = 6$ cm, the frequency for a traveling-wave interaction with the 10 kV beam would be essentially $f = 6 \times 10^{7}/6 \times 10^{-2} = 10^{9}$ Hz. The practical limit on how short λ can be while obtaining useful coupling between beam and traveling-wave structure is evident from Sec. 4.6.

The kinematic picture for the beam is useful for making the electroquasistatic origins of the coupling clear and to identify the nature of the synchronous interaction upon which devices like the traveling-wave tube depend. But, because the electron bunching takes place self-consistently with the coupling fields, it is necessary, in engineering electron-beam devices, to treat the electrons as a continuum in their own right.[4] Such examples are taken up in Chap. 11.

Both electron-beam devices and synchronous alternators convert mechanical to electrical energy. As a reminder rather than a revelation, note that the synchronous alternator is of far more fundamental importance for human welfare, because when attached to the shaft of a turbine driven by a thermal heat cycle, it is capable of converting low-grade thermal energy to a high-grade electrical form. Its conversion of energy naturally fits into schemes for production of energy from natural basic sources. By contrast, the electron-beam devices only convert d-c electrical energy to a high-frequency electrical form.

4. M. Chodorow and C. Susskind, Fundamentals of Microwave Electronics, McGraw-Hill Book Company, New York, 1964.